UNIVERSITÀ
DEGLI STUDI
FIRENZE

PhD in
International Doctorate in Atomic and Molecular Photonics

CYCLE XXVI

COORDINATOR Prof. Wiersma Diederik

Versatile systems for visible light communication (VLC): from optical antennas based on fluorescent concentrators to software defined radio (SDR)-based receivers

Academic Discipline (SSD) FIS / 03 - ING/INF/03

Doctoral Candidate
Muhammad Ali Umair

_____
(signature)

Supervisor
Dr. Jacopo Catani

_____
(signature)

Coordinator
Prof. Wiersma Diederik

_____
(signature)

I dedicate this thesis to the memory of my departed **parents**, **uncle** and **aunt**. May Allah grant them high ranks in the afterlife.

Contents

List of Figures

List of Tables

Acknowledgements

First of all I would like thank you to my esteemed supervisor, Dr. Jacopo Catani, I owe a debt of gratitude for his invaluable guidance, unwavering support, and boundless patience. I am equally thankful to Dr. Marco Meucci, whose consistent, unwavering and unconditional support have smoothed the three-year journey. My appreciation also extends to Dr. Marco Seminara, whose assistance during my first year in understanding the experimental system was indispensable. Heartfelt thanks to all our industrial partners, Glass to Power and FluoCom, and particularly to Prof. France Mainardi, Prof. Sergio Broveli, Prof. Marco Fattori, Dr. Luigi Consolino, Dr. Sandra Doria, and Alessia Sorgi for their invaluable discussions and collaboration.

A special mention goes to my mentors and guide Mufit Abdul Khaliq Azad and Mr. Anis Ahmed Sajad, whose affiliation has been instrumental in shaping the person I am today. Their wisdom and guidance have been a source of strength and enlightenment throughout this transformative journey. To my family, especially my sisters, wife your unwavering support from afar has been my anchor. Special acknowledgment goes to my flatmates and fellow country-mate doctoral and postdoctoral colleagues, especially Dr. Ghulam Murtaza, Dr. Muhammad Atif Khattak, and Mr. Usman Ali Shah. Without their companionship and support, my stay in Italy would have been considerably more challenging.

In this moment of completion, I recognize the collective effort of those both seen and unseen who have played a pivotal role in my academic journey.

Abstract

Over the course of three years, this doctoral thesis delves into various aspects of visible light communications (VLC). The project has concentrated on development and implementing optical wireless communication (OWC) systems across diverse application scenarios. The primary focus of the thesis revolves around the creation and characterization of various organic and inorganic fluorescent concentrators (FCs), and software-defined radios (SDR) based optical receivers. The performance of optical receivers is studied by characterizing their absorption-emission spectra, bandwidth (BW), and field of view (FoV). A notable advancement is achieved by the development of Quantum-Dots (Q-dots) FCs optical receiver for long-range communication, enabling communication link up to 100 m directly under sunlight. In addition to this, for realistic indoor applications employing white light sources, this thesis investigates and compares the performance of optical receivers based on two organic fluorophores. Experimental outcomes demonstrate a field of view of approximately FoV $\simeq 85^{\circ}$, crucial for mitigating misalignment issues between the transmitter (TX) and receiver (RX). Moreover, a SDR based digital signal processing (DSP) stage is also designed for filtering ambient light. This stage significantly enhances the performance of optical communication systems by nearly twofold, even in outdoor conditions under direct sunlight. An important contribution of the thesis is the design and development of smart window for VLC, utilizing Q-dots FCs. Finally, preliminary results of the Cryogen-free quantum cascade laser (QCL) employed for OWC are also presented.

Chapter 1

Introduction

Communication has been a vital and fundamental aspect of human history and civilization, and various methods have evolved for efficient communication and connectivity. Presently, the increasing demand for high data rates, low latency, and exponential increase of connecting devices heavily bottle-necked the current radio frequency (RF) wireless communication systems[3]. Moreover, RF-based communication technologies face interference, which can potentially threaten human health; for this reason, they are prohibited in airplanes and hospitals [4]. This raises the demand for developing more innovative wireless technologies exploiting TXs and RXs in other frequency bands of the EM wave spectrum with no or very few interference issues. In this scenario, exploiting the unlicensed optical band of EM spectrum OWC technology (Free Space Optical Communication (FSO) and VLC) exploits light for data transmission, offering unique advantages like high data rate and increased security. OWC is also envisioned as an integrated technology in future 6G networks, it also aims at overcoming the limitations connected to the increasing RF spectrum crunch [5]. In Section 1.1 I will discuss a detailed historical background of VLC, its technological advancements, and its role in next-generation-networks (NGNs).

1.1 Visible Light Communication

The use of light as a communication medium dates back to ancient civilizations. One of the earliest examples is light beacon system which was used in ancient Greece for sending messages over long distances. The use of fire for communications is reported in the Bible as well, while for long distance communication reflective surfaces, and mirrors were used to send messages. In Alexandria during the era of great Pharaohs light beacons were used to navigate boats sailing in water [6]. In recent times telegraph based on chains of semaphore each at the distance of 10 km was built by a french naval officer Claude Chappe at the end of eighteenth century [6]. In late nineteenth century American military officer designed a solar telegraph based on simple mirrors, which transfers sunlight encoded according to Morse code. A milestone was achieved by Alexander Graham Bell in 1880, when he invented a photophone [7], through which he was able to transmit voice signals using light at a distance of 200 m as shown in Figure 1.1.

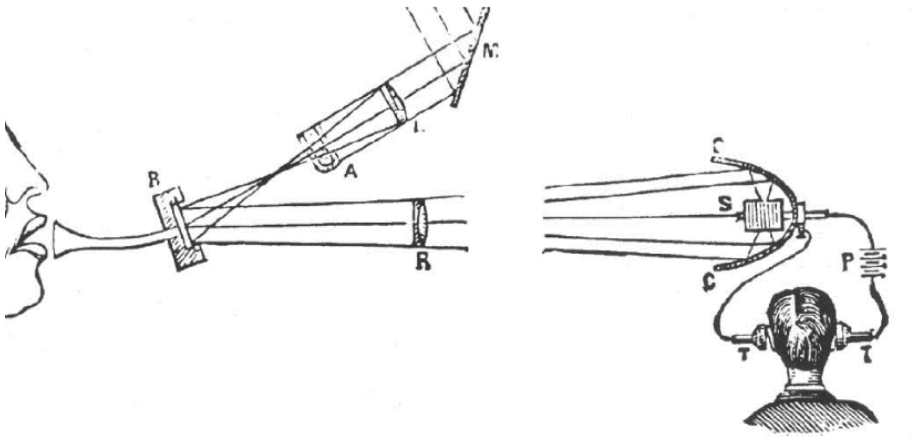

Figure 1.1: Photophone invented by Alexander Graham Bell. Reproduced from ref[8]

In 20th century a revolutionary breakthrough was made by Theodore Maiman [6] by the invention of Light Amplification by Stimulated Emission of Radiation (LASER) which provides a coherent light source. A recent breakthrough in this field was reported in 1960, when Bell Labs performed an experiment in which they transmitted signals upto 40 km using ruby LASER. The first infrared (IR) based communication link was developed by Gfeller

and Bapst in 1979 which was able to send at hundreds of Mbps in indoor scenarios [9].

In late 20th century researchers began to experimenting the transmission of data through light in air as a medium this technique is named as OWC. Researchers and companies started developing more robust systems capable of transmitting data using modulated light over longer distances which is called FSO. One of the breakthrough in FSO technology was in 2000s when a successful high speed optical wireless link was established [10]. Moreover FSO was more reliable in situations where laying cables was not so recommended making it viable solution for last-mile connectivity [11]. Additional to this, with the invention of LEDs the concept of VLC for wireless communication traced back in the late 20th century when scientists started exploring the transmission of data by modulating visible light. The most recent ground breaking VLC experiment was done by a research group in Keio university in Japan, they demonstrated transmission of information using white LEDs (WLEDs) [12]. VLC has already demonstrated its value as a foundational technology for IoT [13] and smart city protocols [14]. The main benefit of VLC is that it exploits the widely used, already implemented architecture of LED sources, providing illumination and communication at the same time with less energy consumption costs [15]. OWC technology covers infrared (IR), visible and ultraviolet (UV) portions of EM spectrum, VLC particularly covers from 430 to 790 THz, which corresponds to wavelengths of 750 to 380 nm as shown in Figure 1.2.

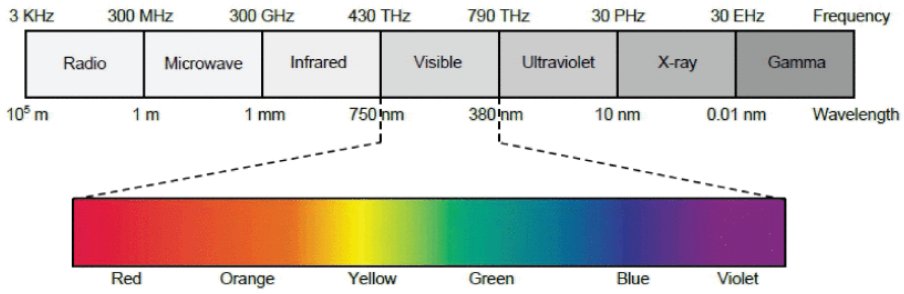

Figure 1.2: Electromagnetic (EM) spectrum indicating visible light portion. Reproduced from [8]

VCL has proven itself as a very promising technology for different applications such as wireless data transmission, visible light positioning, health care etc [16]. Wireless data

transmission using VLC is one of the interesting applications in indoors especially home, offices and supermarket buildings [17]. Data transmission through VLC is called light-fidelity (Li-Fi), a term coined by Professor Harald Haas to perform high speed data transmission over network [18]. As an example Li-Fi network in office and for personal use is represented in Figure 1.3a. Moreover, another interesting example of VLC is indoor positioning systems which is also called visible light positioning (VLP) [19]. Differently from Global positing system (GPS) [20], VLP can also work in those scenarios where GPS can not such as deep underground locations and inside certain buildings. VLP systems can provide a flexible and cost effective positioning system exploiting already employed LED infrastructure. In 2013 a pioneering experiment was carried out at "Korean Mall" which was termed as sale navigation [6]. VLP exploits white and multicolored LEDs which makes it more versatile [21]. VLP can also be used in theaters and museums to guide customers to their seats and to provide information to visitors about certain art work such as historical background [22]. The main challenge in implementation of VLC in indoor is obstruction between TX and RX caused by human bodies and furniture or other objects [8]. For this reason multiple LEDs points are necessary so that no shadow exist in a room. but this cause signal interference. To address these issues efficient coding schemes are designed to ensure sufficient spectral efficiency [23]. However, as OWC required line of sight (LoS) to improve the communication performance novel optical RX architectures are required having wide FoV so that LoS issues can be minimized.

Additionally, the progress of outdoor OWC (which is usually called FSO) is slow as compared to indoor applications due to adverse effect of atmospheric turbulence on communication link [24]. In outdoor optical sources exploiting IR, visible light and UV spectrum are used to establish communication link [25]. For long distance communication such as ground to satellite and satellite to satellite communication FSO is exploited to established high speed communication links [26].

Figure 1.3: VLC application: a) Indoor VLC network, b) outdoor VLC based intelligent transport system (ITS). Reproduced from [1]

FSO is also a strong candidate to establish communication in remote areas where conventional communication infrastructure is not present [27]. One of the outdoor OWC application is underwater high speed communication links, which is helpful in exchanging information for tactical surveillance, offshore exploration, and ocean research. Presently underwater communication is carried out by means of acoustic waves, however this technology posses lot of limitation like low BW, scattering, low propagation speed and high attenuation [28]. Recently underwater optical wireless communication (UWOC) was realized at 6.25 Mbps upto 2.5 m for diver communication [29]. However, most appropriate operating wavelength should be selected for UWOC so that impurities and water can have minimum effect on communication link. One of the most promising outdoor application of VLC is to realize intelligent transport system (ITS) (Figure 1.3b) by implementing vehicle to infrastructure (V2I), or vehicle to vehicle (V2V) communication links for safe driving by exchanging useful information, and also to control the traffic density in more intelligent way [30]. The pioneering communication link was established in Japan by exploiting LEDs deployed in vehicles and streetlights [31]. Researchers in [32] have demonstrated communication link up to 70 m using car headlamps achieving data rate up-to 50 Mbps. One of the challenge in establish-

ing of ITS based on VLC is to ensure efficient communication between RX and TX while both are moving. In order to address this challenge high speed cameras and 2D imaging sensors were used at receiver [33]. One of the main challenge is presence of background light interference and light scattering due to smog, fog, rain etc.

In VLC links high data rates can be achieved by large BW and signal-to-noise ratio (SNR) at both TX and RX. Photodetectors (PDs) are used to received optical signal (OS), where PDs with high BW have very small active area (1 mm^2), while large active area PDs posses very small BW [34]. As the active area of PD is small so the optical gain (OG) is less. To increase the OG at RX optical focusing elements are used. However these depends on reflection and refraction, therefore conserves etendue, hence reducing FoV [35]. Recently a new way to increase the OG is based on Luminescent Solar Concentrators (LSCs) also known as FCs [36, 37, 38]. LSC (FC) is usually made by a slab doped with a particular fluorophore. Principally incoming light is collected by the largest surface area of FC, where some of the light is absorbed by the fluorophore material, and reemitted light at larger wavelength. Due to the high refractive index of the slab, the light is wave-guided towards the edges of the slab until it reaches the PD coupled to one of the edges of the FC. Due to the large surface area of FC, high OG can be achieved at RX, while BW of the FC depends on the type of fluorophore and on the size of PD. The details about FC and its working principle are given in Chapter 3.

1.2 Contribution of this thesis

The research work presented in this doctoral thesis spans the period of three years (2020-2023). During the three years I focused on different applications of OWC listed below:

- Organic FCs based optical antennas (OAs) for WLED communication.
- Inorganic FCs based novel antennas enabling long distance communication in realistic outdoor conditions.

- SDR based noise filtering stage, to improve the performance of VLC system in presence of strong ambient light.

Therefore, Quantum-Dots based FC OA has been designed and analyzed, with the collaboration of Milan based Glass To Power company. To the best of our knowledge this is the first time a communication up to 90 m with FC based antenna directly under the sun has been demonstrated. Moreover, our next focus was to design OA based on FCs doped with organic fluorophore, with the collaboration of Institute for the Chemistry of Organometallic Compounds (ICCOM) of National Research Council (CNR) Italy. A complete analysis of the FCs such as temporal response, maximum BW, external efficiency has been realized. My efforts were also focused on the design and implementation of SDR based digital signal processing stage (DSP) to filter out strong ambient noise, generated by artificial or natural sources. The performance of SDR based filtering system was compared with conventional systems under strong ambient light in both indoor and outdoor scenarios. A complete characterization of new OAs based on two different organic fluorophores (LR305 and DQ1) has been carried out exploiting both blue and white LED sources.

1.3 Thesis Organisation

The present Thesis is organized as follows:

- Chapter 1 introduces the context of research.
- Chapter 2 presents architecture of the experimental setup.
- Chapter 3 presents an introduction on FC.
- Chapter 4 presents research on Quantum-dots (Q-dots) based FC antenna for long-range OWC are described and discussed.
- Chapter 5 gives insight of our characterization of an organic FC-based VLC RX stage.

- Chapter 6 presents the design and characterization of SDR based DSP filter stages.
- In Chapter 7 an outlook of preliminary results of Q-dots FC based smart window for VLC and Quantum cascade LASER (QCL) for OWC is given.
- Chapter 8 draws the main conclusion of the present works.

After Chapter 8, readers will find an extensive bibliography containing all referred works in this thesis.

Chapter 2

Visible Light Communication (Overview)

In Figure 2.1 general architecture of VLC system is shown. Data are encoded/modulated at encoder, the modulated data then proceeds to a LED driver, which controls the optical source. The optical source receives the modulated data and transmits it through the air. During this transmission, various phenomena such as absorption, scattering, and beam wandering occur. The light signal is captured by a PD. After reaching the PD, the signal is transmitted to a decoder. Finally at this stage, the data undergoes demodulation and digitization.

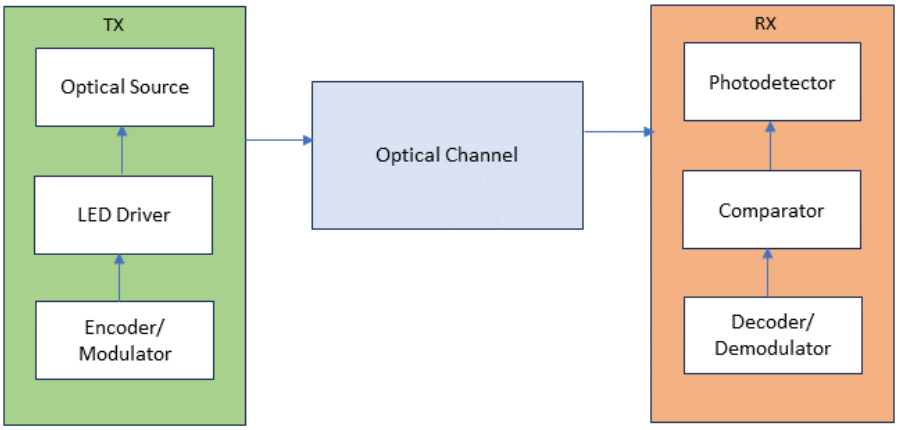

Figure 2.1: Block diagram of VLC experimental setup . In TX side encoder/modulator block encodes/modulates message that is added with DC provided by the current modulator to the light source. The modulated light passes through the optical medium and at RX it is collected by photodetector, after that signal is digitized by the comparator and fed to a demodulator/decoder stage for signal processing.

2.1 Transmitter

In this section, I will discuss the transmission unit used in various experiments covered in the thesis. The components of the transmission unit include the encoder (both hardware and software), current modulator, and light sources shown in Figure 2.1. The core of TX is based on low cost Arduino DUE based encoder shown in Figure 2.2, which is controlled and programmed by open source C++ software. Arduino DUE [39] is a 32-bit ARM microcontroller having 54 digital input/output pins, 12 analog input pins, 2 digital-to-analog converting (DAC) output pins, 512 kB divided in 2 blocks of 256 kB flash memory for storing code, the available flash memory is 96 kB which is also divided into two parts of 64 kB and 32 kB, 84 MHz clock and 4 universal asynchronous RX-TX ports are available. Maximum voltage required by Arduino DUE is 3.3 V, applying higher voltage could damage the board. It can be connected via micro-USB cable with any computer/laptop. The Arduino DUE based encoder is used to transmit packets at different baudrates using Manchester or UART encoding scheme.

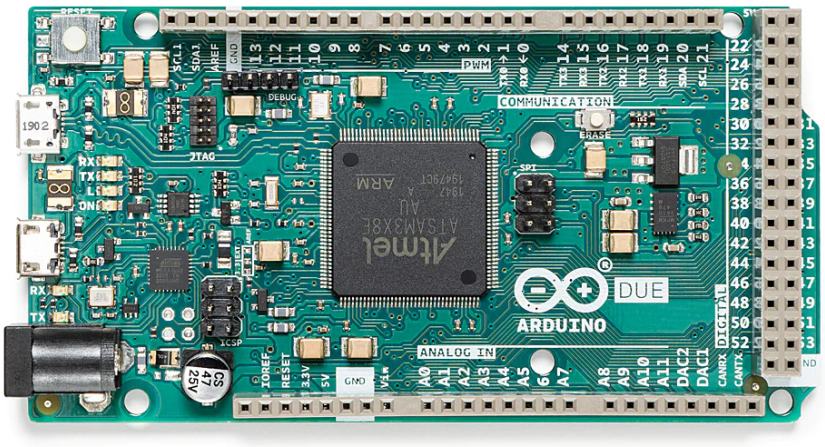

Figure 2.2: Image of Arduino Due board.

On Arduino DUE board four serial ports UART0, UART1, UART2, and UART3 are available. Among these four available ports UART0 is used for establishing connection and communication between Arduino DUE board and a computer. UART1 and UART2 were used for VLC communication, among these two UART1 was used for reception of data, whereas UART2 is connected to current modulator to drive the LED annd transmit data. UART3 is used to communicate with Zigbee board used to set the communication parameters and synchronise both Arduino based RX and TX. This port is only used for resetting the parameters of the both boards like number of messages, rebooting the boards, and required baudrate.

Moreover, I will now discuss the packet formation in the software sent to evaluate the communication performance through packet-error-rate (PER) measurements. The software was developed, which enabled bytewise analysis. The packet consists of 72 bits, of which 24 pre-equalization bits required to stabilize the signal, a 32-bit reference message, and 16-bit preamble. If these preamble bits were received correctly, the system evaluates the following

bits. Otherwise, the packet was considered lost due to a synchronization error. The end transmission includes 124 bits. The system inserts a delay after every 72 bits (1 packet) depending on the baud rate. Once the end transmission is received, the decoder prints the result on screen, including the total number of sent bits and correctly received bits.

2.1.1 LED Current Driver

LEDs are widely used in VLC systems for both illumination and communication purposes. To achieve this dual functionality, a current driver is necessary to regulate the intensity of the LED light source in accordance with the supplied current. The current driver not only provides a constant DC level but also adds a modulated signal from the encoder stage, which is used to switch on the light source at the nominal current during communication. It is important to note that existing LED drivers should support VLC without compromising the quality of illumination. LEDs have low resistance and are sensitive devices, which means that current drivers should not overdrive them. However, the drivers need to be fast enough to execute light source modulation that is imperceptible to the human eye. This presents a significant challenge in driving and controlling the intensity of the light source. In this context, an ideal LED current driver should exhibit the following characteristics:

a) Large bandwidth (BW): The -3 dB bandwidth of the current driver should be sufficiently wide to alter the frequency BW of the light source, ensuring accurate and efficient modulation for communication.

b) Long lifetime and low power consumption: The current driver should have a long operational lifetime while consuming minimal power, ensuring the overall efficiency and durability of the VLC system.

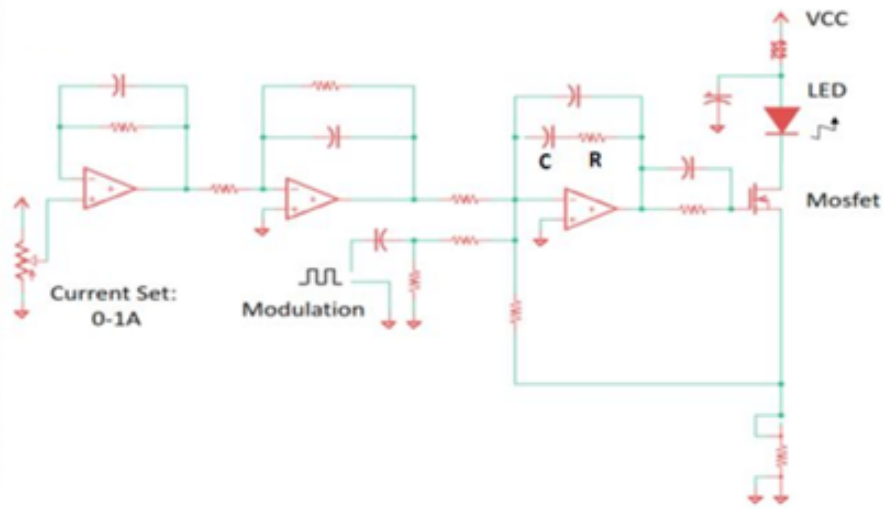

Figure 2.3: Schematic diagram of LED current driver. Reproduced from [2]

Meeting these requirements for LED current drivers is crucial in achieving optimal performance and reliable communication in VLC systems. In this research activity current modulator with 2 MHz of bandwidth is used to drive the LED and provides AC modulation to modulate (0-200%) the intensity of the source. LED driver shown in Figure 2.3 adds modulated data coming from decoder with a DC which is used to turn ON the light source. The LED driver is based on high-speed OP467 operational amplifier from Analog Devices having unitary-gain BW of 28 MHz, slew rate of 170V/µs and setting time of less than 200 ns to 0.01%.

2.1.2 Light Source

VLC explores light sources exploiting the visible band of EM spectrum which is typically from 400 nm to 800 nm. A wide range of light sources such as LASERS, blue-LEDs, and micro-LEDs exploiting the visible band are used in different applications of VLC. In this thesis, commercial LED light sources (shown in Figure 2.4) were used for experiments discussed in following chapters. Analog and digital BW of each light source was measured at their nominal current values. The cutoff frequency of each light source is defined as the frequency value for which the signal amplitude decreases by -3 dB with respect to its DC

value.

Figure 2.4: Images of main light sources used in experiments: a) 405 nm collimated light sources; b) automotive WLED; c) museum spotlight.

An arbitrary function generator (Siglent SDG6022X) was used to provide a square wave signal to the light source, the optical signal (OS) was collected by APD (thorlabs APD 430A/M) and acquired by digital oscilloscope (Siglent SDS1204X-E). The frequency of the signal was increased step by step and peak-to-peak value of the signal was considered until the signal amplitude lowers by the factor of $\sqrt{2}$ (corresponding to -3 dB) with respect to reference signal.

2.2 Receiver

2.2.1 Photodetectors

In this research work, two variable gain silicon PDs were utilized. To improve the performance of the RX, an AC-decoupling stage was integrated between the PD and the transimpedance amplifier (TIA) stage [40]. The AC-decoupling stage was designed with specific parameters to effectively filter out low-frequency stray light components that may be present in the incoming OS. By selectively attenuating these stray light components, the AC-decoupling stage helps enhance the quality and reliability of the received OS, reducing the impact of interference and noise. Overall, the integration of the AC-decoupling stage between the PD and TIA is aimed at improving the RX's ability to accurately capture and

process the desired OS while minimizing the impact of undesired stray light components.

Figure 2.5: Image of Photodetectors. a) Photograph of Thorlabs PDA100A2. b) Photograph of Thorlabs APD 430 A/M (c) Photograph of the Hamamatsu S3588-09 connected to the PDA100A2 TIA, used to collect the light from a thin FC slab.

The Thorlabs PDs used in the research, specifically the PDA 100A2 (wavelength 320 - 1100 nm, active area 0.9 mm, switchable gain) and Avalanche Photo Diode (APD) 430 A/M (wavelength range 400-1000 nm, active area 0.5 mm, variable gain) shown in Figure 2.5, possess several desirable qualities. These include low-offset, high-gain, and low-noise trans-impedance amplifiers (TIAs). The gain of the PDs is variable and can be adjusted using a movable knob. It's important to note that as the gain increases, the BW of the PD decreases as shown in Figure 2.6. These qualities make these PDs suitable for the research work, as they provide the necessary performance parameters for efficient signal detection and processing in the VLC system. In FC experiments PDA100A2 was customized by replacing original PD with an S3588-09 silicon PD by Hamamatsu having wavelength range between 340-1100 nm keeping the original TIA stage. This changing was done so that PD size (L = 30mm , d = 3mm) can match the one of the side of FC.

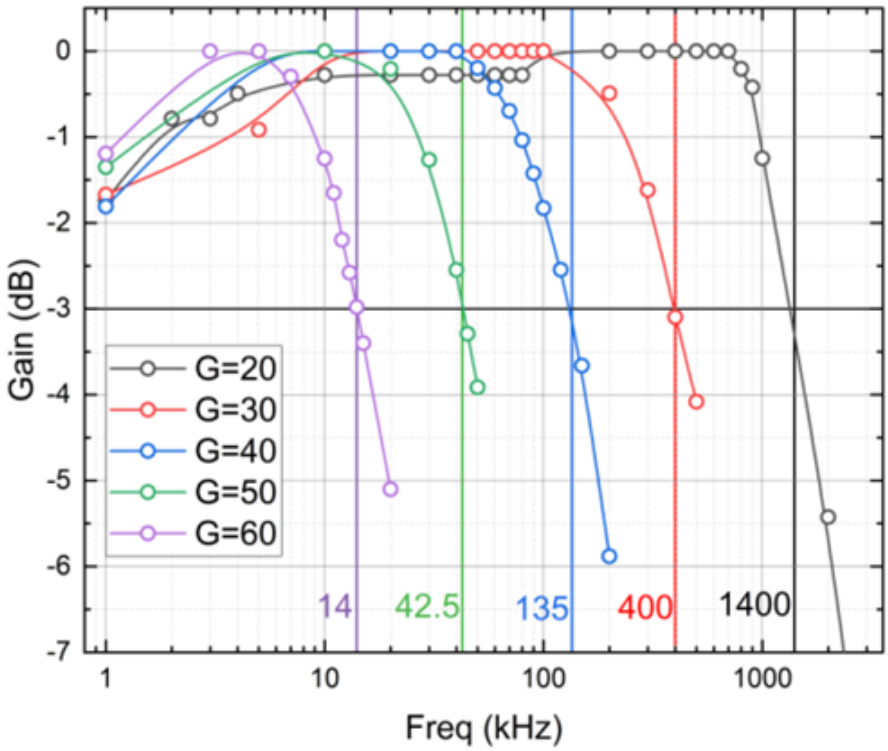

Figure 2.6: A graph illustrating the different digital BWs corresponding to various gains of the photodiode (PD), comprised of the Hamamatsu S3588-09 PD and Thorlabs TIA, is presented. Reproduced from [2].

2.2.2 Comparator Stage

The analog signal from PD passing through TIA stage is digitized by a comparator stage based on high precision comparator LT1016 shown in Figure 2.7. This comparator posses high BW/gain product and it responds very efficiently to low-level signals, this allows its BW in the order of several MHz. Moreover, the signal coming from TIA posses an average value close to 0 V therefore a variable DC offset was added with the analog signal from PD and it was compared with reference value of 1.6 V. Moreover following the configuration of Schmitt trigger there was hysteresis of 250 µV realized through resistors R2 and R5 to prevent the background noise continuously commuting the comparator thereby increasing its stability.

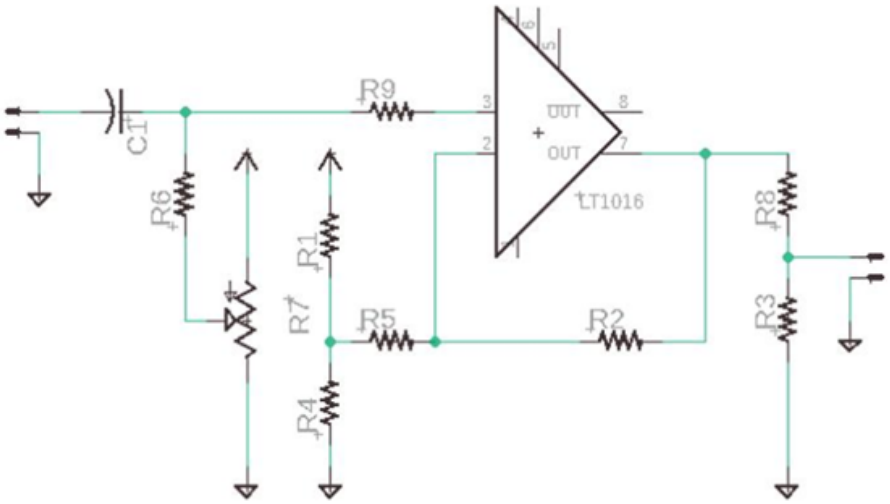

Figure 2.7: Schematic diagram of comparator. Reproduced from [2]

The Schmitt trigger is a comparator which compares the analog signal with a threshold value which is 1.6 V in this case and transforms the analog signal into digital binary output (0,1) depending on whether the analog signal is above or below the reference threshold value.

2.2.3 Decoder

The comparator stage is followed by the decoder stage, used for decoding the received message and calculating PER. The encoder allows a bytewise decoding and comparison of the encoded data packets with already stored message and checking the length of preambles (16 bits "0"). Each time the signal is received at the transmission pin the system remains idle for the time proportional to the each bit time, which varies for each different baudrate. During this time the system reads the received bits and compares it with the pre stored message, and if the message sent was received correctly the counter is increased by one, the same process is repeated for each received bit. After the reception of ending string the results are printed on the screen showing number of packets with a correct preamble and correct message, total bits sent.

Chapter 3

Fluorescent Concentrator antennas for Optical Wireless Communications

In this chapter, I will discuss in detail the conventional optical concentrators (OCs) used in OWC and their advantages and limitations. Further, I will discuss novel FC antennas to overcome the limitations experienced by conventional OCs. In my doctoral research, I worked on designing and developing FC-based novel OAs. The experimental campaign and analysis of the proposed OAs will be discussed in detail in the following chapters.

3.1 New Optical concentrators for VLC. Why?

3.1.1 High Bandwidth

The initial experiments incorporating fast LEDs and LASER diodes TX were conducted in a lab setting under a strictly controlled environment, resulting in a very short link distance [41, 42]. Furthermore, white LEDs (WLEDs) are primarily composed of fast blue LEDs and a yellow phosphor coating. The phosphor coating converts some blue LED light into yellow, inherently reducing the LED's BW to a few megahertz [43]. Typically, an optical blue filter is employed to remove the yellow component of the white light before detection.

Researchers in [44] have successfully achieved high-speed white light communication (WLC) by incorporating a blue filter to eliminate the slow yellow component. Moreover, the system's BW can be improved through advanced equalization and modulation techniques [45, 46, 47].

However, optical filtering may only be effective when high BW is necessary, as is often the case in IoT scenarios [48, 49]. The blue filter restricts most of the wavelengths in the white light spectrum, allowing only the blue portion to pass through. This leads to a significant waste of optical power from the LED source, limiting the establishment of long-distance WLC links [50]. In this scenario, optical RX architecture requires high BW and long-distance OWC links simultaneously.

3.1.2 High Optical Gain

An optical beam broadens as the link distance increases; this phenomenon is known as spatial beam divergence. Maximum channel capacity depends on BW and SNR at the RX, as described in [51]. Principally, a large SNR could be attained by collecting a significant fraction of light at the RX coming from TX. In order to maintain a good SNR, the PD at the RX stage must be large enough to collect the large portion of incoming optical beam. Doing so also results in higher parasitic capacitance, which will reduce the intrinsic BW of the PD [34].

Additionally, typically OWC requires Line-of-Sight (LoS) between TX and RX to maintain an effective communication link. As the active area of the PD is very small, a minimal hindrance/movement due to different phenomena like atmospheric turbulence, mechanical vibration, and pointing errors in TX or RX can affect the communication [52]. Once the hindrance between TX and RX has been removed and LoS is maintained, communication is resumed. Several techniques are proposed in [53, 54] to mitigate the misalignment issues, such as adaptive optics, but this makes the system bulky and costly. Additionally, very complex tracking and positioning algorithms are used to realign the TX and RX by tracking the optical beam to ensure that maximum optical power is received at RX [55, 56]. However,

these complex algorithms increase the computational cost. In order to relax misalignment issues without the implementation of complex algorithms, one way is to increase the collection area of the RX stage so that maximum optical power is received at the RX. As described earlier, if the active area of a PD is increased, BW will decrease. To control the area-BW effect, an array of small PDs with large BW is employed at the RX instead of a single PD [57, 58]. By adopting such a solution, the OG of RX stage is increased but at the cost of more power consumption and complexity, which is not desirable in most of the low-power IoT applications [59, 60].

3.1.3 Conventional Optical Concentrators

Already realized approach for achieving a high BW and SNR involves the utilization of OCs coupled with PD at the RX. Typically, two types of OCs called parabolic concentrators (PC) and compound parabolic concentrators (CPC), are used with small PD to increase OG at the RX. The fundamental concept behind OCs is that they gather incoming light across a broad collection area and concentrate it onto a smaller PD.

OCs like PC and CPC depend on reflection and refraction of light and therefore conserve etendue [61], a geometric property that quantifies the extent of light spreading in terms of both area and angle. The maximum achievable geometric gain is given by [61]

$$\mathrm{G_{max}} = \frac{n^2}{sin^2\theta_{\mathrm{max}}} \tag{3.1}$$

where in Equation 3.1 $\mathrm{G_{max}}$ is maximum gain, n is the refractive index and θ_{max} shows the maximum possible incidence angle. The limitations caused by conventional optics make it essential to develop new RX stages with large collection areas, high OG, large BW, and relaxed misalignment issues. In the context of the challenges mentioned above, recently novel antennas based on fluorescent concentrators (FCs) have gained a lot of attention [36, 37, 38]. FCs are optical wave guides usually doped with different kinds of fluorophores [62, 63], and

they are not limited by conservation of etendue as reported in [61].

3.2 Luminescent solar concentrators

The history of the idea of FCs can be traced back to the Luminescent solar concentrators (LSCs).

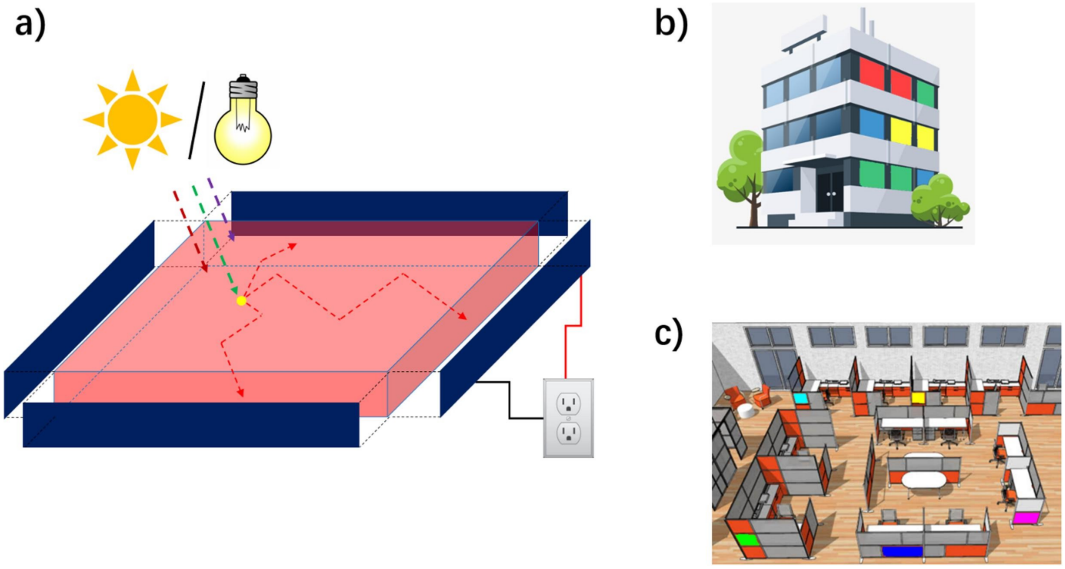

Figure 3.1: Schematic representations of (a) the operational mechanism of an LSC, and the application of the LSCs in (b) a building envelope and (c) an office area. Reproduced with the permission from [64].

These large-area concentrators were introduced initially to replace the expensive and bulky large-area solar cells in the 1970s. The main idea of LSC is that as solar cells are very bulky and expensive and block the incoming sunlight; it was proposed to develop less expensive concentrators, which are also light in weight. Initially, the development of LSC was prolonged due to the low performance of available dyes. After few years, the performance of organic dyes and Quantum dots (Q-dots) was studied. The working principle of LSC is that photovoltaic cells (PV) are coupled at the edges of the LSC, incoming light is collected and wavelength converted by the LSC, and due to total internal reflection, it is wave-guided towards PV at the edge. This concept of harvesting energy is unique as these LSCs can also

be integrated into the windows of buildings where they harvest energy and allow sunlight to illuminate the buildings simultaneously, as shown in Figure 3.1. Large LSCs are preferred as they have a large collection area to increase the OG.

3.3 Fluorescent Concentrator

Fluorescent concentrators (FCs) refer to slabs doped with fluorophores. While FCs are commonly used interchangeably with LSCs, their applications extend beyond solar energy harvesting. The working principle of FCs entails the collection of incident light by the largest surface area of the FC, where a fraction of the light is absorbed by the fluorophore material. This doped material typically absorbs light in the UV region of the EM spectrum and emits light at longer wavelengths. This conversion from shorter to longer wavelengths is known as the Stokes shift [65]. The high refractive index of the slab causes the absorbed light by the fluorophore to be wave-guided towards the edges within the slab until it reaches the PD attached at the sides of the FC as shown in Figure 3.2

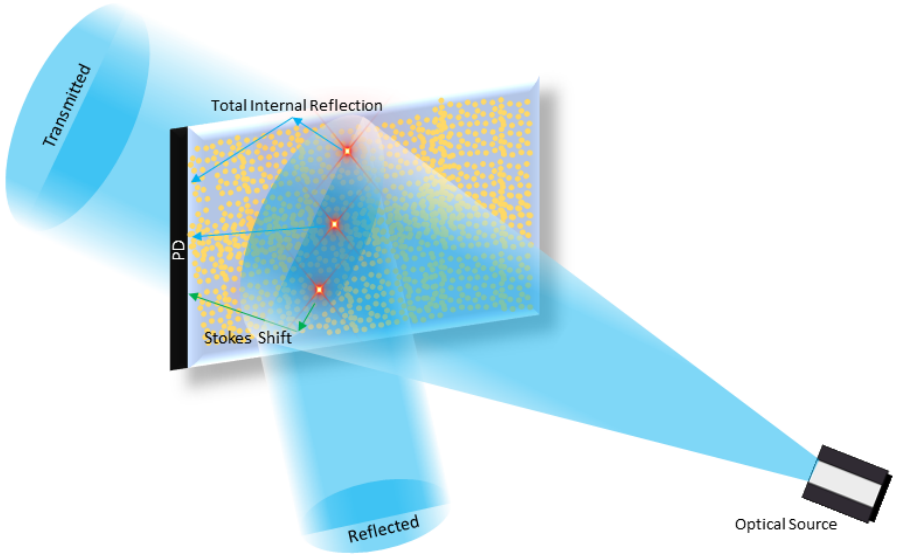

Figure 3.2: Model diagram of fluorescent concentrator with PD attached at the left edge

As previously mentioned, FCs incorporate fluorophores that absorb incoming light, and the effectiveness of the FC depends on the specific fluorophore used for doping [66]. Gener-

ally, fluorophores are classified into two main classes: organic and inorganic. Properties of some of the widely used fluorophores are listed in Table 3.1. Electrons inside the fluorophore have discrete energy levels in the ground state (E_0) and excited state (E_1). When the incoming photons are absorbed by the electrons in the ground state, they shift the electron to an excited state. After a certain time, the energy is released/emitted by the electrons, and electrons go again to the ground state. The average time taken by the electron to go from an excited state to a ground state is called a lifetime. Different fluorophores have different lifetimes; usually, few of them are in the range of nanoseconds (ns) [6]. The number of fluorescence emitted photons is usually less than the number of absorbed photons, as they may get absorbed or lost. The ratio of the number of photons being emitted to the number of photons being absorbed is called quantum yield (ϕ), which is given in Equation 3.2 [67].

$$\phi = \frac{\text{number of emitted photons}}{\text{number of absorbed photons}} \tag{3.2}$$

Fluorophore	Absorption (nm)	Emission (nm)	lifetime (ns)	Applications
Rohdamine B	540	565	2.41	Fluorescence imaging
Coumarin	380-480	430-500	1.5	Medical studies, VLC
Q-Dots	430	770	depends on Q-dots	Solar energy harvesting, VLC
Lumogen Red	574	611	6.5	VLC ,textiles
Texas Red	589	615	4.2	Biological and biochemical application
BODIPY	depends on solution	depends on solution	1	Cellular Imaging, VLC
Quinoxaline	430	546	≈ 1.5	VLC

Table 3.1: List of different fluorophores and their properties.

3.3.1 Fluorescent Concentrator Gain

Gain of FCs depends on different factors, which are discussed here in detail. Fluorescence emitted photons are emitted isotropically some of them are trapped inside the FC due to total

internal reflection and other escape the FC. This critical angle is set by the refractive index of the substrate and the doped fluorophore. A portion of these trapped photons propagates towards the PD coupled at the edge of the FC. However, the performance and gain of FCs are limited by different factors. Firstly, only a considerable portion of light is absorbed by the FC. This absorption depends on the doped fluorophore material's concentration and the slab's thickness. After the absorption of photons, only a certain fraction of photons is reemitted. In addition to these factors, a fraction of remitted photons will escape the FC [6]. Furthermore, depending on the Stokes shift, a difference between absorption and emission spectra, a portion of photons is reabsorbed by the fluorophore [68]. The overall gain of FC is given by Equation 3.3 [69]

$$G = \eta_{\text{enter}} * \eta_{\text{abs}} * \phi_{\text{QY}} * \eta_{\text{det}} * G_{\text{geo}} \tag{3.3}$$

where η_{enter} is the probability of photons entering in FC which is also called Fresnel transmission coefficient, η_{abs} is the probability of photons to the absorbed in FC, ϕ_{QY} is the quantum yield explain in Equation 3.2, G_{geo} is geometric gain of FC which is given in Equation 3.4

$$G_{\text{geo}} = \frac{A_{in}(\text{input area of FC })}{A_{out}(\text{output area of FC })} \tag{3.4}$$

3.4 Related Studies

In 2014 researchers conducted first study for the utilization of FC in OWC [61] and achieved 1 Gb/s using OOK modulation scheme. The most important experiment proving the proof-of-concept of using FCs in VLC is realization of FC antenna with doping of Coumarin 6 as a fluorophore [37]. In this research work, researchers achieved maximum OG of 12° while also getting a full width at half-maximum FoV of 120°, in comparison of CPC with the same FoV a maximum OG of 3° was expected. Moreover, the effective receiving area of OAs can be

significantly enlarged while still maintaining substantial bandwidths and reduced sensitivity, compared to standard optical condensing systems [70]. This approach holds the potential to revolutionize the integration of FC OAs in the VLC RX stage, as FC OAs can be seamlessly incorporated into devices like laptops and mobile phones [71]. As mentioned earlier, FCs offer advantages in terms of relaxed misalignment issues and can alleviate the need for complex pointing and tracking systems in FSO communication [72], making them attractive for long-range VLC applications as well [73]. Pioneering efforts have demonstrated the successful transmission of data at very high baud rates, reaching several Gb/s, by carefully selecting fluorophores with shorter fluorescent lifetimes and employing planar-shaped FC OAs [61]. Furthermore, wide FoV FC-based VLC systems have been reported in [37] reporting FOV up to 60°.

In most cases, FCs are constructed using organic fluorophores (OFs), originally developed for different purposes, but also exhibit suitable optical properties that make them suitable for VLC applications, including visible spectrum absorption and strong fluorescence. The commonly used OF is Coumarin 6 [70, 74, 75] which exhibits excellent optical properties but faces challenges with compatibility in polymeric matrices and stability [76]. Less effective OFs include BODIPY derivatives [77], known for their low fluorescence, and pentaphenylenes [78], which absorb light below 400 nm and cannot be utilized with white LEDs. Recent comparative studies in [79] have investigated the time response of various FCs in VLC applications, exploring alternative geometries beyond simple planar structures. For instance, in [34], non-planar spherical geometries have been realized using fluorescent flexible fibers that absorb ultraviolet light (< 405 nm), and flexible nanostructured FCs in [72] have been demonstrated, both utilizing violet LEDs as transmitters [80]. While recent results have pointed out limitations of UV-absorbing fluorescent fibers as RX stages in white-light VLC systems, most FC-based OAs still primarily focus on Blue-UV LED sources [79]. Efforts have been made to develop FC OAs, including the design of multi-layer OAs for wavelength division multiplexing (WDM) in the blue and green regions of the visible spectrum [74].

Another design utilizes three commercially available fluorescent fibers [81], each selectively absorbing different wavelength ranges to cover the spectrum of a WLED. Additionally, a simulation-based concept for an OA integrating three distinct fluorophores has been proposed in [82], although experimental validation of this approach is yet to be reported.

Within this thesis, I contributed to the analysis and development of OAs with three different fluorophores. In Chapter 4, a reliable long-distance VLC link exploiting very large OAs based on $CuIS_2$ (CIS) Q-dots is established and discussed. The absorption and emission ability of photons in FC depends on the type of fluorophore used. As said earlier majorly fluorophores are divided into two main classes: organic and inorganic fluorophores. FC made up of organic fluorophores shows excellent properties, but their performance decreases with time due to environmental effects. On the other hand, inorganic fluorophores are stable in the environment and can be an excellent candidate for the FC-based VLC systems. Q-Dots belongs to the inorganic family; they are nanoscale semiconductor materials that exhibit unique optical and electronic properties due to quantum confinement, a phenomenon observed in nanoscale semiconductor materials in which the motion of charge carriers is confined in three spatial dimensions. For the full deployment of FC-based VLC systems in real-world scenarios, it is crucial that the performance of these systems is thoroughly assessed in well-illuminated environments. However, there have been limited studies demonstrating the capabilities of the FC-based VLC RX stage in a partially illuminated environment [83]. No study is done under a full illumination environment, such as under direct sunlight. The absence of such investigations highlights a gap in characterizing FC-based VLC RX technology in terms of photostability and its ability to establish reliable links under direct sunlight, effectively filtering out unwanted low-frequency interference. As far as our knowledge extends, this marks the first comprehensive examination of FC-based RX stages under such conditions. The successful demonstration of the FC-based VLC RX stage utilizing photo-stable, large-area FC optical antennas suitable for real-world operations and achieving practical distances would be a significant milestone in advancing the widespread

adoption of VLC technology. It also holds the potential to greatly impact long-range OWC applications, encompassing LED and laser sources in both UV and IR wavelength ranges.

Furthermore, white light typically exhibits intrinsically reduced BW due to the presence of layer of phosphorous which converts a portion of blue light into yellow reducing the BW [84]. BW of WLEDs can be increased by applying an optical filter at RX which filters out yellow portion of light [44] but it also reduces the overall optical power received at the RX, negatively impacting the attainable haul for WLC links. In this context a VLC RX is important for WLC which is able to receive maximum optical power with intrinsically high BW. In Chapter 5, OAs with two different organic fluorophores namely Lumogen Red© 305 F (LR305) a well-established benchmark in LSC applications [85, 86], and a recently synthesized quinoxaline chromophore (DQ1) that exhibits excellent optical properties are studied [87] for WLC. The spectral features of these two chromophores are different: DQ1 has a prominent absorption peak at 430 nm and emits light with a large and broad Stokes shift (ϕ), whereas LR305 absorbs light with a smaller Stokes shift over a larger portion of the solar spectrum. Finding the best optical antenna for WLC applications requires comparing the performance of these two fluorophores with WLED sources.

Chapter 4

Quantum-Dots based Fluorescent Concentrator Antenna for Long-range OWC

Q-Dots possess remarkably high photoluminescence (PL) quantum efficiency [88] and can be customized to selectively absorb specific wavelengths [89]. Additionally, Q-Dots exhibit minimal re-absorption losses compared to organic dyes, thanks to their controllable and engineered Stokes shift [90]. They are the greatest candidates among the others [61] due to their ability to have lifetimes as low as 1-ns [91]. Q-Dots are far more photo-stable than the vast majority of organic dyes used in earlier works, allowing for the creation of large-area FC appropriate for outdoor applications involving prolonged exposure to direct sunshine. Common Q-Dots used earlier for high-performance FC embed highly toxic heavy metals like Cd, Pb, and Te as discussed in [92, 93].

In this thesis, I studied large-area FC antenna constructed using $CuInS_2$ colloidal Q-Dots, which are combined with a ZnS shell and dispersed within a Polymethylmethacrylate (PMMA) slab. This FC has been developed by the company Glass to Power, Milan, in collaboration with the University of Milano-Bicocca. The development of the Q-Dots FC

slab is not part of my research. I only used these slabs in my study for VLC. However, I am providing a brief introduction to the production process of these slabs. These nanocrystals exhibit a significant absorption-emission Stokes-shift and relatively rapid excited state lifetimes, making them highly suitable for large-area OAs employed in fast-communication devices. Additionally, recent studies have demonstrated their exceptional stability when exposed to direct sunlight [94, 95]. The procedure described in [94] was utilized to synthesize $CuInS_2$ Q-Dots by employing a specific heat-up method. This thesis provides comprehensive information about the synthesis process, including a detailed characterization of the Q-Dots photoluminescence efficiency (approximately 80%), TEM images, and analysis of particle size distribution. Subsequently, the Q-Dots were incorporated into a PMMA slab through a bulk polymerization technique using an industrial cell-casting process.

4.1 CIS Q-Dots as Fluorophore

The synthesis process consists of two steps. In the first step, the MMA monomer was heated to a temperature of 80 °C. Once the temperature stabilized, 100 ppm w/w of an organic compound azobisisobutyronitrile (AIBN) was added. This initiated the pre-polymerization process, causing the monomer temperature to rise until it reached the boiling temperature of MMA (around 90 °C). Once the monomer reached a state of vigorous boiling, it was rapidly cooled down to room temperature. In the second step, the resulting prepolymer underwent degassing through freeze-pump-thaw cycles. Following this, the Q-Dots were added to the prepolymer. Afterward, the prepolymer was introduced into a casting mold while being exposed to a continuous flow of argon. The mold was then placed in a water bath set at a temperature of 550 °C for a duration of 48 hours. Following this step, the slab was post-cured by placing it in an oven at a temperature of 115 °C overnight. Once the slab had cooled down, it was laser-cut to the desired dimensions and its edges were carefully polished. Finally, the prepolymer was injected into the casting mold under argon flow and heated to

550 °C for 48 hours. The slab was then post-cured in the oven overnight at 115 °C. After cooling, slab were laser-cut to the proper size (38.4 x 6.8 x 0.3 cm^3) the slab's edges were polished, and it was laser-cut to the required dimensions. The resulting FC collects the incident light over a sizable area, transforms it into fluorescence, and directs the radiation produced to the edges where it can be captured by a PD (see Figure 3.2).

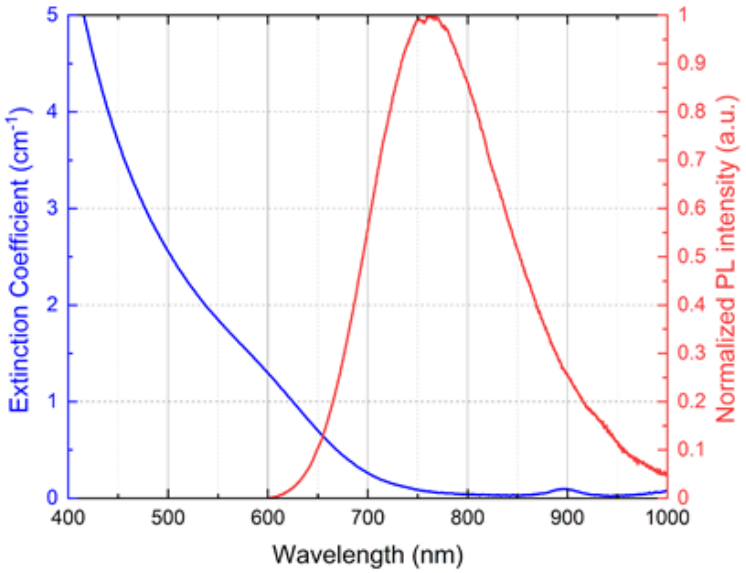

Figure 4.1: Measured extinction coefficient (blue) and normalized PL spectrum (red).

Figure 4.1 displays the sample fluorescence measured with a Hamamatsu TM-VIS/NIR C10083CA mini spectrometer upon illumination at 532 nm and the observed absorption spectra recorded with a Varia Cary 50 spectrometer. The data show a broad absorption that spans the entire UV spectral range and places no restrictions on the excitation wavelengths, as well as an emission peaking at approximately 770 nm with a Stokes shift as significant as 400 meV, which minimizes the re-absorption and enables the realization of large-area devices. Using the time-correlated single-photon counting (TCSPC) approach, fluorescence decays in the time domain are computed [96]. A 405 nm laser source (Edimbourg EPL-405) with a pulse duration of less than 100 ps excites the sample. A Hamamatsu R943-02 photomultiplier coupled to an Ortec 9353 multichannel scaler is used to detect the photons released by the sample in photon-counting mode. Overall, the timing resolution was superior

to 1 ns.

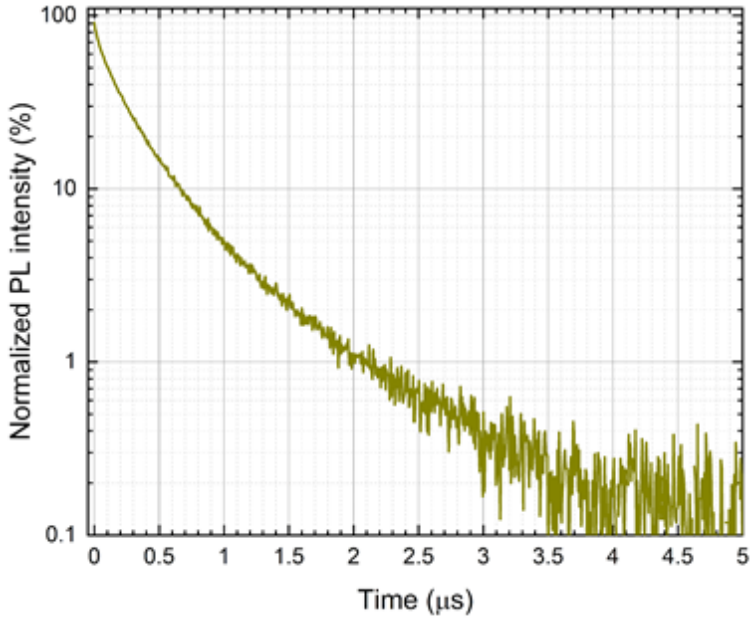

Figure 4.2: Time resolved photo-luminescence decay

The TCSPC results are shown in figure 4.2. With an average $1/e$ lifespan of roughly 300 ns, the fluorescence decay exhibits a slightly stretched behavior, as is typical for colloidal Q-Dot ensembles. This could have significant impact on VLC BW, as I will show later.

4.2 Experimental Setup

4.2.1 Integration of FC antenna in VLC RX stage

A rectangular Si PIN PD (Hamamatsu S3588-09, Figure 4.3), with an active area and low parasitic capacitance, is placed in correspondence with one of the short edges of the slab's middle point to integrate the antenna into the custom RX stage (Figure 4.3). The slab thickness (3 mm) fits the short side extension of the PD to maximize light collecting and reduce coupling losses. The width and height are respectively $w = 38.4$ cm and $h = 6.8$ cm (Figure 4.3). As the slab's height h partially exceeds the PD's size, part of the converted light escapes from the short side of the OA.

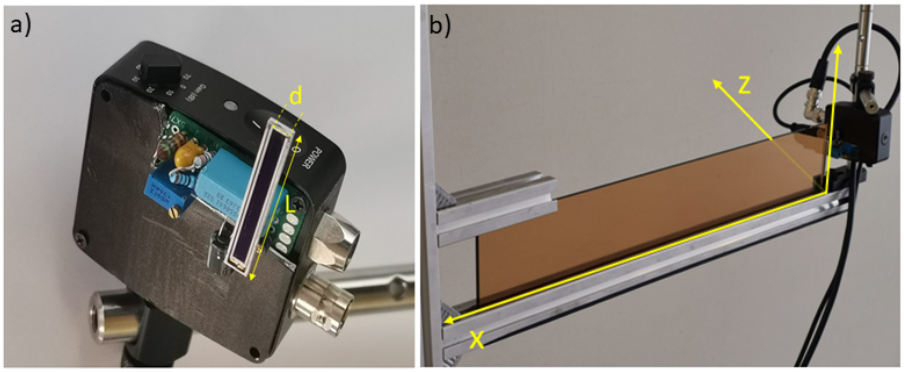

Figure 4.3: FC based OA: (a) Custom photodiode used to couple (b) FC edge View of the VLC optical RX based on fluorescent concentrator.

To address this undesired effect, one potential solution is to apply a reflective coating to the uncovered portions of the collection edge. By doing so, the reflective coating would help to redirect the escaped light back towards the PD, thus enhancing the system's overall light collection efficiency. In the setup illustrated in Figure 4.3, the photocurrent produced by the PD is amplified and converted by a custom TIA amplifier (TIA) stage as described in section 2.2. To achieve this, a commercial variable-gain PD (Thorlabs, PDA100A2) was modified by replacing the original PD with the Hamamatsu S3588-09 used in the previous steps. The custom modification allows for integrating the TIA stage, which amplifies the photocurrent signal and converts it into a corresponding voltage signal for further processing and analysis.

The customized TIA stage additionally incorporates a specific AC pre-filter stage as discussed in section 2.2 has a maximum BW (-3 dB) of 12 MHz for minimum TIA gain G = 0 dB, whose architecture excludes undesired light components at frequencies below 1 KHz, like stray artificial illumination or sunshine [97]. The risk of DC saturation in the TIA stage is significantly decreased by this feature. Additionally, the FC's absorption spectrum, which is shown in Figure 4.1, aids in lowering the system's response at wavelengths $\lambda > 500$ nm, which protects from solar irradiance. To use our RX stage for VLC under direct sunlight without significantly degrading the SNR value, the combination of the properties mentioned above is necessary.

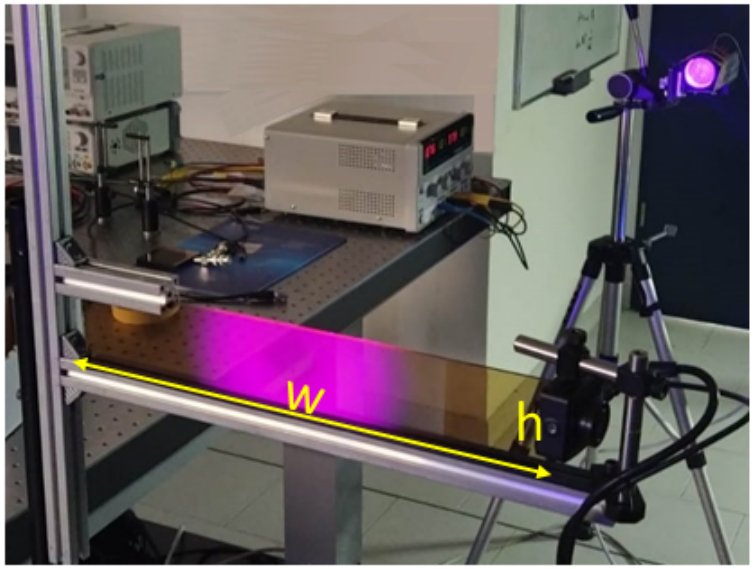

Figure 4.4: View of FC optical receiver

4.2.2 Characterization of FC antenna

The experimental characterization of the FC Q-Dots antenna consists of two main parts. The first part focuses on characterizing the conversion properties of the FC, including its efficiency, wavelength dependence, and FoV. The objective is to understand how effectively the FC converts incoming light signals. The second part of the experimental campaign aims at evaluating the time response of the OA to digital signals and determine the maximum communication BW.

A small LED source at a wavelength of $\lambda = 405$ nm, which exhibits an intensity modulation BW (-3 dB) exceeding 13 MHz and with a power output of 15 mW (Thorlabs LED405E), has been employed as the optical source for these experiments. This LED source allows for the generation of digital signals and enables the investigation of the OA's performance in terms of time response and communication BW. At the wavelength of $\lambda = 405$ nm, the FC exhibits complete absorption of radiation over short distances. Consequently, only a negligible portion of the excitation radiation reaches the PD in the setup. A 200 MHz arbitrary waveform generator (Siglent, SDG6022X) with a sampling rate of 2.4 GSa/s is utilized to

drive the LED. This generator provides the necessary current (20 mA) to drive the LED, allowing for both analog and digital intensity modulation patterns. The limiting factor for the modulation BW is the parasitic capacitance of the LED substrate given in Section 2.1.

4.2.3 Dependence of the photoluminescence signal on the position of the light spot

The signal was recorded as a function of excitation distance from the edge where the PD is coupled to detect potential asymmetries associated with the position of the excitation spot on the FC. For this purpose, the small LED was placed directly in contact with the FC surface, perpendicular to the FC surface, as shown in Figure 4.5, and it was moved along the x direction. The signal amplitude was measured after the TIA stage. Section 2.2 of PD is presented in Figure 4.6.

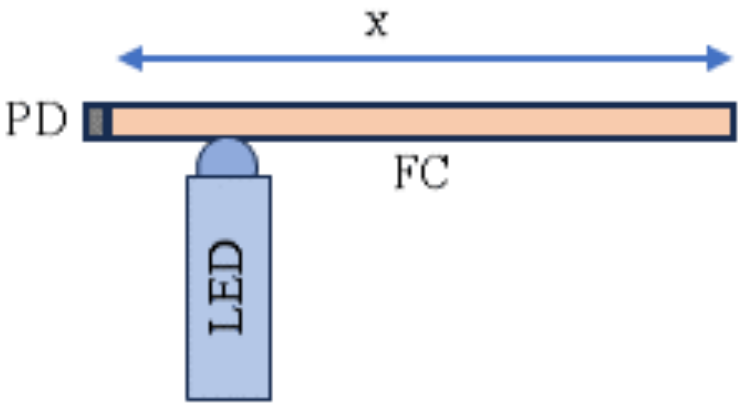

Figure 4.5: Schematic diagram of efficiency vs side displacement

The signal amplitude, recorded after passing through the TIA stage at each position, is reported in Figure 4.6. The error bars are determined as the maximum deviation observed in five consecutive measurements for each data point. In general, it is observed that the signal decreases as the x increases. However, this decrease follows an unusual pattern not typically seen in the context of embedding reabsorption-free chromophores for FC [89].

However, the data was analyzed separately for two distinct ranges: firstly, when the

excitation spot is positioned at relatively small distances from the edge (around 3-5 cm) and secondly, when placed further away. The signal reduction in the first range is primarily attributed to a geometric effect. In this scenario, the detector is smaller than the dimensions of the slab, and it captures only the photons emitted within the solid angle it can see from the excitation point. As the distance increases, this effect diminishes due to the guiding properties of the slab. Beyond a distance of 5-7 cm, the additional reduction in the signal is mainly influenced by the re-absorption occurring in the PMMA matrix and the Q-Dots.

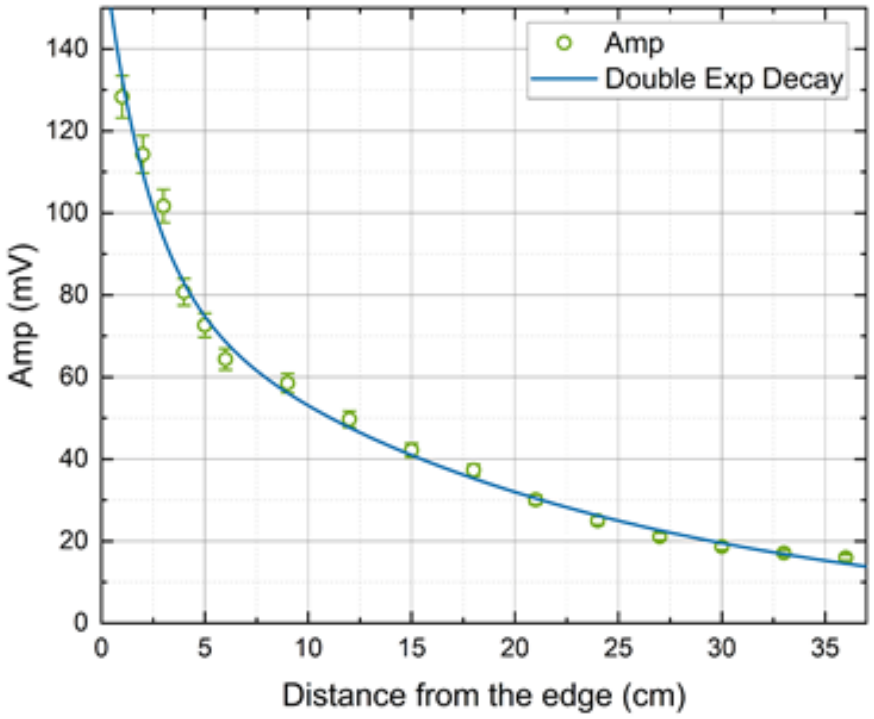

Figure 4.6: Photodetector amplitude as a function of distance from the edge and comparison with Monte Carlo model

To obtain a comprehensive understanding of this phenomenon, a Monte Carlo ray-tracing simulation was performed by Marco Fattori to model the anticipated output based on the excitation spot's position. In summary, the stochastic nature of the Monte Carlo ray-tracing method suggests that the light ray doesn't split upon reaching an interface, and its intensity doesn't gradually decrease within the PMMA slab. Instead, each photon undergoes reflection, transmission, or absorption with probabilities proportional to the energy fluxes,

as defined by the Fresnel and Lambert-Beer law [98]. The simulation's input parameters comprise the optical spectra of the PMMA slab, which is doped with Q-Dots. The simulated results are presented in Figure 4.6 and show remarkable agreement with the experimental data. This alignment is compelling evidence that the FC system under study functions precisely as anticipated, given the particular geometry and the specific Q-Dots used.

4.2.4 Field of View (FoV)

FoV is an important factor in addressing the challenge of developing optical RXs with high OG for VLC applications. The FoV of the Q-dots OA antenna is quantified and discussed in this section. This was accomplished by recording the corresponding signal amplitude after the TIA while illuminating the slab with the LED source. The FC was rotated around its central axis in the $x-z$ plane using a precision rotation stage. The angle θ between the FC's optical axis ($\hat{n}$ and the incident light direction ($\vec{k}$ in Figure 4.7 and 4.8) was scanned in steps of 10°.

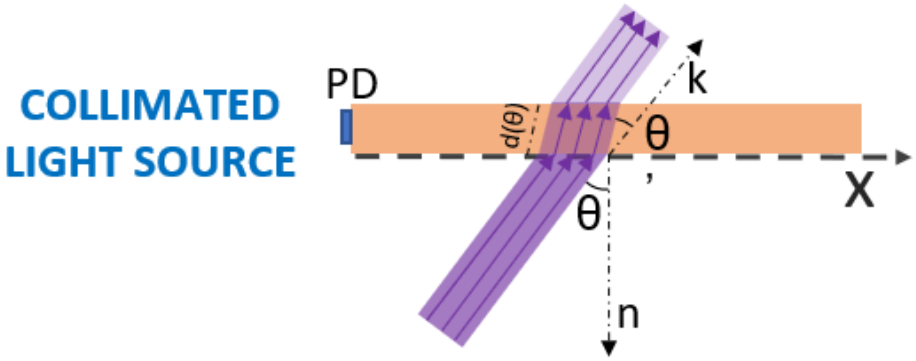

Figure 4.7: A collimated light source (*Coll*), where the light spot is collected for each angle inside the FC. $\vec{n}$ and $\vec{k}$ are respectively the incident wave vector and the FC optical axis.

Two distinct illumination configurations were considered. The first configuration, referred to as the collimated source configuration (Coll) (Figure 4.7), involved a light spot that was fully contained within the FC antenna surface. In the second configuration shown in (Figure 4.8), the extended source configuration (Ext), a dispersed light source was used

to illuminate the FC uniformly. By systematically rotating the FC and recording the signal amplitude, the FoV of the antenna was characterized under both the collimated and extended source configurations. This measurement provides insights into the angular range over which the antenna can effectively receive and detect optical signals, offering valuable information for VLC system design and performance optimization.

In the two different illumination configurations, we expect the FoV to exhibit distinct behaviors. To reconstruct the output signal corresponding to the number of photons converted by the FC and reaching the PD, we can make use of fundamental laws of optics [99], assuming a uniform quantum yield across the slab.

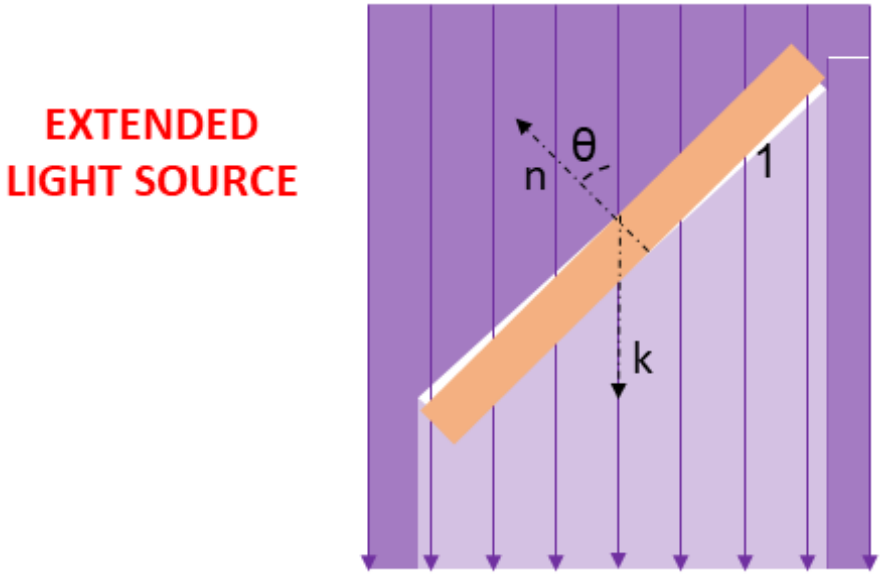

Figure 4.8: An extended light source configuration (*Ext*), where the light uniformly illuminates the FC.

Firstly, when light is incident on the FC, a portion of it will be reflected due to Fresnel's laws. Assuming non-polarized light, we can define the reflection coefficient as:

$$R(\theta) = (R_p(\theta) + R_s(\theta))/2 \tag{4.1}$$

Where in Equation 4.1 $R_p(\theta)$ and $R_s(\theta)$ are the reflection coefficients for p-polarized and s-polarized light, respectively. According to Snell's law, the optical path $d(\theta)$ traveled by a

light beam inside the FC increases with the incident angle θ. This can be described by the Equation 4.2

$$d(\theta) = d(1 - (n_1/n_2)^2 \sin^2(\theta))^{-1/2} \tag{4.2}$$

where d is optical path of beam inside the FC, n_1 and n_2 are the refractive indices of the surrounding medium and the FC substrate, respectively. Following the Lambert-Beer law, the absorption (conversion) probability in the FC substrate increases exponentially as the optical path increases. By considering these principles, we can reconstruct the output signal as a function of θ for both the collimated and extended source configurations. This analysis provides insights into the effects of reflection, refraction, and absorption within the FC, allowing us to understand the variations in the output signal concerning the incident angle.

In the extended source configuration (*Ext*), the optical power collected on the FC surface, denoted as $P(\theta)$, is influenced by the projection of the FC area onto the uniform intensity pattern of the incident light. This reduces the optical power collected compared to the orthogonal incidence configuration ($P(0°)$). The relationship between $P(\theta)$ and $P(0°)$ can be expressed as $P(\theta) = P(0°)\cos(\theta)$. This cosine function accounts for the decrease in the effective area of the FC exposed to the incident light as the angle θ deviates from 0°. Based on these considerations, we anticipate that the signal amplitude after the TIA stage should exhibit the following trend in the two illumination cases:

$$S_{Coll}(\theta) \propto (1 - R(\theta))(1 - e^{-\alpha d(\theta)}), \tag{4.3}$$

$$S_{Ext}(\theta) \propto (1 - R(\theta))(1 - e^{-\alpha d(\theta)})\cos(\theta). \tag{4.4}$$

In Figure 4.9, the recorded normalized signal amplitude as a function of the angle θ is

presented for the *Coll* and *Ext* configurations. The signal amplitudes are represented by blue and red circles, respectively. It is important to note that each amplitude measurement considers a relative statistical error of 4%. The depicted figure demonstrates that the *Coll* configuration exhibits a wide plateau for small values of θ, while the *Ext* configuration displays a more pronounced angular dependence. This contrasting behavior arises from the lack of a vignetting effect (an optical phenomenon that describes the gradual darkening or reduction of brightness at the corner of edges) for small spot sizes in the *Coll* case, as θ is varied (as described by Equation 4.4). The obtained data are compared with simulation results using Equations 4.4 (red solid line) and 4.4 (blue solid line) for the two configurations. Notably, in the *Coll* case, a non-monotonic behavior in the signal amplitude is anticipated, with a relative increase expected for $\theta \simeq 60°$. This behavior arises from the opposite trends exhibited by the optical path length and Fresnel reflection coefficients as a function of θ, leading to a relative maximum in the collection efficiency of our antenna. Conversely, in the *Ext* case, the vignetting effect consistently dominates, resulting in a continuous decrease in efficiency as θ increases. For larger angles, the contribution of Fresnel's reflection becomes predominant in both cases, causing a rapid decline in the collected signal.

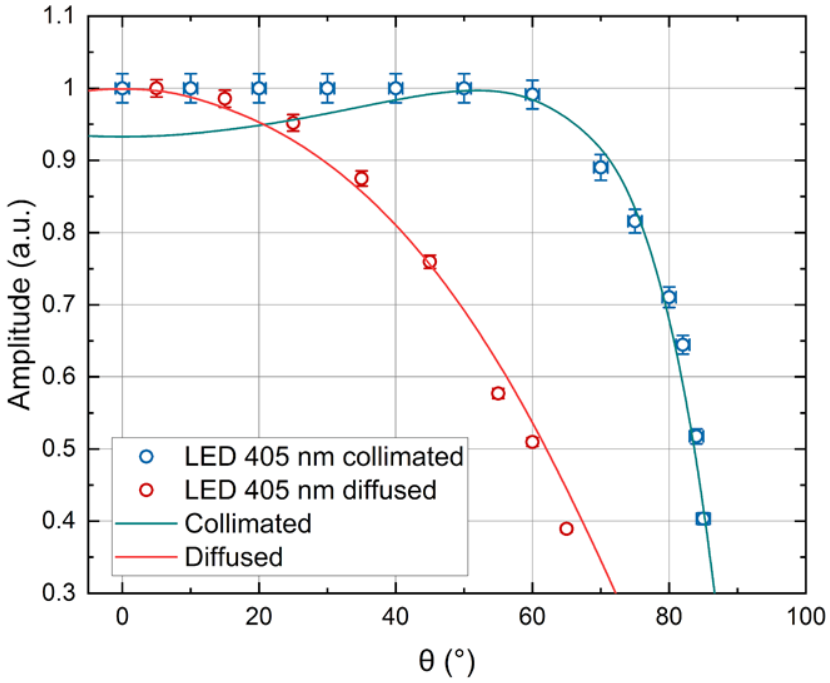

Figure 4.9: FoV measurements results for the two configurations. Red: *Ext* configuration and Blue *Coll* configuration. Dots are relative to experimental data whereas continuous lines refer to the FoV model prediction

While there is excellent agreement between the data and the model in the *Ext* configuration, a slight deviation is observed in the *Coll* configuration for small θ values. This discrepancy could reasonably be attributed to the non-ideal collimation of the LED emission pattern and residual polarization effects, which make Equation 4.4 an approximation for our specific case. The observations and modeling of RX stage highlight its significant feature of a large FoV, resulting in low sensitivity to angular misalignment. Precisely, in the *Coll* configuration, Marco Seminara estimated the FoV as the θ value at which the signal drops to 0.5 times the value observed at $\theta = 0°$, resulting in a FoV of approximately 85°. In the *Ext* configuration, which is more likely to be encountered in long-range OWC or FSO applications, the FOV is estimated to be around 60°.

4.2.5 Characterization of time response

To characterize the temporal response of the FC antenna, a square pulse with 20 ns rise and fall times was generated using the waveform generator. This pulse was used to modulate the LED light source, which was positioned in contact with the FC device at a distance of x= 2 cm. The purpose of this setup was to isolate the temporal response of the FC substrate. To measure the temporal response, the light converted by the FC antenna was collected using a fast APD from Thorlabs (model APD 430A/M) 2.2. The APD has a response time of $\tau < 3$ ns, which is much shorter than the estimated lifetime of the FC fluorophores. This ensured that the APD could accurately capture the temporal characteristics of the converted light. Figure 4.10 presents the recorded temporal response of the FC antenna captured by the APD. The rise and fall times were determined by measuring the time interval between 10% and 90% of the output step height, resulting in estimated rise and fall times of 1.8 μs.

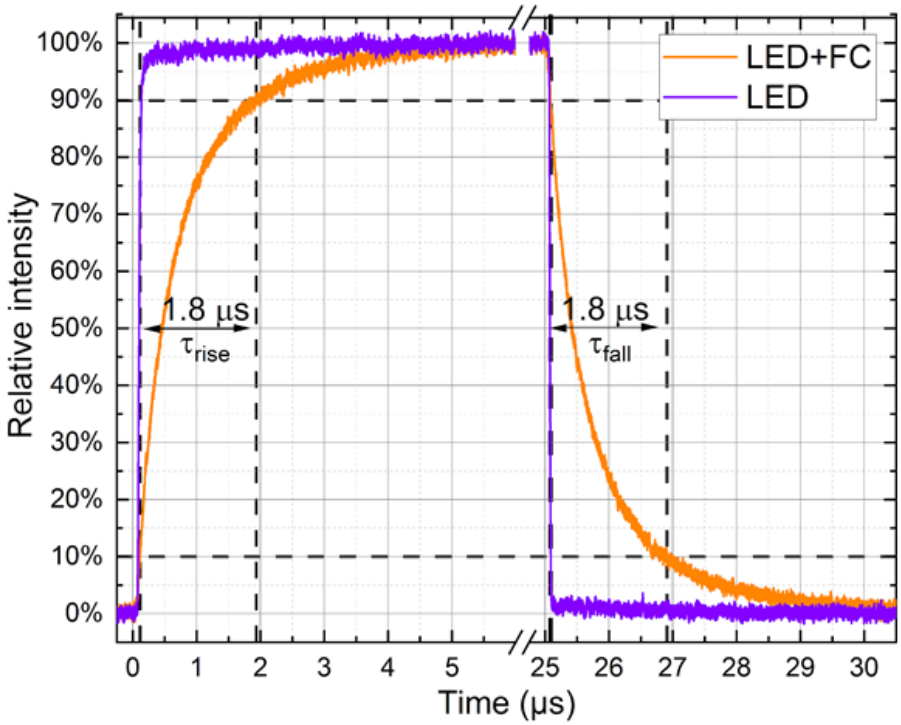

Figure 4.10: FC time response analysis: The LED is modulated with optical intensity between 0% and 100% of the nominal optical power with square wave 50 % of duty cycle. LED rise and fall times of few ns are much lower than FC rise and fall times (1.8 μs)

By considering the FC as a simple first-order RC electrical circuit [100], we can estimate an overall FC BW of approximately 200 kHz. This estimated value is slightly lower than the experimental BW extracted from the data presented in Figure 4.11. Where the amplitude of the received signal is plotted as a function of the LED driving frequency in the small-signal regime. The measurements were conducted for a distance of 2 cm between the LED and the PD. The slight deviation observed between the estimated FC BW based on the RC circuit model and the experimental data can be attributed to the convolution of multiple Q-Dots responses, each having different time constants (Figure 4.10).

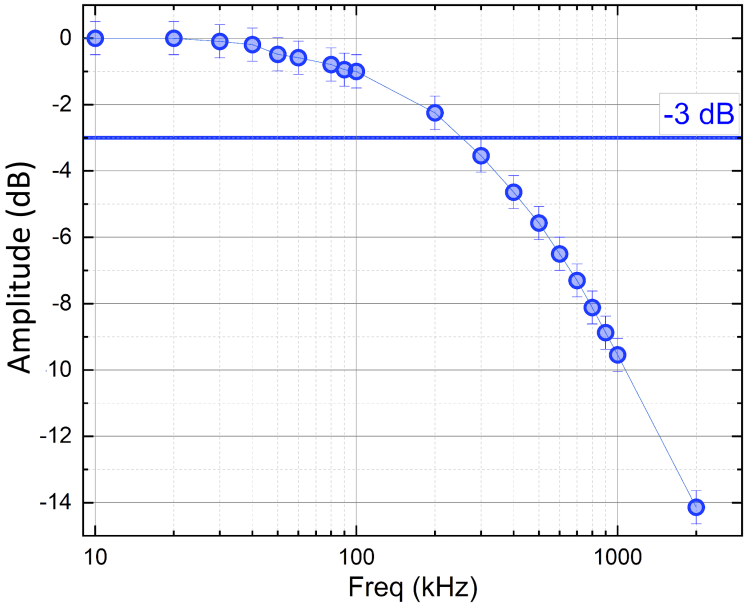

Figure 4.11: BW analysis: Relative amplitude measurements using a variable-frequency sine wave, in small-signal regime. The amplitude values are normalized to the maximum value, expressed in dB. Both step response and BW measurements are relative to side distance x = 2 cm.

Applying the Shannon-Hartley theorem [101], we can predict a maximum channel capacity (C) of approximately 1 Mbps for an SNR of around 11 dB, assuming additive white Gaussian noise (AWGN). In our VLC setup, the TIA gain can be increased up to 20 dB, corresponding to a -3 dB BW of 1 MHz, more significant than our FC substrate's intrinsic BW. This optimal TIA configuration for our RX stage allows for maximum SNR without additional BW limitations. With the setup mentioned above, we can achieve the requested

noise margin of 11 dB for a 1 Mbps capacity, even in outdoor, long-range conditions when utilizing suitable high-power LED sources.

4.3 Long-Distance VLC Data Transmission

The novel VLC system incorporates the Q-Dots-based FC antenna as a large-area RX stage, and its performance has been evaluated in an outdoor environment to showcase its capability for long-distance communication even under intense solar irradiance conditions. The experimental measurements were conducted in July 2021 outside the Physics and Astronomy department at the University of Florence.

4.3.1 VLC system architecture for long distance communication

Figure 4.12 illustrates a block diagram of our communication setup. The VLC system comprises a digital transmitter (TX) consisting of a high-power 405-nm LED source (Thorlabs, M405P1) with a dedicated collimation lens (Figure 2.4a). The LED source is connected to a specially designed current modulator controlled by a digital encoder (Figure 4.12), which is based on the Arduino DUE digital microcontroller board [102]. The LED source has an intensity modulation BW (-3 dB) of 2.5 MHz.

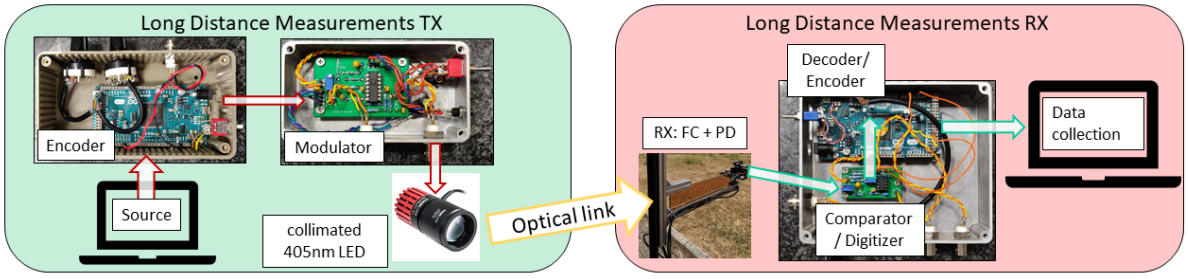

Figure 4.12: TX RX hardware overview: in the left block (TX) the signal is generated by a digital controller based on Arduino DUE, and it is encoded through current modulator converter. In the right block (RX) the receiver composed of FC and PD. The output signal is digitized and compared with a pre-stored reference message.

The TX stage generates a continuous stream of identical 32-bit packets encoded as in-

tensity modulation using the custom modulator stage. The current modulator enables the LED's optical intensity to be modulated in AC fashion, ranging from 0 % (Off) to 100 % (On) at a maximum current of 1.4 A. The average LED current is set to half the DC nominal value, which is 0.7 A when using a modulation with a 50 % duty cycle. The RX stage, depicted in Figure 4.13, consists of the FC antenna with the PD + TIA placed on its short side, as explained in Section 4.2.1. The TIA signal is digitized using a single-threshold Schmidt-trigger comparator stage and then decoded by a digital micro-controller board, also utilizing the Arduino DUE platform.

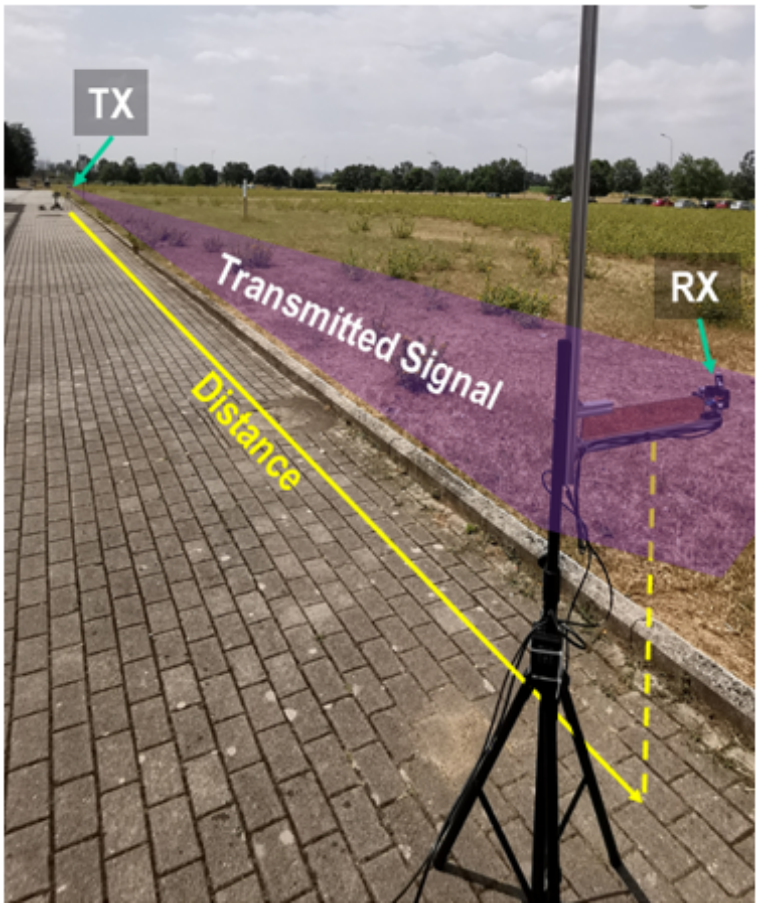

Figure 4.13: Experimental sketch of outdoor long-distance measurements setup

The captured data are processed in real-time by the digital board, which conducts a byte-wise comparison of each received packet with a reference packet and records any errors that occur in the received stream. The performance of the communication system is evalu-

ated using the Packet Error Rate (PER), which is defined as the ratio of received packets containing at least one incorrect bit to the total number of sent packets. Furthermore, the RX signal is acquired using a 200-MHz digital oscilloscope (Tektronix, MDO3024) and an FFT spectrum analyzer (SignalHound, USB-SA44B) to perform direct Signal-to-Noise Ratio (SNR) measurements and analyze the noise characteristics.

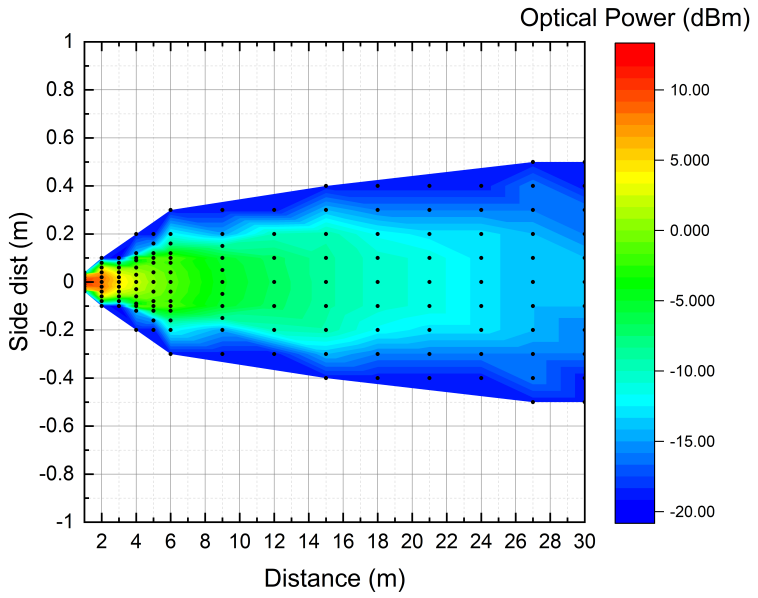

Figure 4.14: LED experimental irradiance map

4.3.2 Communication performance of Q-Dots FC antenna

During the experimental campaign, SNR and PER values were measured on the experimental grid for link distances of up to 100 m, as shown in Figure 4.13. The measurements were conducted using both modulation schemes. In the tests, the LED and FC were positioned 115 cm above the floor in a LoS configuration.

Based on the previous characterization of the FC with a low-power, high-BW LED, two basic configurations were tested for our experimental setup, operating at a clock rate of 500 kHz. The first configuration utilized 1 Mbps On-off Keying (OOK) Non-Return-to-Zero (NRZ), while the second configuration employed 500 kbps OOK with Manchester encoding. For the NRZ configuration, the optimal TIA gain setting was found to be G = 20 dB, while

for Manchester encoding, the gain was reduced to G = 10 dB to mitigate Inter Symbol Interference (ISI). The observed discrepancy is likely attributed to technical limitations of our RX board when the Manchester configuration is chosen, as the Arduino DUE board does not natively support Manchester encoding [39]. This limitation may result in reduced timing tolerance during the bit decoding process performed by the microcontroller board. Furthermore, this effect is amplified when dealing with BW-limited waveforms and low-frequency signal fluctuations. Consequently, the Manchester configuration requires a lower TIA gain setting, corresponding to a larger TIA BW value of approximately 1.5 MHz. The solid lines in Figure 4.15 correspond to a fit of the SNR data using a function of the form $I(D) \propto 20\log(A/D^2)$, where A is a free fit parameter.

SNR measurement

Assuming a digital, square waveform, we can define the SNR in decibels as $20\log(S_{RX}/2\sigma)$, where S_{RX} represents the signal amplitude and σ is the RMS value of the noise after the RX stage. For the G = 10 configuration (500 kbaud Manchester encoding), we observe $\sigma \approx 0.7$ mV, while for the G = 20 configuration (1 Mbaud), $\sigma \approx 0.8$ mV. Consequently, the SNR value at 500 kbaud (Manchester encoding) is lower compared to the 1 Mbaud case, as shown in Figure 4.15, which displays the measured SNR values as a function of distance D for both configurations. Circles represent the experimental data, while the error bars, primarily influenced by repeatability in the relative positioning between the TX and RX stages, are smaller than the symbols.

In the far-field region, where the beam spot size (Figure 4.4) significantly exceeds both w and h, we can consider the optical irradiance $I(D)$ to be uniformly distributed across the entire antenna surface. Consequently, the signal amplitude after the RX stage (proportional to the local irradiance) will decrease as $1/D^2$, where D represents the distance as a consequence of beam expansion, which is practically spherical in the far-field.

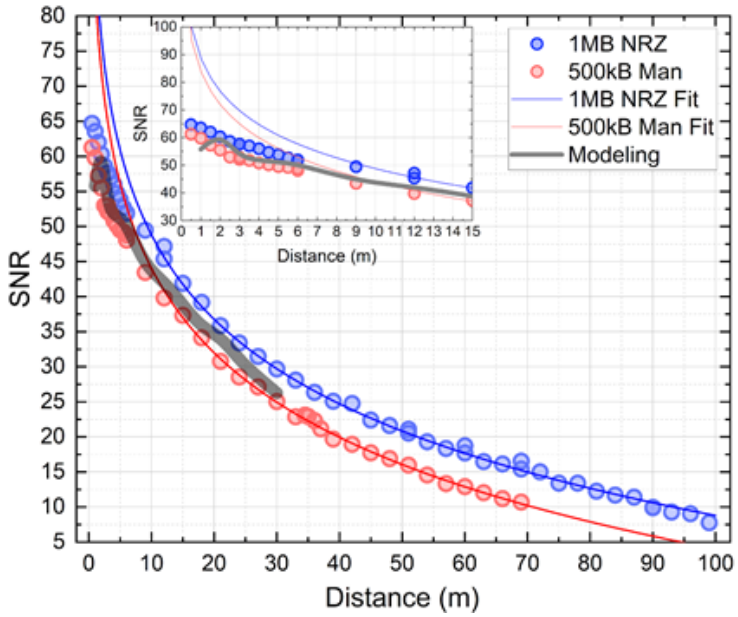

Figure 4.15: Measured SNR versus distance for 1 Mbaud NRZ (blue) and 500 kbaud Manchester (red). Solid lines refer to a fit to data in the far-field propagation region. The inset highlight short-distance deviations of data from the far-field trend. The gray thick shaded line represents the prediction of the efficiency/propagation model.

The SNR trend shown in the figure exhibits the expected behavior at large distances for both baud rates, following a decrease proportional to $1/D^2$. However, a significant deviation from this trend occurs at short distances ($D < 10$ m, inset of Figure 4.15), where the relationship between S_{RX} and D is not strictly proportional to $1/D^2$. When D is reduced further, the size of the beam spot becomes comparable to the surface area of the FC antenna, resulting in dependence of SNR on variations in D.

PER measurement results

The experimental campaign for PER measurements involved sending a total of 10^5 packets, ensuring that the minimum PER achievable is 10^{-5}. In Figure 4.16, the PER values are plotted as a function of D with 3 m intervals. The error bars indicate the uncertainty due to the relative positioning between the TX and RX, similar to the SNR measurements. The blue and red thick-shaded lines in the figure represent the expected error probability (PER) for the transmission, taking into account the relationship between SNR and the Q function

in the AWGN approximation [103], as well as the approximate relationship between SNR and distance $S_{RX} \propto 1/D^2$ established in the previous subsection.

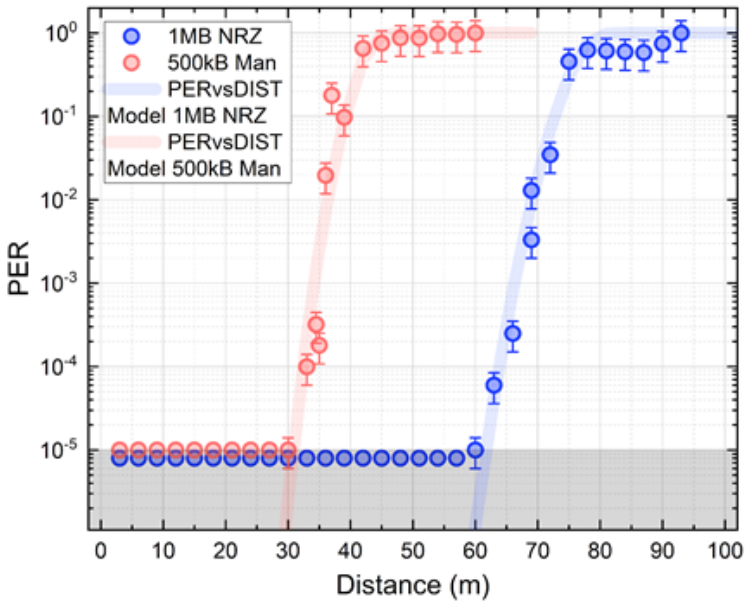

Figure 4.16: PER vs Distance for 1 Mbaud NRZ (blue) and 500 kbaud Manchester (red). The gray shaded area represent the error-free zone for our measurements that is PER $\leq 10^{-5}$. The blue and red thick shaded lines represent the expected PER on the transmission considering the relation between SNR and Q function

Our VLC system based on the FC antenna demonstrates error-free transmission capabilities for distances $D < 60$ m ($D < 30$ m) in the 1 Mbaud (500 kbaud Manchester) configuration. The lower SNR values discussed in the previous section contribute to the poorer performance of the Manchester configuration. For the 1 Mbaud configuration, the Shannon-Hartley limit (Section 4.10) predicts error-free transmission for SNR values above approximately 11 dB, which corresponds to $D \gtrsim 85$ m. The error-free region observed in the experimental results is slightly smaller but still in good agreement with the prediction. It is worth noting that the Shannon-Hartley theorem does not account for factors such as timing and synchronization errors inherent to our digital boards, further highlighting the satisfactory agreement.

Performance under different solar Irradiance conditions

PER measurements were conducted under different irradiance conditions to evaluate potential effects on the quality of VLC transmission. Figure 4.18 presents a comparison between the *Sun* condition (direct sunlight illumination on the RX stage, intensity greater than 70000 lux) and the *Shadow* condition (no direct illumination, intensity approximately 10000 lux) as shown in Figure 4.17.

In the *Sun* condition, the OA experienced an intensity exceeding 580 W/m^2. The experimental runs were performed on various days, with clear sky conditions, typically between 12 and 2 p.m., to maximize solar irradiance on the RX stage. The *Shadow* configuration was achieved by artificially shading the RX stage. The data presented in the figure are obtained as the average of five repeated measurements for four different PER levels. The error bars indicate the maximum deviation from the average.

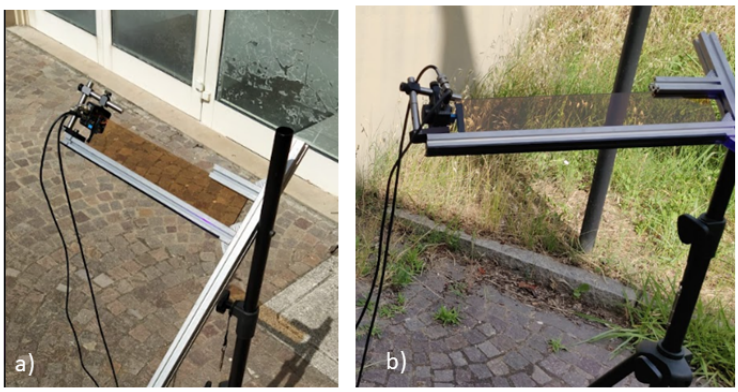

Figure 4.17: RX stage under different solar conditions. a) direct sunlight illumination on the RX stage. b) no direct sunlight illumination.

The results demonstrate that there are no significant variations in the performance of VLC between the two configurations. This confirms that the combination of electrical and chemical-physical properties of our FC-based RX stage effectively ensures reliable long-range VLC links even under strong solar irradiance. It is important to note that these results were achieved through a careful design of the PD+TIA front-end. Future studies will focus on the sun-induced wearing of FC substrates and the detailed characterization of additional

noise caused by direct irradiance on the PD.

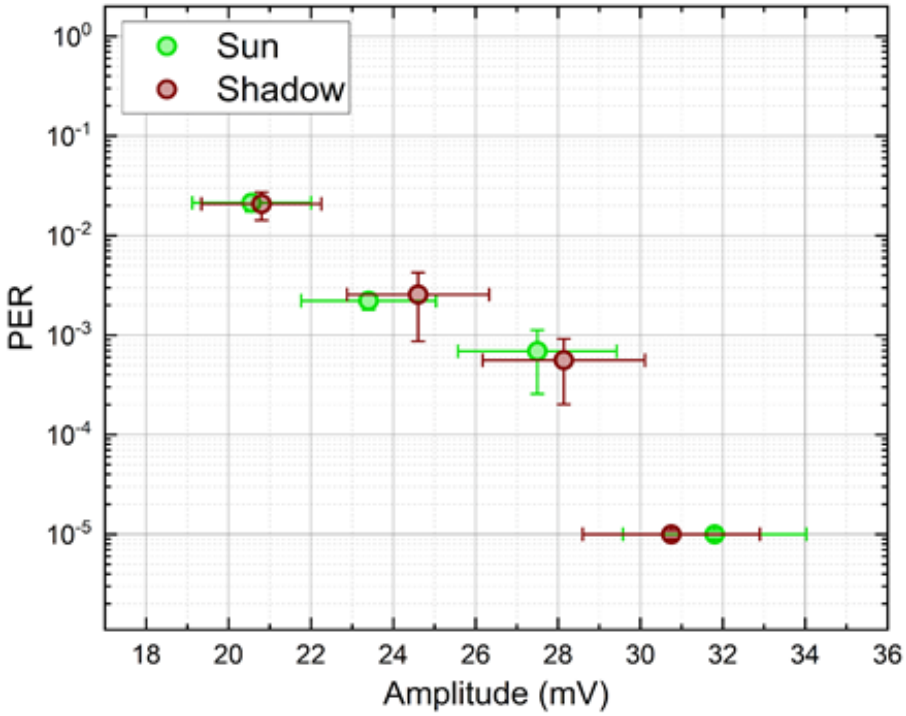

Figure 4.18: Comparison between direct sunlight illumination on *Sun* ($>$ 70000 lux) and no direct illumination *Shadow* ($\simeq$ 10000 lux)

4.4 Summary

In this thesis, a novel OWC system is described that makes use of a novel, large-area FC OA built on photostable $CuInS_2$ Q-Dot fluorophores, characterizing its performance at realistic outdoor distances of up to 100 m. Details on the implementation process for the large FC antenna, which measures 38.4 cm by 6.8 cm and is the largest FC antenna described for VLC/OWC applications are provided. Additionally, a detailed evaluation of its durability, temporal response, BW, FoV, and effectiveness, noting how these factors changed depending on where the light spot was on the slab are given.

When using a collimated light source, the measured BW at the -3 dB level for the FC slab exceeds 250 kHz, and the reported FoV exceeds 80 degrees full width at half maximum (FWHM). FC OA was combined with a unique RX stage which was customized to effectively

filter out ambient light. Even in the presence of extreme direct sun light surpassing 70,000 lux, real-time communication in outdoor settings was tested. The transmission-reception (TX-RX) distances up to 100 m were tested in this thesis. Remarkably, the greatest link distance recorded for a system using an FC OA to date was achieved for distances of up to 60 meters with error-free transmission at 1 Mbaud non-return-to-zero (NRZ). The characterization method and model presented here could be used in various long-range VLC systems that employ FC OAs.

The findings indicate that developing and utilizing large Q-Dot based FC antennas hold great promise for establishing long-distance optical communication links. Consequently, they emerge as strong candidates for a new generation of high-gain RXs for extensive FSO links and VLC. The advantages offered by these antennas, including their substantial gain, photo-stability, and reduced misalignment and pointing issues, hold critical significance. This research has the potential to significantly influence the advancement of innovative Internet of Things (IoT) devices that seamlessly integrate communication and solar energy harvesting functionalities. In the subsequent phase of my research, I will study the potential integration of solar cells along the edges of the FC antenna. This integration will enable the design and testing of hybrid devices capable of hybrid energy harvesting and VLC communication. One of the most important example of such hybrid devices is to characterize building integrated smart windows capable of VLC Communication and harvesting energy. Furthermore, future research activities will focus on exploring optimized, large-area geometries to enhance VLC performance in practical and real-world scenarios.

Chapter 5

Organic FC-Based White light VLC RX Stage

In the context of the background discussed in Chapter 3, in this chapter of the thesis, I will discuss in detail the novel optical antennas with two different organic fluorophores (OFs) and their possibility to be employed for a white LED VLC system. For this purpose, the two most efficient organic dyes that have recently been used for the application of LSCs are named Lumogen Red© 305 F (LR305) and DQ1. The purpose of this study is to compare and devise a very efficient VLC RX stage based on these fluorophores for WLED sources as a transmission stage. OFs offers numerous advantages over rare-earth elements [104, 105] or inorganic nanoparticles [88, 106, 107, 108, 109] in the realm of LSC and, more generally, in FCs. Notably, most OFs exhibit excellent solubility in the polymer matrices utilized for constructing the FC slab. This solubility is crucial to prevent the formation of aggregates that could quench fluorescence and induce scattering effects, ultimately diminishing light reflection within the slab. From a spectroscopic perspective, OFs display broad absorption bands with high molar extinction coefficients. In addition, the chromophore's structural changes can be customized to change the absorption wavelength. Despite this, it is challenging to accomplish high quantum yields ϕ, especially at high wavelengths, and OF also

experiences self-absorption issues as a result of small Stokes shifts [85].

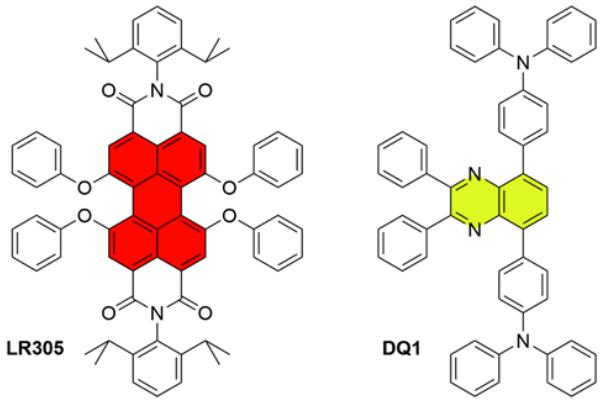

Figure 5.1: Chemical structure of LR305 and DQ1. The perylene and quinoxaline cores are highlighted in red and yellow respectively

However, choosing structures with the appropriate optical properties is possible because of an advantageous structural design. Self-absorption must be kept to a minimum in VLC applications because it can cause secondary re-absorption losses and temporal delays in the transmission of light at the RX, which could lower the maximum achievable BW for high bitrates when large substrates are used [79]. In this thesis, LR305, which is currently acknowledged as the top-performing OF in LSC applications [110], is chosen as a reference point. This choice was based on several factors: LR305 boasts an excellent match between its absorption band and the spectrum of white light-emitting diodes (WLED), making it a suitable candidate for this research (Figure 5.1). Additionally, LR305 is readily available in the market and is one of the most commonly used OFs.

Moreover, it's worth noting that the performance of large-area FCs constructed with LR305 is often constrained by self-absorption phenomena (Figure 5.2). This limitation arises because LR305, like many symmetric perylene fluorophores, possesses a limited Stokes shift and shows significant overlap between its absorption and emission spectra [111].

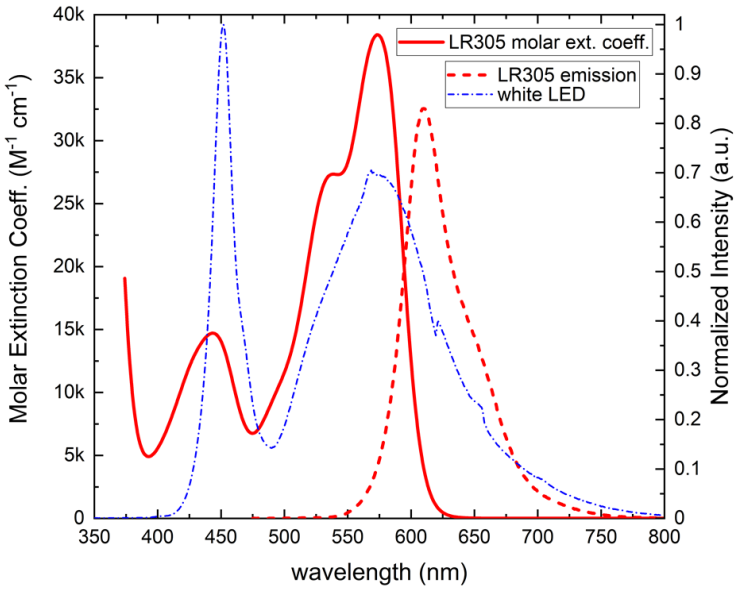

Figure 5.2: Absorption (solid line) and emission (dashed lines) spectra of the Lumogen in the realized PMMA slabs (conc. 350ppm); blue dashed line correspond to WLED emission spectrum

The second OF that was chosen is DQ1, which is a recently created chromophore with a quinoxaline core that has been effectively used as an LSC in solar applications [87]. With a notable ϕ value ranging from 0.90 to 0.98 depending on the fluorophore concentration in PMMA films, DQ1 has the benefit of achieving Stokes shifts as significant as 116 nm (0.61 eV) while maintaining simple and affordable synthetic pathways. It is difficult to predict which of the two fluorophores would perform better in WLC because DQ1 has a greater ϕ and less reabsorption, whereas LR305 overlaps well with the WLED spectra.

Figure 5.2, 5.3 reports the absorption and emission spectra of the FCs created with the two fluorophores. A large portion of the UV-visible spectrum is covered by the three primary absorption bands of LR305 (Figure 5.2), which have peaks at 443 nm, 536 nm, and 574 nm, respectively. Its fluorescence has a peak at 611 nm. Since the Stokes shift for LR305 is just 37 nm [6], the overlap between absorption and emission is relatively consistent. DQ1's absorption and emission spectra, which are respectively centered at 430 and 530 nm (Figure 5.3), are blue-shifted as compared to LR305.

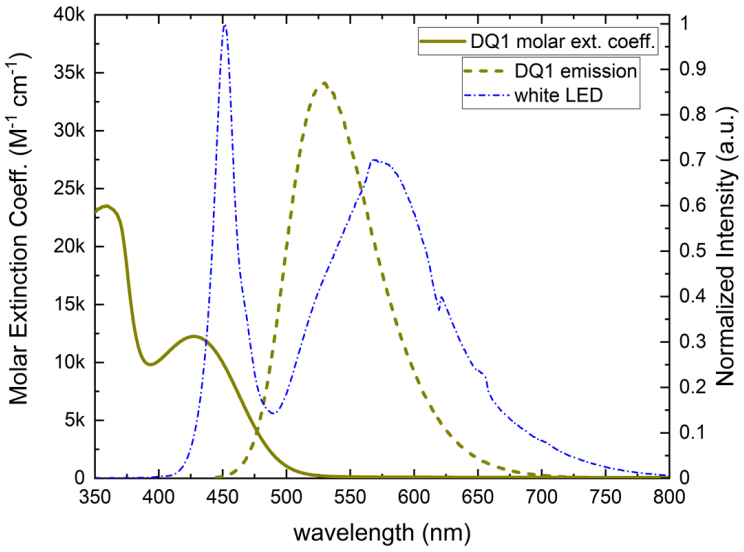

Figure 5.3: Absorption (solid line) and emission (dashed lines) spectra of DQ1 in the realized PMMA slabs (conc. 350ppm); blue dashed line correspond to WLED emission spectrum

In the given FC's both OFs show good ϕ values of 0.83 (LR305) and 0.87 (DQ1). The fluorescence lifetime of both fluorophores was previously characterized to be roughly 8 ns, making them suitable for VLC applications with BW up to several MHz. [87] [112].

5.1 Experimental Setup

5.1.1 Integration of FC antenna in VLC RX stage

Chromophores LR305 and DQ1 were dropped in methyl methacrylate slab with 350 ppm concentration after passing through a rigorous process of synthesis [113] which is not part of my PhD studies. The doped slabs were cut by LASER cutting to get a square geometry with a dimension of 50 mm $\times$ 50 mm $\times$ 3 mm dimensions (W$\times$H$\times$T), and it was polished on both front and back side surfaces both FCs used in this study are shown in Figure 5.4.

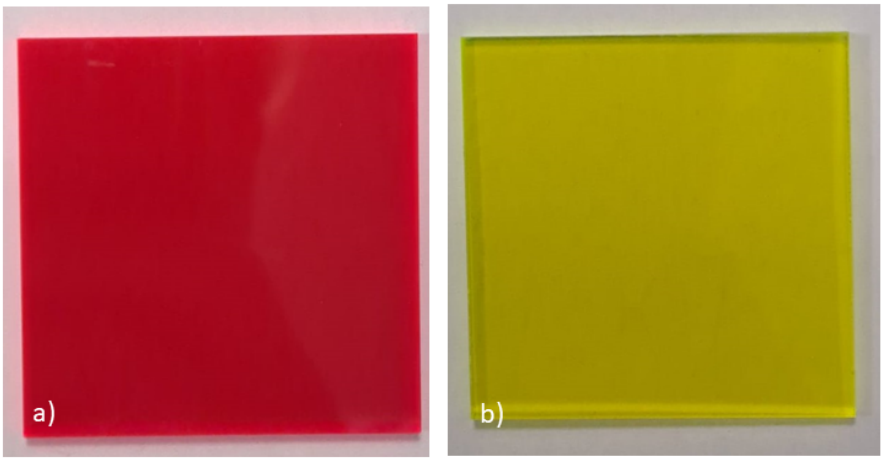

Figure 5.4: Fluorescent concentrators. a) FC Lumogen. b) FC DQ1

In order to fully characterize the working capability of the FC slab RX stage, the experimental campaign is divided into three steps:

- Time response and BW analysis of both FCs.
- Collection efficiency of both FCs.
- Communication performances of both FCs based VLC Rx stage.

5.1.2 FC Time Response

In this section, I will discuss the characterization carried out for the time response of FC's, as this parameter is critical to figure out how fast they can respond to the incoming signal. In order to measure the time response and BW of both FCs, OA is realized by coupling commercially available APD (Thorlabs APD 430 A/M) with a small active area of $0.2mm^2$ and a large BW of 400 MHz. .

Time response can also be translated to the BW, which is an essential parameter in designing a communication system. To carry out this analysis, an AWG (Sigilent SDG6022X) with a maximum BW of 500 MHz to drive a very low-power violet LED (Thorlabs LED405E) to create a high BW TX stage was used.

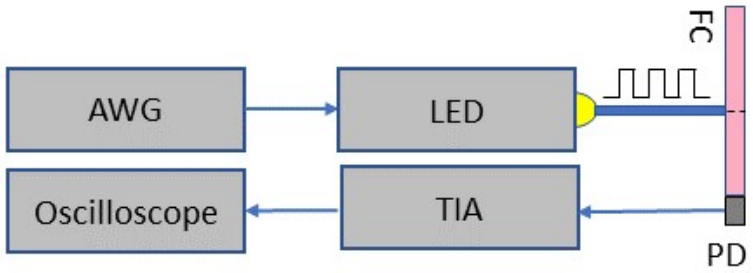

Figure 5.5: Block diagram of the experimental setup for time-response measurement.

As a first step, I measured the optical signal emitted by the LED through APD (Thorlabs APD 430 A/M) by applying a square pulse to the LED, keeping in view that the driving voltage levels should be in the optimal region. A block diagram of the experimental setup for time response analysis is shown in Figure 5.5.

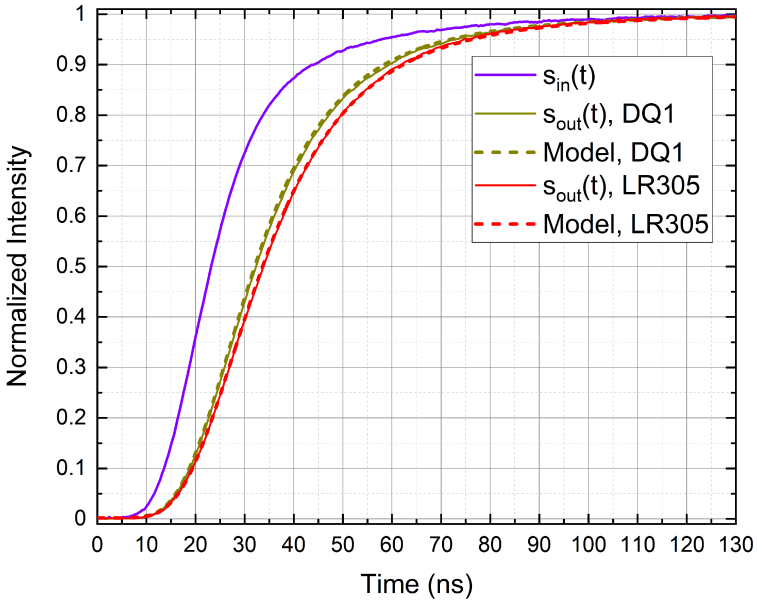

Figure 5.6: Rise time of LR305 and DQ1 FCs (green and red solid lines respectively) when stimulated by a BW-limited pulse of violet light (purple line). Dashed lines represent the function obtained applying the model (see text), minimizing the deviation from $s_{out}(t)$.

The rise and fall duration of the recorded optical signal from the violet LED is 30 ns, which in terms of BW is 12 MHz. As the second step to measure the time response of the FCs, the violet light source is then positioned at the center of the FC, as shown. APD was attached to one side of the FC to record the generated photons. The temporal response of

both FCs is shown by the solid lines in Figure 5.6. The FC time response is replicated as a first-order low-pass filter if the reabsorption of the photons inside the FC is negligible. In order to estimate its cutoff frequency we calculate the convolution of $s_{in}(t)$ with a decaying exponential and determine the time constant that minimizes the deviation of the convoluted function from $s_{out}(t)$. The comparison is shown in Figure 5.6. For the ideal set of time constant value $\tau_{\mathrm{LR305}} = (11.1 \pm 0.2)$ ns for LR305 slab and $\tau_{\mathrm{DQ}} = (9.52 \pm 0.12)$ ns for DQ1 are estimated from fit analysis details are discussed in [113]. The falling edge of the signal was subjected to a similar analysis, which produced comparable results within the experimental uncertainties. Although the measured time constants are slightly larger than those previously reported in the literature [87] [112] this discrepancy may arise from the multi-photon reabsorption which increases the time response of the antennas [79] .

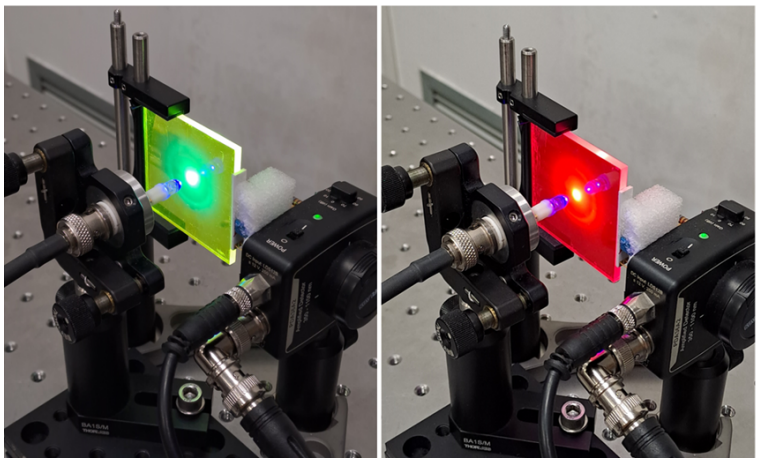

Figure 5.7: Image of the implemented OAs

5.1.3 Collection Efficiency

In order to calculate the collection efficiency (η_{coll}) which is a ratio between the photons collected at the edges of the FC to the photons impinging on the OA, LEDs of different wavelengths (385nm, 405nm, 430nm, 465nm, and 560nm) were used as an optical source. To carry out η_{coll} test the APD (Thorlabs APD 430 A/M) is replaced by the customized 30 mm $\times$ 3 mm Si PD (Hamamatsu S3588-09) discussed in Section 4.2.1, whose photo-

current is voltage-converted and amplified by a trans-impedance amplifier (TIA) with 12 MHz BW. A multi-order AC filtering stage is embedded before TIA to filter out low frequency unwanted light components below 1 kHz, to avoid DC saturation [114]. Moreover to characterization of η_{coll} of both FC with WLED is also very important, with and without optical filter. Each of the LED is driven at its nominal current values during this characterisation. The OS from each LED transferred by the OA is then collected by the custom made PD+TIA stage, which is then recorded by a 200 MHz digital oscilloscope (Tektronix MDO3024) which digitizes the output signal.

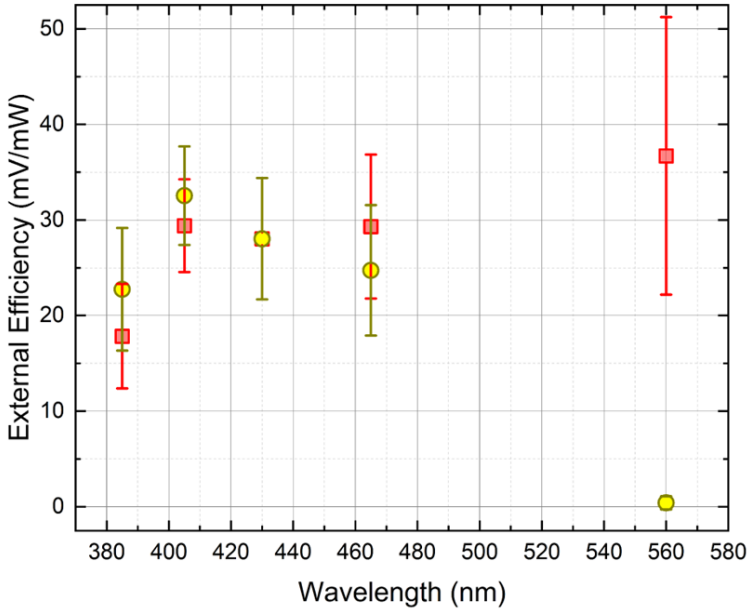

Figure 5.8: Symbols represent the power-normalized efficiency of LR305 and DQ1 OAs, measured with LEDs at different wavelength.

To present comparable efficiency results, the recorded amplitudes are normalized to the corresponding optical power of each LED and then reported in 5.8 as a function of LED wavelength. This is because the optical power of LEDs varies depending on their inherent characteristics. The experimental uncertainties on PD and LED location, LED power, and signal amplitude are propagated in error to produce the error bars.

The results demonstrate that OAs based on DQ1 and LR305 operate similarly in the UV-blue range, with DQ1 having a slightly higher η_{coll} at 380 and 405 nm than LR305.

The efficiency of DQ1 significantly decreases in comparison to LR305 at wavelengths greater than 430 nm, as predicted from absorption spectra, while LR305 boasts a significantly higher yield in the green-yellow region around 560 nm, a crucial band for WLED-based communications.

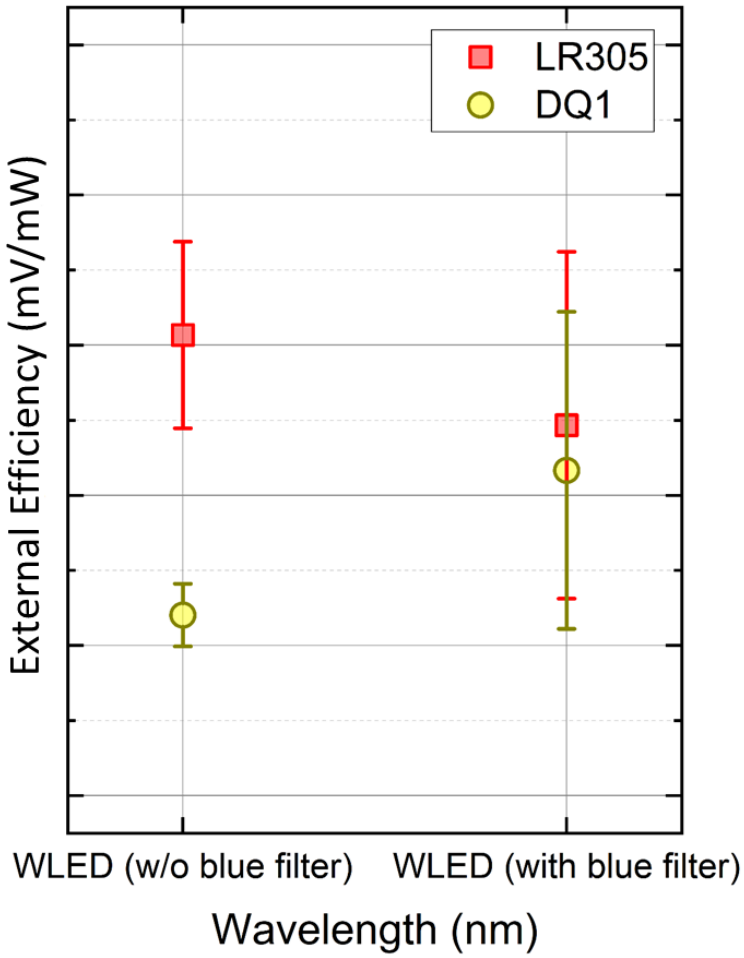

Figure 5.9: The power-normalized efficiency of white LED, with and w/o blue filter.

According to Figure 5.9 it can be seen that when white light is used LR305 demonstrates a higher external efficiency than DQ1, with approximately triple conversion efficiency. When blue filter is used as it filters out a large portion of white light spectrum it causes a drop in the overall efficiency of the fluorophores. However DQ1 has lesser reduction (62%) as compared to LR305 (relative to unfiltered condition 85%) because the absorption peak of DQ1 lies in the blue region approximately around 430 nm as shown in Figure 5.3. Both FCs

exhibit comparable capabilities under blue filtering light. This is due to the self-blue-filter property of the DQ1's absorption profile as mentioned earlier the absorption peak of the DQ1 lies in blue region so it inherently filters the yellow and green portion of white light spectrum, hence the performance of DQ1 is not so much effected when blue filtered light is used, which is not in the case of FC LR305.

5.2 Communication Performance of FC-based OA's as VLC Receivers

5.2.1 Communication system for VLC tests

To select the most suitable OA for WLC based on the two FCs, they were embedded in a complete VLC system to fully characterize the performance of OAs as optical receivers, as shown in Figure 5.10. Moreover the hardware diagram of the experimental setup used in the experiment is shown in Figure 5.11. It is essential to perform data transmission experiments individually on each of them to compare their performance. For this purpose, a synchronous digital transmission analyzer (Anritsu ME520B BERT system) with an external distributed clock to both TX and RX was used to drive WLED to perform a bit error rate test. Pseudo-random binary sequence (PRBS) data was generated using Anritsu digital transmitter with a non-return-to-zero, on-off keying (OOK-NRZ) modulation scheme. The Anritsu TX module (Figure 5.11a) drives WLED (Thorlabs LEDW7E) that serves as the VLC TX stage, sending digital PRBS sequence as intensity modulation on the optical channel.

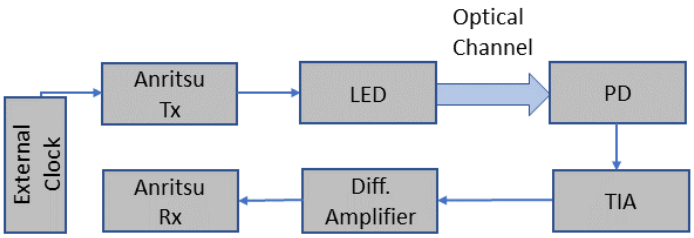

Figure 5.10: Block diagram of the experimental setup for WLC communication tests and BER analysis

Two distinct configurations for the VLC RX stage were analyzed: the first [*White*] corresponds to a scenario in which the entire white WLED spectrum impinges on the OAs, and the second [*Filtered*] embeds the 450 nm optical filter in front of the WLED. Moreover, for reference, the [*bare PD*] arrangements, in which the PD serves as the direct RX front-end, are also examined.

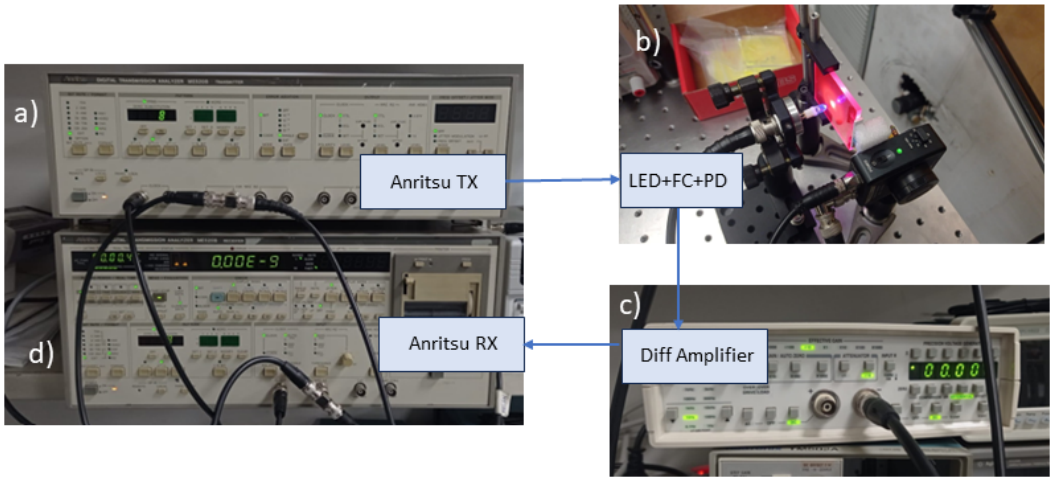

Figure 5.11: Hardware diagram used for experimental setup for WLC communication tests and BER analysis.

In order to measure data integrity and provide the BER value, the PD output following OAs is bandpass-filtered using a unitary gain amplifier (LeCroy, DA1822A shown in Figure 5.11c) and then delivered to the anritsu RX block (Figure 5.11d) of the BERT system. In order to test the communication performance of VLC system with OA's under consideration, transmission experiments for bit rates of 1 Mbps and 5 Mbps were performed. At 1 Mbps all

the VLC system configuration were inside the BW limits hence communication performance was not effected. On the other hand at 5 Mbps some of the VLC system configuration were cutted in BW, the limitations in the system are discussed below in detail .

5.2.2 BER vs Amplitude/SNR

This section illustrates the BER values measured for the discussed experimental configurations in Section 5.2.1 for two date rate cases, 5 Mbps and 1 Mbps. First, I will discuss the case for a data rate of 5 Mbps. The data is presented in Figure 5.12 as a function of the peak-to-peak amplitude of the signal received at the output of PD. Red, yellow, and blue symbols represent data for LR305, DQ1, and [*bare PD*] case, respectively.

Examining the 5 Mbps rate, the [*bare PD, White*], and [*LR305, White*] cases exhibit comparable BER values, which are higher as compared to all other cases. Notably, the BER values of these cases are notably higher than that of the LR305 Filtered case.

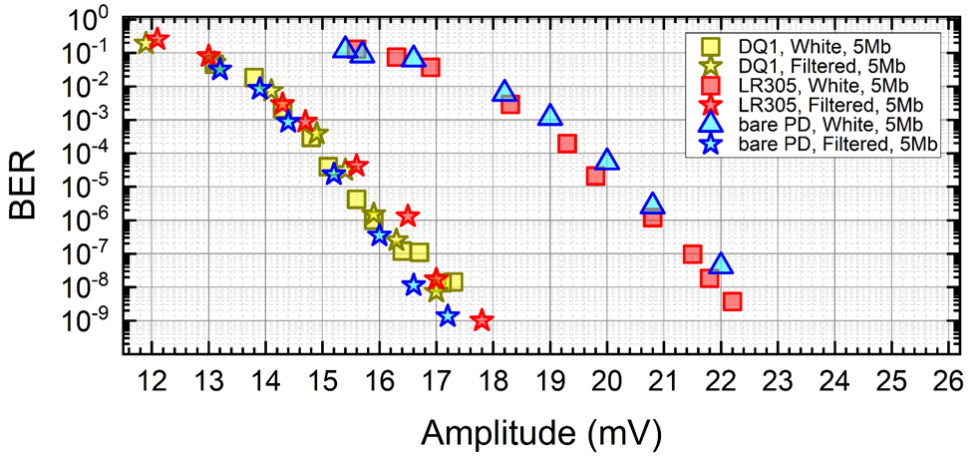

Figure 5.12: Communication performance for both OAs, using WLED with and w/o blue filter as source 5 Mbps.

This is due to the fact that at this particular data rate (5 Mbps), the BW limitation due to slow phosphor component of the WLED starts to become evident. Consequently, the overall SNR is lower for a given signal peak-to-peak amplitude. However, when utilizing blue-filtered light or the DQ1 fluorophore, the slow portion is not converted, as it is filtered

either by the blue filter or by DQ1; this results in a overall higher SNR correspondingly reducing BER value. This becomes more apparent when examining eye diagrams recorded for each experimental configuration at a fixed amplitude of 15 mV using a digital oscilloscope (Keysight, InfiniiVision DSOX6004A) operating at 5 Mbps. The results are depicted in Figure 5.13.

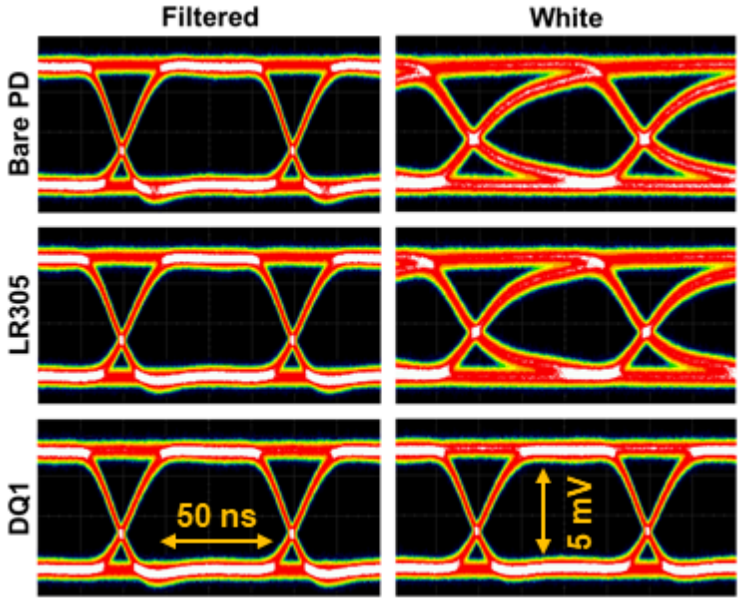

Figure 5.13: Communication performance for both OAs, using WLED with and w/o blue filter as source: eye diagrams for all RX configurations at 5 Mbps, for fixed signal amplitude.

In Figure 5.13 the bandwidth-limiting impact of yellow phosphors is observable in both the [*bare PD, White*], and [*LR305, White*] cases, resulting in slower transitions and narrower eye widths. Intriguingly, this effect is not visible in the Filtered cases, nor in the DQ1 White case, where the bandwidth corresponds to the intrinsic bandwidth of the blue component of the WLED at $\sim$ 9.4 MHz.

At the lower data rate of 1 Mbps, there are no substantial variations in performance observed. This suggests that both LR305 and DQ1 exhibit similar behavior in WLC links, attributed to their intrinsic lifetimes which is explained in Section 5.1.2, which are lower than the rise time of the WLED (approximately $\sim 160, \text{ns}$, with a BW of $\sim$ 2.2 MHz)

Figures 5.12 and 5.14 show that cases with similar peak-to-peak amplitudes, but with

different signal distortions due to factors such as varying bandwidths, may result in different BER values. This discrepancy is a consequence of distinct SNR values, defined as $\mathrm{SNR} = \mathrm{S_{RMS}}/\sigma_{\mathrm{noise}}$, where $\mathrm{S_{RMS}}$ represents the RMS signal amplitude after PD, and σ_{noise} denotes the measured RMS noise value in the decoder bandwidth. However, under the assumptions of purely additive white Gaussian noise, binary OOK modulation, and the absence of synchronization errors, the BER should only rely on SNR through the relationship $\mathrm{BER} = \frac{1}{2}\mathrm{erfc}(\mathrm{SNR})$ [115].

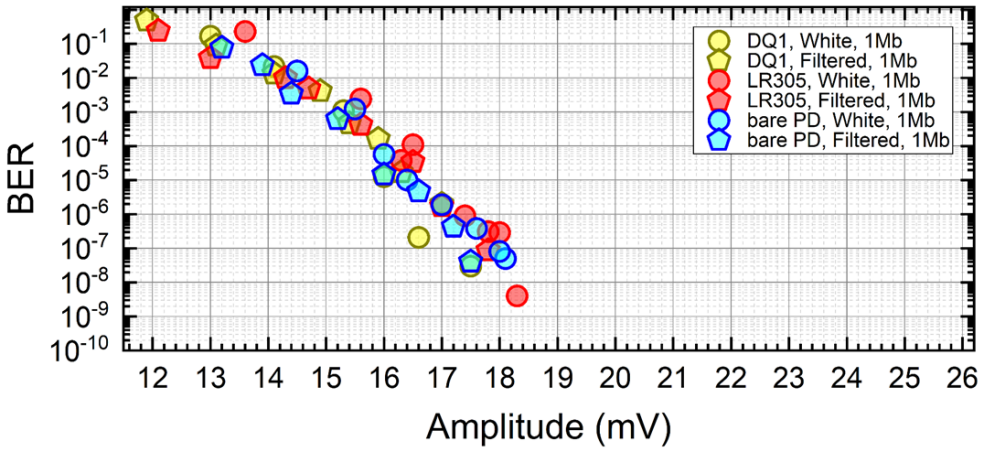

Figure 5.14: Communication performance for both OAs, using WLED with and w/o blue filter as source 1 Mbps.

By computing $\mathrm{S_{RMS}}$ and σ_{noise}, with $\sigma_{\mathrm{noise}} = \sim 0.669$ mV, BER data as a function of SNR (refer to Figure 5.15) can be represented. The calculation involves the recorded tracks of amplitude values measured before the input stage of the RX module. Oscilloscope tracks are BW-limited to 200 MHz, which approximately matches the input BW of the RX module. This ensures that $\mathrm{S_{RMS}}$ and σ_{noise} are effectively calculated within the decoder BW.

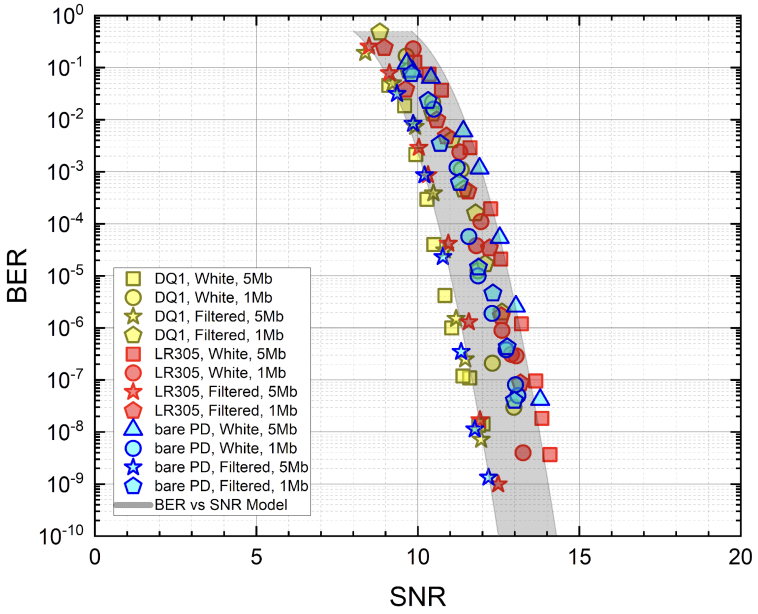

Figure 5.15: recorded BER vs recorded SNR (symbols) and model predictions (shaded area). The extension corresponds to the confidence interval of the model.

The Figure 5.15 illustrates the comparison between data and the model predictions (shaded area) with no free parameters, considering a technical offset $S_{offs} = 6.5, mV$ affecting the discriminator module. This offset lowers the effective SNR by a factor of $S_{offs}/\sigma_{noise} \simeq 9$. The BER model is computed using the rescaled value $(SNR - 9)$. The width of the area in Figure 5.15 corresponds to a confidence interval obtained by incorporating a 5% error in the experimental value of the offset.

5.2.3 Communication tests as a function of distance

Finally, I examined the WLC performances of our OAs concerning the distance between the TX and RX. The WLED was driven with a constant nominal DC current and fixed modulation depth (modulation depth set at 150%). Both the signal amplitude and BER were recorded in 5-cm increments as the distance between the light source and OAs varied as shown in Figures 5.16 and 5.17, respectively, this analysis encompassed all configurations discussed in previous sections.

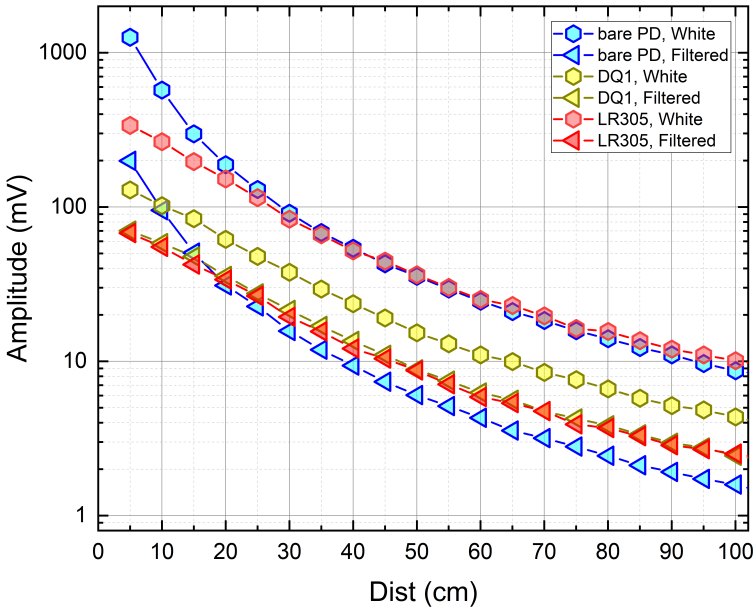

Figure 5.16: Signal amplitude recorded as a function of distance between WLED and OAs. Two configurations are presented for the optical source ([*White*] and [*Filtered*], respectively). In addition to each OA configuration ([*DQ1*] and [*LR305*]) also [*bare PD*] configuration is analysed

Focusing initially on amplitude measurements (Figure 5.16), our results reveal that in cases marked as [*White*] (hexagons), LR305 consistently outperforms DQ1 across all distances. Moreover, beyond a distance of approximately ~ 35 cm, using the LR305 OA yields larger signals compared to the [*bare PD*] scenario. This observation implies that the net OG of the LR305 OA is greater than that of the bare PD, suggesting a distinct advantage in incorporating LR305-based OAs in WLC systems. It is noteworthy that this may not be the case for the DQ1 OA, as it produces lower signals for all considered distances when white light is employed. Additionally, it's important to mention that the net OG could potentially be further increased by covering all thin edges with PD elements or creating larger FCs depending on the minimum BW required and the strength of re-absorption effects. Another strategy could involve coupling the PD with an index-matching material, although this was not implemented in the setup. In all cases marked as [*Filtered*] (triangles), there are consistently lower signal strengths compared to the [*White*] cases. In this scenario, both OAs clearly outperform the [*bare PD, Filtered*] configuration, particularly beyond ~ 20 cm, with

DQ1 exhibiting higher efficiencies than LR305 across the entire range. Consequently, this analysis suggests that DQ1 OAs are most effective in more specific blue/UV VLC applications.

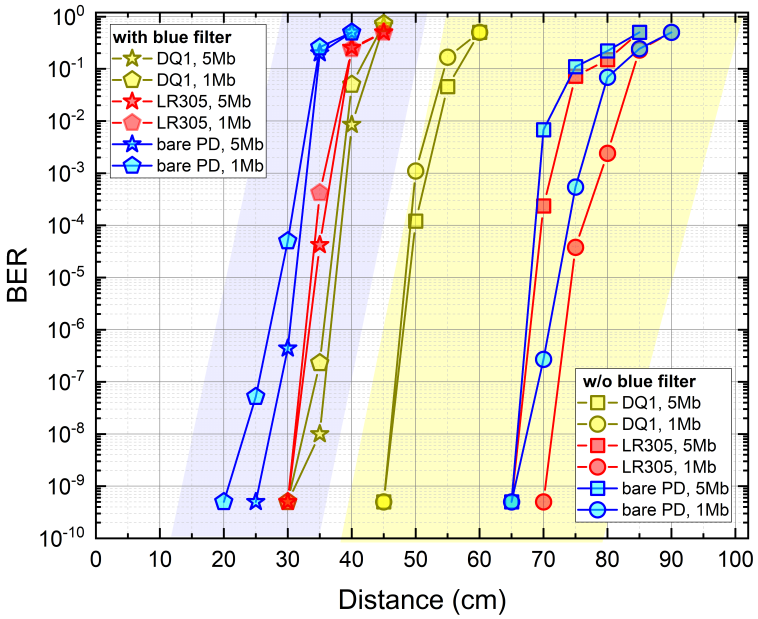

Figure 5.17: BER vs Distance between light source and OAs. The cluster of experimental data inside the blue area refers to [*Filtered*] configuration, whereas the yellow shaded area refers to [*White*] configuration, for both 1 Mbps and 5 Mbps rates.

To corroborate the insights gained from pristine efficiency measurements, Figure 5.17 displays the BER values measured as a function of distance for all examined configurations at both 1 Mbps and 5 Mbps rates (see the legend for symbol assignments). Two clusters of data are emphasized by blue and yellow shaded areas, corresponding to [*Filtered*] and [*White*] scenarios, respectively. In experimental conditions under analysis, data with BER $< 10^{-10}$ are considered "error-free" and are not depicted in the graph. In the case of the [*Filtered*] scenario, where no BW limitations are expected due to yellow LED phosphors' lifetime (see Section 4.2.5), communication performances are generally enhanced by incorporating OAs in the RX stage for both baud rates. More considerable communication distances are achieved compared to the [*bare PD*] cases (depicted by blue/cyan symbols). This confirms that both OA-based VLC systems benefit from the increased OG, with a slight out performance of

DQ1 (yellow symbols) over LR305 (red symbols).

The [*White*] cluster data demonstrates that exploiting the whole white LED spectrum yields globally better performances in VLC applications up to 5 Mbps concerning the blue-filtered option for a given WLED source when no equalization techniques are involved [116], and larger system distances can be attained. Moreover, it is evident that at such baudrates the front end for WLC applications is the LR305-based OA. At 1 Mbps, this device attains error-free distances of 0.70 m, outperforming both [*bare PD*] and the [*DQ1*] configuration, the latter featuring error-free distances of 0.45 m due to reduced conversion efficiency on yellow wavelength components. Noticeably, this analysis highlights equivalent or slightly superior LR305 OA performances as compared to [*bare PD*] setting for both 1 Mbps and 5 Mbps rates. However, at 5 Mbps, it can be noticed that LR305 OA features slightly reduced link lengths as compared to the 1 Mbps case. As LR305 retains the WLED BW limitations, a reduced SNR and larger BW-induced inter-symbol interference (ISI) are affecting the performance of the system, however, pre-equalization techniques could minimize these issues.. This effect is not visible in the case of DQ1 (yellow symbols) due to inherent self-blue-filtering effects of this OF.

Summarizing the analysis, the data presented indicates that in full white light applications, the LR305 OA outperforms the DQ1 OA, serving as a viable alternative to bare PD front-ends. It's worth noting that the potential advantages of LR305 could be further leveraged by realizing larger OAs in future works. Conversely, the self-blue filtering feature in the DQ1 antenna eliminates BW limiting effects related to WLED sources, even for higher data rates (5 Mbps), at the expense of its overall efficiency for WLC applications. This makes the DQ1 antenna particularly promising for high-BW blue/UV light VLC applications. It's important to emphasize that the observed data rate is not inherently limited by the intrinsic properties of the OAs. They are expected to support larger baud rates when fast TX optical sources are employed, or when pre/post equalization processes are implemented.

5.3 Summary

In this work, two distinct OAs based on FC were created and characterized for use in white light VLC. These OAs are based on DQ1 and LR305, two of the most effective fluorophores that were initially created for the conversion of solar energy. I described inherent efficiencies of these OA's, such as conversion efficiency for a variety of LED sources with variable wavelength and time responsiveness to external light stimuli, as well as their capabilities when used as an optical front end in a WLC communication system. Both OAs are appropriate for high data rate applications due to their quick response times of the order of 10 ns, which are equivalent to the intrinsic lifetimes of the two OF. A thorough experimental investigation of conversion efficiency is also carried out. This analysis has universal applicability and may be useful in the development of OAs in the future for VLC and LSC applications. These OAs were tested in a complete WLC system, evaluating SNR and BER for data rates up to 5 Mbps OOK with Manchester encoding as a function of the distance between the TX and RX. This research which is carried out under both white and blue light filters, demonstrate that LR305-based OAs provide a significant advancement over traditional PD-based RX stages in WLC applications with few-MHz-BW requirements, such as many IoT applications. It is demonstrated that LR305 performs similarly or better than a typical RX stage using a bare PD. This is because a larger effective OG grants higher performances in terms of communication quality and WLC connection length.

In contrast, DQ1 OAs are the optimum choice when blue/UV sources may be used because of their greater Stokes shift, decreased self-reabsorption, and improved efficiency in the blue/UV region, which suggests that larger OAs could be obtained than with LR305. To create large-BW WLC links and preventing the yellow components typical of WLED spectrum, the self-blue filtering property of DQ1 could be used, although at the cost of a lower overall white light conversion efficiency. This research offers a significant step towards the full-scale implementation of VLC using white light, where effective, large-area, quick detectors with minimal angular dependence are essential components to exploiting common

white LEDs as VLC transmitters. Furthermore, because the presented OAs are built on effective LSC fluorophores that effectively convert white light, we anticipate that our findings will serve as a benchmark for future research aimed at creating a new class of hybrid devices for cooperative OWC communication and solar energy harvesting. These devices could be effectively incorporated in smart buildings for the deployment of pervasive, energy-efficient networks.

Chapter 6

Software Defined Radio (SDR) based Digital Signal Processing (DSP) stage for VLC

In this chapter of the thesis I will explain the role of a DSP stage, based on SDR developed in my PhD thesis work, in removing noise from the received OS. Furthermore, I will discuss in detail the architecture of the SDR-based DSP filtering stage and experimental campaigns carried out to validate the performance of the VLC system with and without implementation of the designed filtering stage.

6.1 Introduction

Implementation of VLC systems in realistic conditions can be heavily influenced by the environmentally induced noise. For example, background noise photons from artificial illumination and solar irradiance can be a strong detrimental factor of the communication performance for a VLC system. Therefore, it is essential to filter out excess noise to recover a sufficient SNR. For this purpose a dedicated filtering stage at the RX is desirable to maintain the performance of communication system.

As discussed earlier in Chapter 3 usually, a very common approach is to employ a bandpass optical filter on the top of the PD [117, 118]. This technique only allows certain wavelength to pass through and filtering out unwanted wavelengths. WLEDs are built in such a way that there is a yellow phosphorous coating on blue LED which converts blue light into yellow light, the mixture of both produces white light [119]. When WLED is used in VLC system bandpass optical filters are also used to filter out slow yellow spectral component of WLED [120], allowing only to pass blue component increasing the BW of the system [44]. However, in this approach the optical power from the LED source, which can be essential for creating long-distance links under conditions when large BWs are not necessary as in many IoT applications, is not fully utilized. In this light a viable architecture is proposed to use an appropriate electronic filtering stage, especially when white LED light sources are used [121]. The researchers have implemented analog filter techniques to eliminate undesirable voltage levels at the RX side. These techniques are applied after the TIA stage of the PD, to ensure the output SNR remains within acceptable limits, the simulated front-end incorporates an automatic gain control (AGC). More recently, advanced filtering schemes such as matched filter systems [122] or bandpass filtering [29], relying on active and/or digital front-ends, have been reported as more sophisticated methods for achieving effective filtering to attenuate artificial light sources by up to 30 dB. Additionally, this approach rejects low-frequency noise caused by sunlight. The papers [123, 124] discuss the use of AGC in conjunction with software-based adaptive filtering stages, the authors propose an open-loop signal processing approach where the RX adjusts its structural design to maintain optimal performance by analyzing the real-time SNR. However, it's important to note that these methods have not been implemented in actual systems. Instead, the performance of the RX is only evaluated through simulations. The proposed techniques and their effectiveness are assessed in a simulated environment, but their practical implementation and real-world performance have yet to be realized. The authors in [117] presented an analytical and simulated model of a Multiple-Input Single-Output (MISO)-based VLC system. They

demonstrated that the system's performance significantly improves even in the presence of optical interference caused by the environment. The system achieves a forward error correction (FEC) limit, indicating its ability to mitigate errors and enhance reliability. In this scenario, SDRs have gained considerable attention in academia and industry [125, 6] due to their adaptable combination of hardware and software modules. SDRs already served [126, 127] as excellent tools for designing and testing complex RF communication systems. In recent years, the VLC community has started leveraging the capabilities of SDR technology in various applications, including indoor, outdoor, and vehicle scenarios [128, 129]. However, the comparison of SDR front-end improvements with existing VLC systems has not been explored in these studies. This comparison is particularly crucial in realistic scenarios that involve factors such as background noise and strong solar irradiance. Evaluating the potential enhancements offered by an SDR front-end in such conditions is an important target for future research.

6.2 Software Defined Radio

In this section I will give an overview of SDRs their hardware and software. SDRs represent communication systems in which traditional hardware elements such as mixers, amplifiers, and modulators are replaced and programmed using a software. The Universal Software Radio Peripheral (USRP)-N210, an SDR produced by Ettus Research, is depicted in Figure 6.1a. Additionally, these SDRs are equipped with diverse daughter boards that are used as a front end tailored to the specific application and requirements of the communication system under design. In Figure 6.1b,c, daughterboards LRTX and LFRX, featuring a BW of 0-30 MHz, are illustrated and were utilized in this thesis. Furthermore, SDRs incorporate analog-to-digital converters (ADC) responsible for converting analog signals into digital format and vice versa. The central unit of an SDR is a field-programmable gate array (FPGA) which performs real-time signal processing tasks. Programming of SDRs is achieved through

software tools such as GNU Radio Companion (GRC), MATLAB, or Labview.

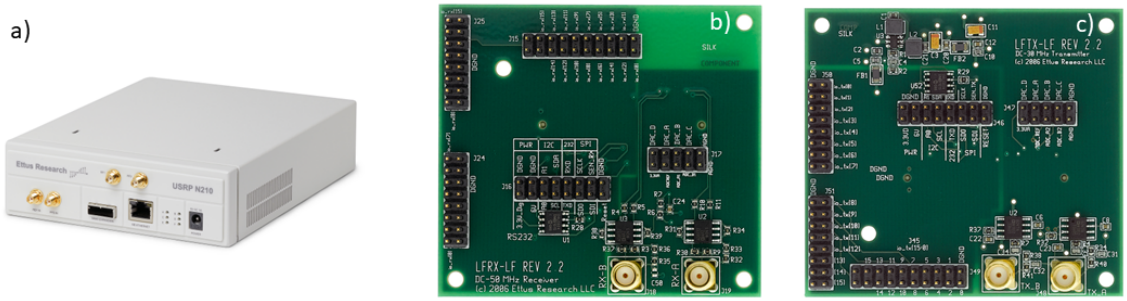

Figure 6.1: Basic hardware blocks of SDR. a) SDR USRP N210. b) Daughter board LFRX for transmission frontend. c) Daughterboard LFTX used for receiver frontend.

Different libraries of these software's are exploited by SDRs to execute distinct signal processing functions such as modulation, demodulation, encoding, and decoding, each handled by the aforementioned software. The features discussed above endows SDRs with increased flexibility and adaptability to a range of communication standards, eliminating the need for extensive hardware modifications.

6.3 Experimental Setup

In this section, I will discuss the experimental setup and RX configurations to design and validate the SDR-based DSP filtering stage for the VLC system. The DSP filtering stage is based on the open-source GNU radio platform [130] discussed in Section 6.3.1. Furthermore, USRP N210 [131] with daughterboards LFRX and LFTX [132] for the transmission and reception of the signal was used. Moreover, SDR is integrated between the TIA stage of PD and the comparator stage of RX [133]. The VLC TX comprises three main components as shown in Figure 6.4 an encoder, a current driver, and a white LED light source described in Section 2.1. The encoder is responsible for encoding 10^5 data packets as explained in Section 2.1 utilizing OOK modulation at a baud rate of 1 Mbaud. The Manchester line coding scheme encodes the data. The encoded data is then fed into the current driver, which regulates the intensity of the white LED light source based on the supplied current.

This allows for the transmission of the encoded data through the modulation of the LED light output. This modulation allows for the transmission of the generated data packets using the low-power automotive white LED source. On the RX side, two different PDs Thorlabs PDA100A2 and APD430A/M, are employed respectively as described in Section 2.1. To enhance the OG and reduce the FoV, an aspheric condenser lens ACL 25416U with a focal length of 16 mm is mounted in the front of the PDs. The light source (TX) and the detector (RX) are positioned at a height of 1.1 meters above the ground level. They are placed at the same height to maintain a direct LoS between the TX and RX. The core of the RX in this setup is based on an Arduino DUE microcontroller [102]. The received signal from the TIA stage of the photodetector is directed to the input of the digitization stage of the RX. At this stage, the analog signal is converted into digital form using a Schmitt trigger physical comparator. The digitized signal is then sent to the Arduino Due RX stage, which is analyzed in real-time. The RX stage detects the PER by counting the number of correctly received packets out of the total number of packets sent, which typically ranges from 10^5 to 10^6. The threshold for error-free communication is set at PER $\leq 10^{-5}$, meaning that if the number of correctly received packets falls below this threshold, the communication is considered to have no errors. In this configuration, a packet is considered lost if one or more bits are changed or lost compared to the original data bit stream. The length of each packet is 32 bits, resulting in an error-free threshold of 3.1×10^{-7}, indicating the desired level of accuracy for successful communication.

6.3.1 SDR-based filter stage GRC flow graph

In this section GRC-based flow graph developed for filtering noise, its building blocks, and their working principle is explained. In the first step of the research, a DC-block stage was designed and implemented to block the DC and low-frequency components of the incoming signal. The first block shown in Figure 6.2, UHD (Universal Hardware Driver) USRP source block in GRC, is used to interface the USRP devices; mainly, it acquires the data from USRP

hardware and passes it to GRC allowing it to analyze the signal. The primary purpose of UHD USRP source is data acquisition from USRP it also allows to set sample rate at which USRP processes the signal. The second block in the flow graph shown in Figure 6.2 is Complex to Float. This is used to convert complex value numbers to their respective float representation.

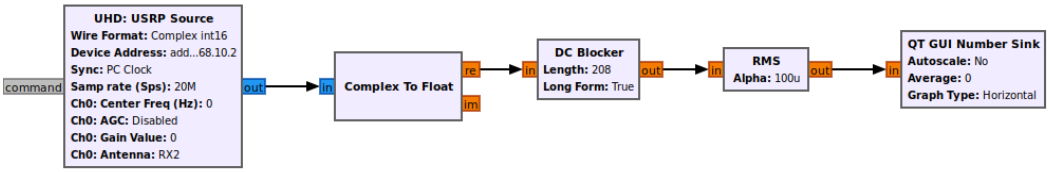

Figure 6.2: GNU radio flow graph for characterizing the effect of DC blocker on input BW.

The third block is the DC Blocker, which is used to remove the DC offset from the received signal. Moreover, following the DC Blocker is the root-mean-square (RMS) block, which computed the root mean square value of the signal, and RMS is the average value of the amplitude of the whole signal. The last stage in the flowgraph is QT GUI Number Sink: it is used to display numerical values in the graphical user interface (GUI). The DC blocker stage is critical for removing the interference caused by sunlight and other artificial stray light components. The DC-block stage uses a linear phase DC-blocker algorithm, which involves taking the moving average of the input signal and subtracting it from the original signal. The length of the delay line element in the algorithm is chosen to match the group delay experienced by different frequencies of the signal. Compared to an equivalent finite impulse response (FIR) filter, the DC-blocker algorithm provides a steeper low-pass filter with a smaller group delay and is computationally more efficient [134]. To determine the best configuration of the DC-block stage for different baudrates, an experimental characterization of the input BW was performed. The effect of this DC-blocker stage on input BW is described in Section 6.5.1

Now I will explain the flow graph of DSP filtering stage designed in GRC platform shown in Figure 6.3. The first and second block are UHD USRP Source and Complex to Float.

Moreover within the GRC framework, the next stage of the SDR-based system is the DC-block stage (Figure 6.4d). As explained earlier, this stage performs a moving average of the incoming signal, effectively rejecting low-frequency components with a -3 dB high-pass frequency of 10-100 kHz, depending on the chosen baud rate. Following the DC block, an AGC block with a 1 ms update rate and maximum gain of 10,000 is applied to dynamically amplify the received signal. The amplified signal then passes through a low-pass filter block with a cutoff frequency of 4 MHz. Subsequently, in next stage the signal is digitized by a software discriminator block with an adjustable threshold, generating a TTL logic signal. This logic signal is then fed into the Arduino RX board for further processing and analysis.

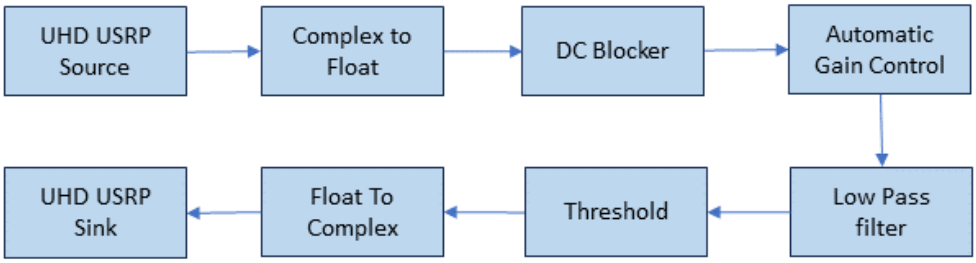

Figure 6.3: Block diagram of DSP filter stage GRC flowgraph.

The final block is the UHD USRP Sink. The primary function of this block is to transmit signals from the flowgraph to USRP, which is a hardware device for SDR. The inclusion of the SDR-based filter stage allows for the implementation of complex filtering and digital signal processing algorithms, which can be executed on the FPGA-based SDR board. This configuration offers more flexibility and advanced signal processing capabilities compared to the previous configurations, enabling enhanced performance in VLC applications.

6.3.2 Receiver Stage Configurations

Moreover in order to explore the performance of the developed SDR based DSP filter stage, the research work explores three different configurations of the RX stage, while keeping the TX configuration unchanged. These configurations are depicted in Figure 6.4.

Direct Arduino System: This corresponds to the original configuration discussed in the

reference paper [40]. In this configuration (Figure 6.4a), the photodetector (PD) is directly connected to the input of the Arduino-based RX stage. The RX board itself performs the digitization of the received signal by means of Schmitt-trigger comparator.

Bridge System: In this configuration (Figure 6.4b), an SDR is inserted between the output of the PD and the input of the RX block. The SDR is equipped with software that replicates the input signal and bridges it to the comparator stage of the RX board. This configuration allows for quantifying the excess noise introduced into the RX stage due to the presence of an additional SDR stage.

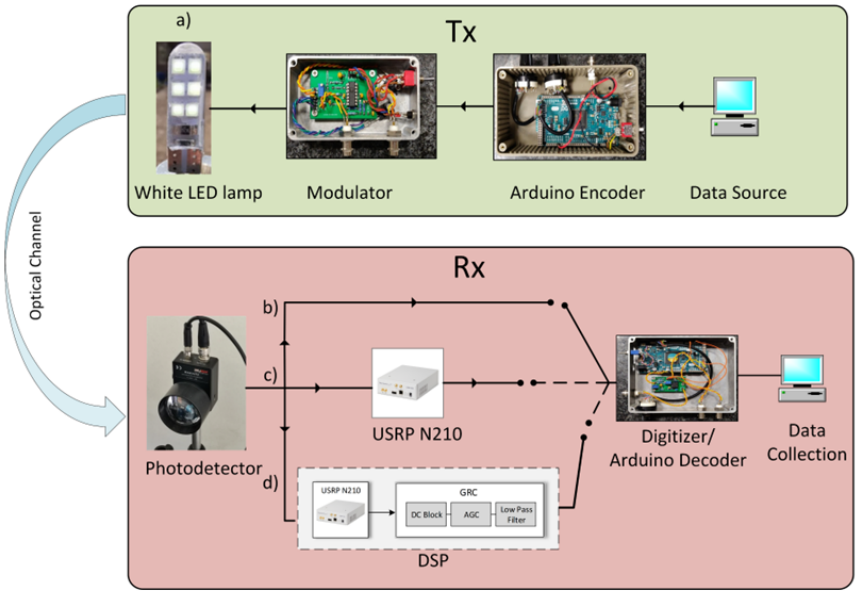

Figure 6.4: VLC system block diagram: (**a**) The green panel shows the block diagram of TX hardware, including the data packet generator and current modulator, which supplies the automotive LED lamp. The pink panel shows the VLC RX hardware system used for the three configurations analyzed, (**b**) *Direct Arduino System*, (**c**) *Bridge System,* and (**d**) *Full System*. For all three configurations, the digitization and decoding process is performed by the Arduino RX Digitizer/Decoder board, which also performs a byte-wise comparison for PER calculation.

Full System: Figure 6.4c shows recently developed *full system* which incorporates a

fully operational SDR-based filter stage integrated between the PD and discriminator at the RX. Utilizing the SDR-based system enables the integration of intricate filtering and DSP blocks, executed on an FPGA-based SDR board. The hardware component of the SDR system utilizes an Ettus Research USRP-N210 [131] system equipped with 30 MHz and RFTX daughterboards [132]. The SDR-based DSP stage [133] is implemented using the open-source GRC software [130], the block diagram of flowgraph implemented in GRC is explained in Section 6.3.1. The sampling rate is configured to 20 Ms/s, constrained by the data handling capabilities of the USRP boards.

The purpose of testing these different configurations is to evaluate the impact of using the SDR as a bridging component and to analyze the additional noise introduced by this setup. By comparing the performance of the direct Arduino system with the bridge system, insights can be gained into the effectiveness and limitations of each configuration in VLC applications.

6.4 Model and Data Analysis

In this section, we will provide details about the data analysis and the mathematical expression used to evaluate the performance of our system.

Assuming a uniform distribution of error bits within bad packets, the PER can be related to the Bit Error Rate (BER) using the following expression [135]:

$$\mathrm{PER} = 1 - (1 - \mathrm{BER})^{N} \tag{6.1}$$

Here, N represents the number of bits in a single packet, which in our case is $N = 32$.

In the case of OOK modulation and an AWGN channel, there is a well-known relationship between BER and SNR. By incorporating this relationship, we can further expand the equation to:

$$\text{PER} = 1 - \left[1 - 0.5erfc\left(\frac{E_b}{N_0}\right)\right]^N \tag{6.2}$$

Here, E_b represents the energy carried by a single bit, and N_0 is the noise power spectral density. By utilizing these mathematical expressions, we can evaluate the system's performance and analyze the relationship between the PER and the BER, taking into account the specific characteristics of our modulation scheme and the noise conditions in the channel.

The above expression can be written as:

$$\text{PER} = 1 - \left[1 - 0.5\,erfc\left(\frac{a(x - x_c)}{2\sqrt{r}w}\right)\right]^N \tag{6.3}$$

In equation 6.3, the variables are defined as follows:

x represents the amplitude of the measured signal at the comparator stage. x_c is the threshold value at the comparator stage. α is a rescaling factor that accounts for the differences in gain values between the USRP and the input impedance of the three setups. It ensures that identical OS result in the same values after passing through the PD stage. w is the RMS value of the noise present at the discriminator stage. This noise can be either hardware or software, depending on the specific configuration. r is a factor that takes into account the shape of the signal. For a square signal, as is the case in our system, r is equal to 1. For a sinusoidal signal with BW limitations, r would be equal to 2. By incorporating these variables into equation 6.3 we can evaluate the relationship between the measured signal amplitude, the threshold value, the noise level, and the specific characteristics of the signal being analyzed. This equation allows us to determine the performance and analyze the behavior of our system in different configurations and noise conditions.

6.5 Results and discussion

6.5.1 Effect of DC-blocker on input BW

In the first step I will discuss the effect of DC-block on input BW characterized by experimental campaigns. The experimental results of the input BW of the DC-block stage are shown in a Figure 6.5. The black line represents the -3 dB BW of the system without the DC-blocker. The red curve corresponds to a delay line length of 20 samples, which achieves a low-frequency cut of 300 kHz suitable for baud rates of 2.5 MBaud and above. The green line represents the input BW for a baud rate of 500 kBaud, requiring a delay length of 200 samples. The orange line corresponds to a baud rate of 115 kBaud and a delay length of 2000 samples. By characterizing the input BW of the DC-block stage for different baud rates, the appropriate configuration can be chosen to effectively block the DC and low-frequency components of the incoming signal depending on the required frequencies BW and improve the performance of the VLC system.

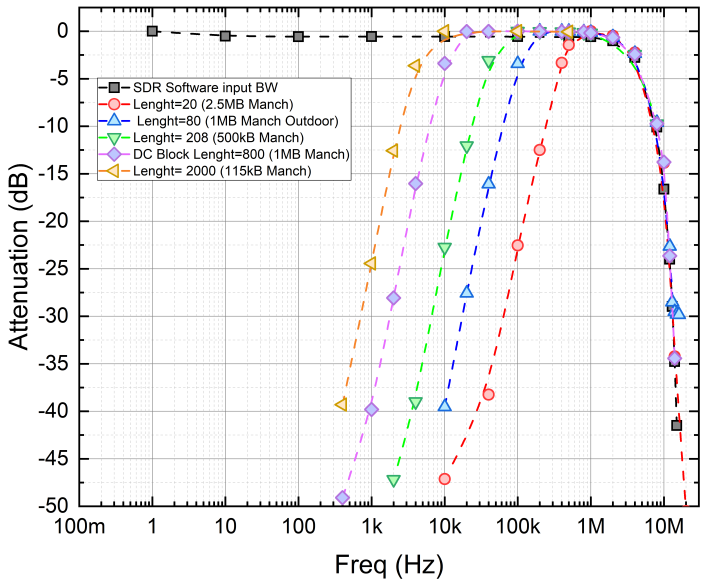

Figure 6.5: Input BW: results obtained by varying the length of the delay line in DC-block algorithm.

In the experiments conducted, the amplitude of the received signal and the relative SNR level were measured at various points in the signal chain. This measurement was achieved using dedicated software blocks in the SDR system or a 4-channel Tektronix digital oscilloscope (MDO3024). The OS, amplified by the photodetector (PD), was fed into the USRP for real-time processing. To evaluate the performance of the different setups and refine the filtering software, a comparative analysis was conducted as a first experimental test (Section 6.5.2). The results of this analysis are presented in the respective section. In Section 6.5.3, an indoor scenario was analyzed focusing on the impact of strong 100-Hz stray lights on the VLC communication link. The experimental setup for this scenario is depicted in Figure 6.6. In Section 6.5.4, the potential of the system in an outdoor environment was demonstrated considering the presence of strong solar irradiance. The outdoor experiment was conducted during the peak solar irradiance period, between 12 pm and 2 pm. The experimental setup for the outdoor scenario is shown in Figure 4.3. By conducting these experiments, the performance and capabilities of the system were evaluated under different conditions, allowing for a comprehensive analysis of the VLC communication link.

In Section 6.5.2, the performance of all three systems was tested indoors with the artificial lights turned off. The purpose was to compare the performance of the systems under controlled conditions and evaluate their effectiveness in the absence of additional light sources. In Section 6.5.3, the focus was on demonstrating the effectiveness of our SDR-based DSP stage in rejecting artificial light interference. The experiments were conducted to evaluate the system's ability to filter out unwanted artificial light components and improve the overall performance of the VLC communication link. Lastly, in Section 6.5.4, the outdoor communication scenario was investigated. The experiments were conducted during a period of high solar irradiance to assess the system's performance under challenging outdoor conditions. The goal was to characterize the system's performance and analyze its ability to maintain reliable communication in the presence of strong solar irradiance. By conducting these experiments and analyzing the results, the research work provides insights into the

performance and capabilities of the system in different scenarios, both indoors and outdoors, and under various conditions.

6.5.2 Comparison of the Three Systems: Indoor Tests

Indoor tests are conducted to determine the maximum performance limits of the VLC communication setup and evaluate the effectiveness of the SDR-based filter stage the flowgraph of which is explained in Section 6.3.1 in rejecting artificial light interference and reducing electronic noise on the VLC link.

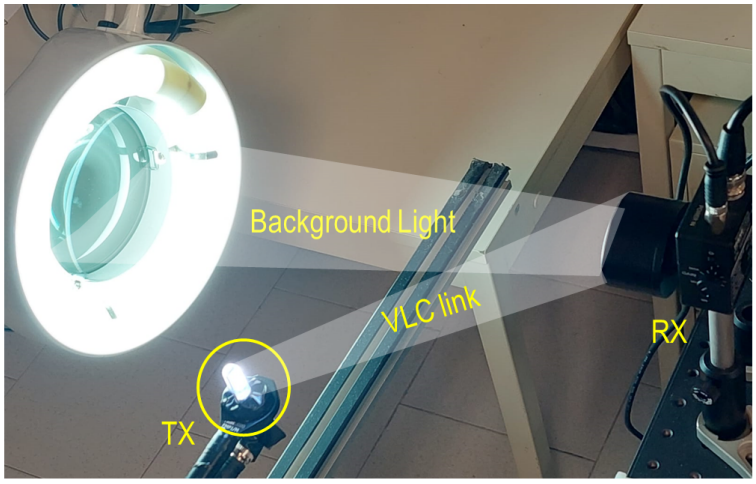

Figure 6.6: Indoor measurements experimental setup in the presence of strong background light

Figure 6.7 shows the PER for all of the three configurations, recorded as a function of OS, which has been varied by controlling the amount of LED light collected by the PD. In order to compare the performances of the systems in equivalent conditions, we normalize the signal amplitude recorded by the PD stage in the three configurations after compensation of the different impedance and electronic amplification factors which could differ case by case (factor α in Table 6.1). The comparison highlights a very strong enhancement of the sensitivity of the RX stage introduced by the SDR stage, which allows for error-free communications for OS values (red symbols) as low as 1/10 of the original value (black symbols). This improvement is made evident also by the eye patterns reported in Figure 6.8

a,b where in Figure 6.8a the eye pattern is closed indicating that there is more noise and the signal is distorted, where as in Figure 6.8b shows that eye pattern is open indicating that noise is filtered efficiently and the received signal is of good quality.

The *bridge* configuration does not introduce significant discrepancies with respect to the original system, as expected, meaning that the excess noise introduced by the SDR block is negligible as compared to the optical channel noise affecting the VLC link in our condition.

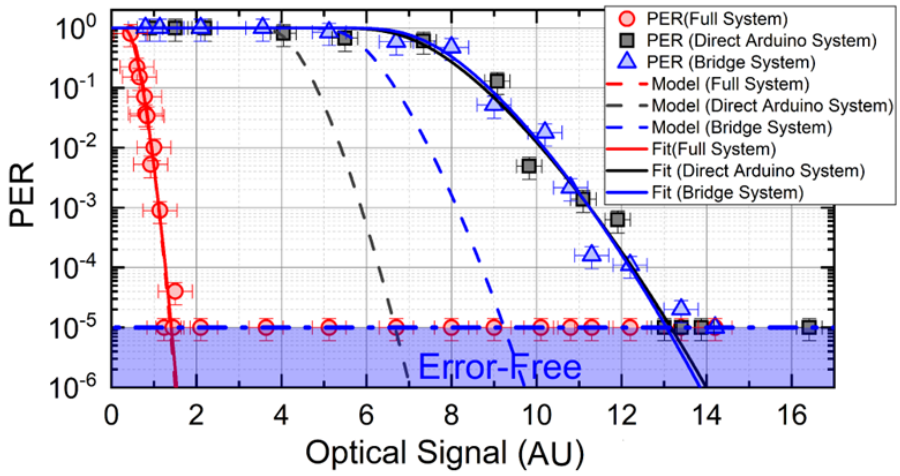

Figure 6.7: PER as a function of the OS: comparison between the three experimental systems used.

In Figure 6.7, the dashed lines represent the predictions of the model discussed in Section 6.4. The model is developed based on the experimental parameters listed in Table 6.1. It provides a theoretical estimation of the system's performance under different configurations. Experimental measurements of noise RMS values (w) are taken before the comparator stage of the RX board using a digital oscilloscope for both the *Direct Arduino System* and *bridge system*. These measured values are then used in Equation 6.3 to calculate the predicted PER values. For the *full system*, where a software discriminator block is used, the noise RMS is measured before this block using a dedicated software block. This measurement is also used in Equation 6.3 to determine the predicted PER.

The observed discrepancy between the model predictions and experimental data for the *Bridge* and *Direct Arduino* configurations can be attributed to an additional source of uncer-

tainty that affects the Arduino-based RX discriminator. This uncertainty is not accounted for in the model indeed.

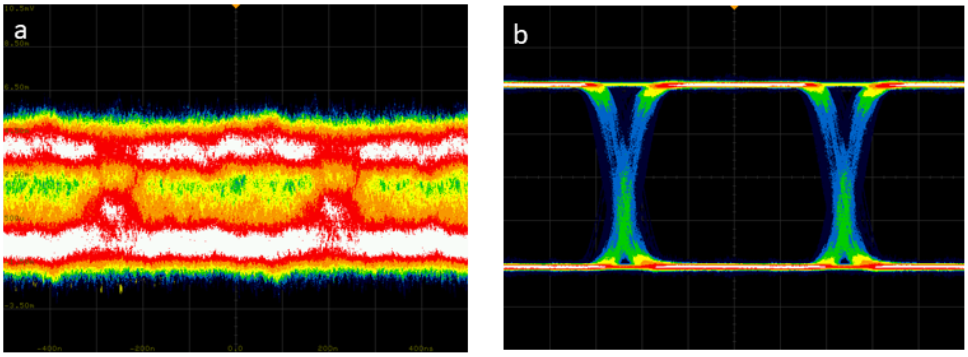

Figure 6.8: (**a**)Eye diagrams related to OS = 5 AU case of the panel recorded for direct PD output and (**b**) after SDR output (*full system*)

In both the *Direct Arduino* and *Bridge* systems, the discrimination process is performed by a physical comparator stage. However, due to low signal levels and other factors, such as finite BW and hysteresis, residual self-oscillation phenomena can occur, leading to false triggering and jitters in the digitized signal that is fed to the Arduino. This introduces additional noise and uncertainty in these configurations. In contrast, the *full* system with the software discriminator stage effectively suppresses this noise by employing multiple filtering stages before providing the signal to the physical comparator.

To account for this additional noise factor in the *Bridge* and *Direct Arduino* configurations, the experimental data are plotted against the predictions of a fit. The fit is computed by leaving either w and/or x_c as free parameters in Equation 6.3. The best-fitting parameters for each configuration are provided in Table 6.1. This fitting approach helps to capture and quantify the extra noise contribution in these configurations. On the other hand, the *full* system, which incorporates the SDR DSP stage, shows a better agreement between the experimental data and the model predictions. Interestingly, the model for the *full* system does not require any additional free parameters, this suggests that the SDR DSP stage can be efficiently modeled by Equation 6.3.

Table 6.1: Parameters used for the model and fit in Figure 6.7

	Full System $\alpha = 0.714$		*Bridge System* $\alpha = 1.25$		*Arduino System* $\alpha = 1.73$	
	Model	Fit	Model	Fit	Model	Fit
Threshold x_c (mV)	0	0 (fixed)	3.6	3.87	2.6	3.46
RMS noise w (mV)	0.14	0.15	1.0	1.63	1.0	2.38

6.5.3 Rejection of Artificial Light Contribution

Noise at frequencies of 100 Hz and its harmonics produced by fluorescent tubes or halogen lamps, can introduce disturbances in the received signal. Additionally, the slow movements of people and objects in the room can also contribute to this interference. Furthermore, the AC-switching frequency of fluorescent lamp drivers, ranging from 100-500 kHz, can have a detrimental effect on VLC links if appropriate filter stages are not employed. This effect becomes more pronounced when dealing with low received signal amplitudes. In such cases, in hardware decision based schemes, noise-induced fluctuations can cause the signal to fall outside the digitization threshold of the physical comparator, leading to errors in signal detection and decoding. To address these challenges, careful design and implementation of filter stages are necessary. The filters should be designed to suppress the interference caused by the low-frequency components of the fluorescent lights and other sources. Additionally, techniques such as adaptive thresholding and signal processing algorithms can be employed to improve the robustness of the system against noise-induced fluctuations and variations in received signal strength. In the experiments conducted in the indoor environment, the performance of the *full* system was evaluated in the presence of varying background light intensity emitted by a neon lamp and collected by the PD shown in Figure 6.9. The upper

panel in Figure 6.9 shows the received OS when there is no background light, while in the lower panel a combination of received OS and noise induced fluctuation by background light is shown.

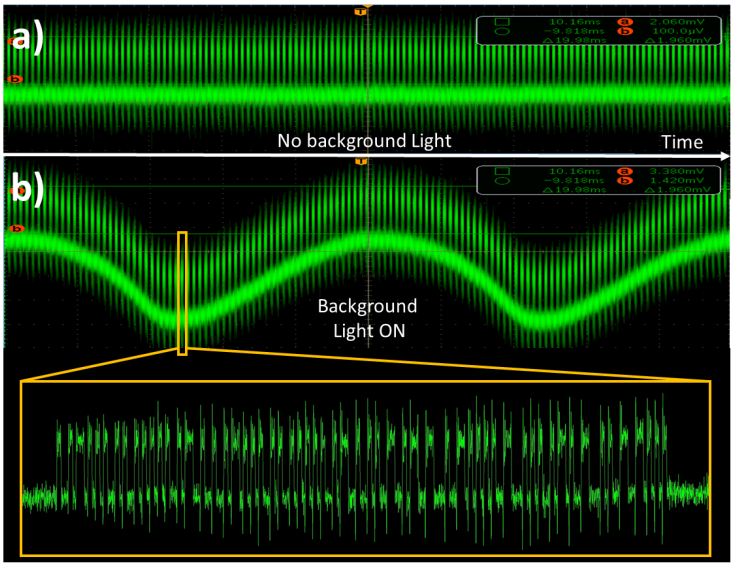

Figure 6.9: Example of OS after PD amplification with artificial light off (**a**) and on (**b**), respectively.

As shown these fluctuations can bring signal out of the digitization threshold of the physical comparator. The objective was to assess the system's ability to maintain a low PER under different levels of background light interference.

The results of this analysis are presented in Figure 6.10. Three different noise levels, represented by w (4.17 mV, 14.7 mV, and 31.6 mV), were achieved by adjusting the distance between the neon lamp and the photodetector. The black symbols in the plot correspond to the case when the background lights were turned off. The PER values obtained for each noise level and background light condition provide insights into the system's robustness against interference. By analyzing the data, it is possible to observe how the PER increases as the background light intensity (noise level) increases. This demonstrates the impact of background light interference on the system's performance. The ability to maintain low PER values even with higher noise levels indicates the effectiveness of the filtering and signal processing techniques employed in the *full* system.

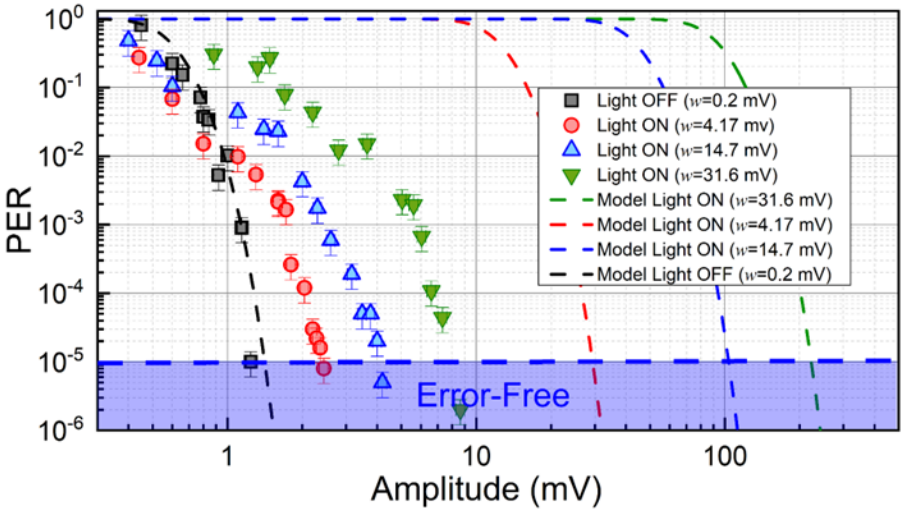

Figure 6.10: Effect of indoor background light intensity on communication quality in terms of PER, for 3 different levels of background illuminance: PER vs. signal amplitude at the RX.

The dashed lines in Figure 6.10 represent the predictions of Equation 6.3 when using the measured value of w at the PD output. These lines illustrate the expected performance of the VLC system under different noise conditions without SDR filtering. Figure 6.10 shows that the *Full* configuration enables error-free communication even when the background RMS noise exceeds three times the OS amplitude ($w = 31.6$ mV). The effectiveness of the DSP stage is further demonstrated in Figure 6.11 where PER is plotted against the SNR after the PD stage. In the most challenging noise scenario (green symbols), a noise margin of -17 dB is observed in the low-PER region (PER $= 1 \times 10^{-5}$).

The black dots and dashed line in the graph represent the data and model predictions, respectively, for the scenario without background lights, where a noise margin of +10 dB is required. These results demonstrate that the improvement in the noise margin for high levels of noise is always greater than 27 dB in the low-PER region. Furthermore, this improvement continues to increase reaching 40 dB in the high-PER region (PER $= 1 \times 10^{-1}$).

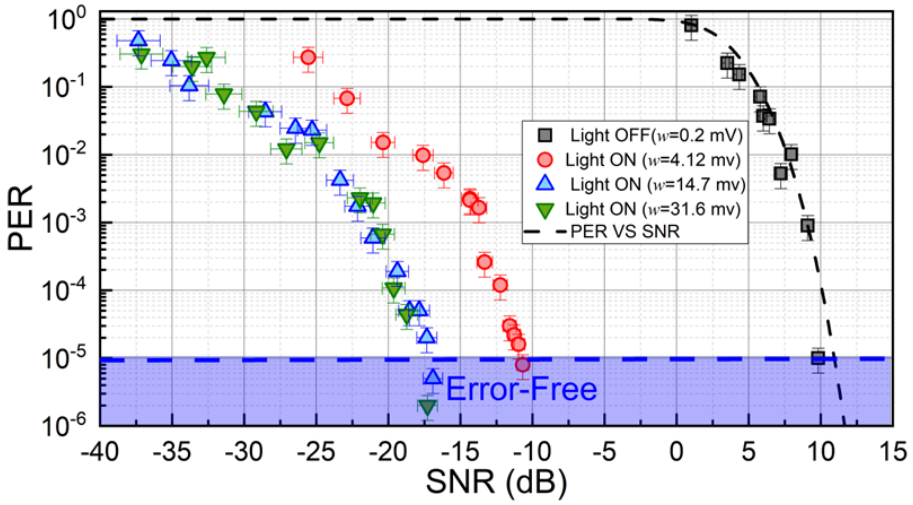

Figure 6.11: Effect of indoor background light intensity on communication quality in terms of PER, for 3 different levels of background illuminance: PER vs. measured SNR.

6.5.4 Outdoor Tests

An outdoor analysis to assess the performance of the VLC link under direct solar irradiance conditions was conducted as shown in Figure 6.12. We specifically tested the system with typical luminous fluxes of 1.2×10^4 lx, which represents a challenging scenario for real-world VLC applications. In this analysis, the focus was on comparing the performance of the *Direct Arduino* system and the *full* system. Since the *Bridge* configuration did not show significant discrepancies as compared to the original system, it was not included in this analysis. For these measurements, APD Thorlabs APD430A/M was used which has small active area to reduce the FoV, which limits the environmental induced stray light components at the RX.

The existence of high levels of background solar irradiance leads to a significant contribution of shot noise in the photocurrent, as mentioned in [136]. This shot noise has a white spectrum, and the process of filtering it out is typically more challenging compared to the indoor scenario. In indoor environments, the RX is not effected by saturation effects and shot noise, the only dominant noise contribution is flicker noise range below 1 kHz produced by fluorescent lamps or halogen tubes.

Figure 6.12: Outdoor measurements setup under strong solar irradiance.

Figure 6.13 presents a comparison of the PER as a function of the distance between the TX and RX stages for both the *Direct Arduino* and *full* systems. The *Direct Arduino* system, benefiting from a low-frequency cutoff at the PD stage [102], achieves error-free communication distances of up to 5 m. However, with the *full* system, the error-free distance is extended to 7.5 m, which is 1.6 times longer than the *Direct Arduino* system. Moreover, successful communications are observed at distances up to 10 m with the *full* system.

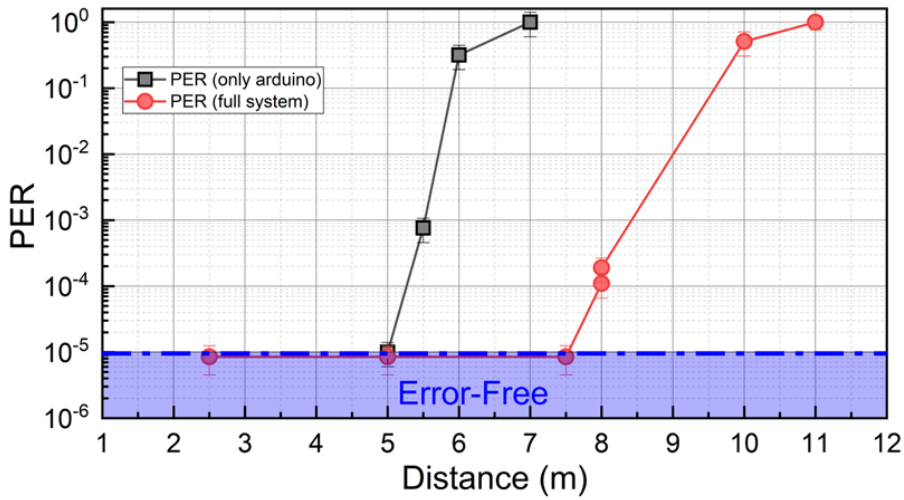

Figure 6.13: Outdoor tests: PER as a function of the distance between TX and RX, under a solar irradiance of 12,000 lux. Results were obtained with the traditional system (black) and the *full* SDR system (red).

This outcome is noteworthy since the V5W LED, is widely used in the automotive industry. This finding suggests that practical VLC Intelligent Transportation Systems (ITS) protocols could also be implemented in existing vehicles without requiring specialized high-power LED sources. It is worth noting that by reducing the baud rate, higher E_b/N_o ratios can be attained at a specific distance (as discussed in Section 6.4) leading to even greater error-free communication distances.

6.6 Summary

An extensive indoor and outdoor evaluation of an innovative VLC system that incorporates a digital DSP filter stage built on SDR technology for the active and dynamic elimination of environmental background noise is reported in this thesis. In order to experimentally demonstrate, compare and quantify, for the first time, the improvement brought by an SDR-based DSP stage in realistic indoor and outdoor (direct sunlight) VLC applications, for a baud rate of 1 Mbaud, the DSP filter stage is coupled with a low-cost VLC prototype based on Arduino that was previously developed. The system's modular design enables it to be copied on existing VLC implementations, which makes practically any VLC system significantly less vulnerable to the negative background light effects and fluctuating signal levels that are a major problem in indoor VLC applications. The SDR-based unit improves the achievable error-free communication distance by a factor of 1.6 in comparison to the original instance when used outdoors under direct solar illumination up to 12,000 lux, and successful communication up to 10 m is seen. The difficulty of conducting tests outside is exacerbated by non-uniform surfaces, wind speed, and other environmental conditions, as well as by the fact that typical outdoor applications demand VLC longer link lengths than typical indoor cases.

In conclusion, the use of DSP techniques significantly enhances the performance of VLC RX, improving resilience to both electronic noise and that generated by background lights.

This is crucial when there are broad-spectrum light sources present, like white LEDs, for which an optical filtering solution cannot be used. Implementing higher-order modulation methods and eliminating multi-path effects are the main areas of my ongoing research.

Chapter 7

Hybrid Smart Window for VLC and Cryogen-Free QCL System (An Outlook)

7.1 Hybrid Smart Window for VLC

In the context of ongoing climate change and the profound need to transition to renewable energy sources is on top priority. This sense of urgency has been further underscored by governing bodies like European Union (EU) [137, 138], emphasizing that new buildings achieve (near) zero energy status. This regulatory landscape has pushed Building Integrated Photovoltaics (BIPV). [139] into a pivotal role, seeking to seamlessly incorporate photovoltaic elements into the fabric of building envelopes. In this context, LSCs offer the possibility of integrating photovoltaics in a way that is particularly well suited to architectural aesthetics [140, 141, 142, 143].

Significantly, the advantages from the integration of LSC in as BIPV extend beyond energy harvesting, presenting a pivotal opportunity to realize second most important pillar of modern architecture. This invloves to connectivity and the IoT [144], as it opens up avenues

for the creation of self-powered, interconnected intelligent facades. These facades possess the capability to seamlessly exchange information and receive instructions for specific functionalities, such as integrated sensors, and wireless data transfer. Notably recent research [73] has showcased the efficacy of CuInS2 Q-dots based LSC waveguides as antennas, facilitating error-free OWC over substantial distances (up to 60 meters). The achieved baud rates reach up to 1 Mb/s through modulation of 405 nm light. This pioneering effort not only taps into the opportunities presented by VLC and Li-Fi in the IoT revolution but also lays the groundwork for the realization of hybrid smart windows. These windows boast dual functionalities, seamlessly combining energy harvesting capabilities with VLC communication, thereby contributing to the advancement of intelligent and energy-efficient building technologies.

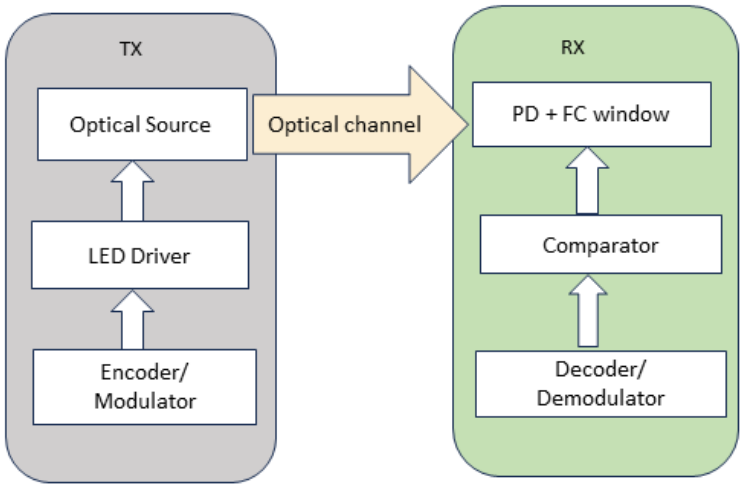

Figure 7.1: PER measurements for different mutual positioning between spotlight and FC window.

To delve into this promising realm, at LENS a comprehensive performance analysis of the CuInS2 Q-dots LSC slab as an optical RX in VLC applications was conducted with the collaboration of University of Milan Bicocca and Glass to power company. Here in this thesis I will briefly describe the initial experimental campaign we conducted at LENS for the realization of VLC.

7.1.1 Experimental Setup

In the VLC TX stage shown in Figure 7.1, where an encoder is based on Arduino DUE microcontroller is used to generate continuous transmission of 32-bit packets, with digital information modulated by specially designed current driver which is discussed in Section 2.1.1. The used optical source is based on high-power white spotlight-type LED lights (Exenia Museo Mini 2L, 300 KHz modulation BW) as the VLC TX stage. Positioned on the ceiling at an approximate height of 3 meters from the floor, this configuration aims to replicate a realistic scenario as shown in Figure 7.2. On the RX side, a Q-Dots based LSC slab, measuring 38 cm × 38 cm, produced by researchers at University of Milan Bicocca which is integrated with a rectangular PD with an active area measuring 3 mm × 30 mm (Hamamatsu, S3588-09), placed at the midpoint of one of the slab's edges as shown in Figure 7.2.

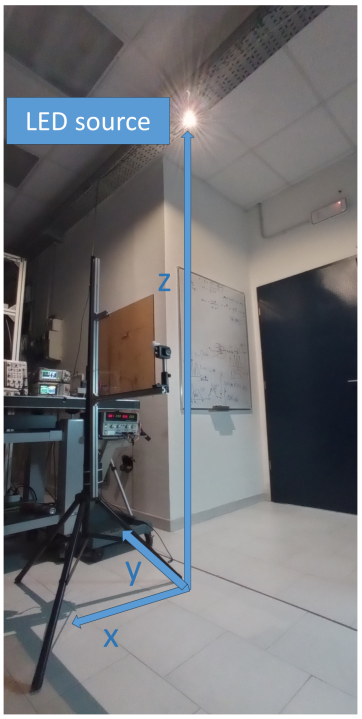

Figure 7.2: Sketch of the VLC smart window test setup and coordinate system used.

The incoming OS is received by large area LSC slab which is coupled with a PD. The

photocurrent generated by the PD undergoes amplification through a custom AC-coupled TIA stage as discussed in Section 2.1. Subsequently, the received signal is digitized by a Schmitt trigger comparator, decoded, and byte-wise compared with a preloaded reference packet for PER calculation (for details Section 2.1) by Arduino DUE microcontroller. In our VLC tests, the LED spotlight is fixed to the ceiling as shown in Figure 7.2, directing light downwards from a height of $z = 2.8$ m, replicating the average height for a typical room. The LSC slab is positioned at $z = 1.55$ m above the floor, and the coordinate x is changed.

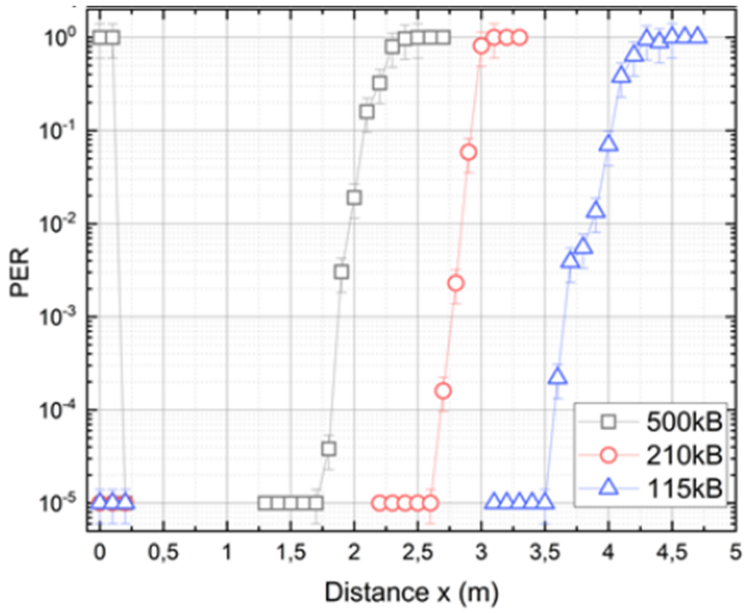

Figure 7.3: PER vs distance measurements for different baudrates.

7.1.2 Communication performance

Error-free transmission is represented by PER values lower than 10^{-5} for different baudrates. To evaluate the quality of the optical channel, experimental tests include measuring the PER, defined as the ratio of lost packets to the total number of transmitted packets. A packet is considered incorrect if even a single bit is lost during transmission. The minimum observable PER 10^{-5} is constrained by the maximum number of transmitted packets 10^5. Interestingly our VLC window prototype exhibits error-free transmission up to $x < 3.5$ m

for 500 kBaud Manchester and $x < 1.7$ m for 115 KBauds. This is expected because lower baudrates exhibits large energy per bit allowing large gain PD with high SNR vales [40].

7.1.3 Summary

In this thesis the potential of hybrid LSC based energy harvesting window is explored as OAs for light communication. The capability of smart window for VLC and Li-Fi is successfully presented, even in challenging conditions of intense sunlight. The achieved baud rates reach up to 500 kBaud through modulation of spotlight-type ceiling LED lights. These findings mark a significant advancement towards the practical implementation of smart buildings.

7.2 QCL-based THz Optical Wireless Communication Link

Wireless data is growing exponentially, so the demand for high data rates also. The wireless networks are developing to meet the increasing demand for higher data rates (ranging from several hundreds of Gbps to several Tbps) along with low latency ($<$ 10 ms). This is crucial for accessing various emerging applications within 6G network. The current research direction involves exploring carrier frequencies beyond the limits set by RF or millimeter wave (mmWave) spectra. The THz band offers intrinsic accessibility to data rates surpassing the Tbps threshold, presenting the primary advantage of this frequency range for wireless communication systems. Additionally, THz radiation, characterized by a longer wavelength compared to infrared (IR) and visible waves, exhibits inherent robustness against Rayleigh scattering caused by dust, smoke, and particulate matter in the atmosphere[145]. This makes the THz band well-suited for communication links in challenging environments and industrial applications. Nevertheless, the THz spectral window experiences water vapor absorption in the atmosphere, primarily restricting the range of terrestrial THz wireless communication (TWC) links to approximately 10 m. In contrast, this factor is entirely inconsequential for intersatellite links (ISLs). Currently, only the 0.3-0.6 THz range has been investigated, and various wireless communication links have been documented in this sub-THz spectral region, which remains accessible using electronics-based devices [146]. Free space optical communication (FSOC) links within the 2-5 THz BW are enabled by high-power THz QCLs. Nevertheless, in all reported setups thus far, both the utilized sources and receivers, specifically quantum well PDs, necessitate intense cryogenic cooling, around 10 K [147, 148], achieving reported data rates of up to 20 Mbps over distances of approximately $\approx$2 m. In this thesis I will present first experimental realization of a cryogen-free QCL-based TWC link, suitable for transportable solutions

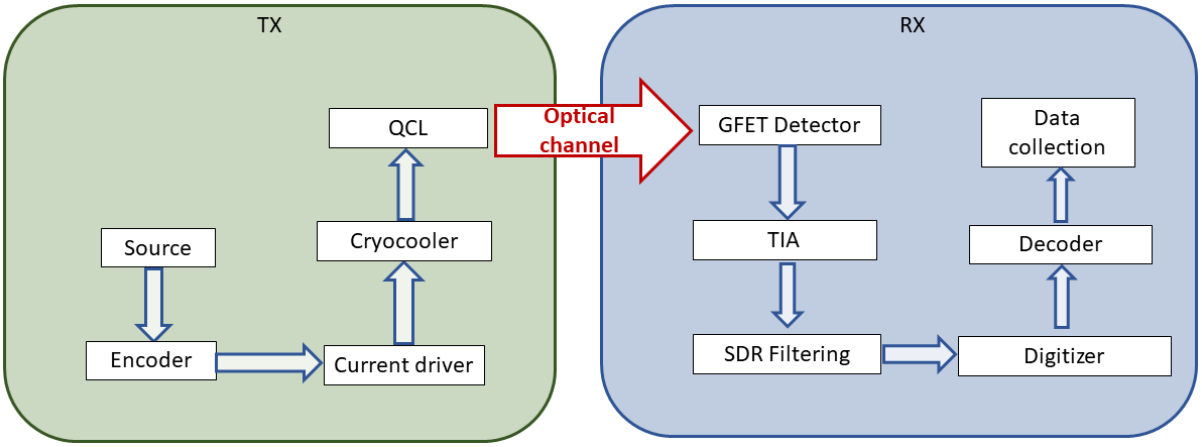

Figure 7.4: Block diagram THz communication system. The TX block diagram features an Arduino DUE board responsible for encoding the signal. The TX block produces a sequence of packets transmitted through the optical free-space channel, comprising a QCL housed in a Stirling cryocooler and a room-temperature GFET detector. The RX block illustrates the block diagram RX incorporating digital decoding, executed using a second Arduino DUE board. The GFET detector output undergoes amplification through a variable-gain TIA, followed by signal filtration via an SDR-based DSP filter stage. Next, the signal is digitized using a single-threshold Schmitt comparator and decoded using another Arduino DUE board, which conducts a byte-wise comparison for PER calculation.

7.2.1 Experimental setup

THz-FSOC link was developed using a source based on 2.83 THz cryogen-free QCL- and a detector based on solid-state graphene-based field-effect transistor (GFET). The Cryostat QCL (source) and GFET detector (receiver) were developed by NEST laboratory in Pisa, Italy. The fabrication of Cryostat QCL and GFET detector is beyond the scope of this thesis. Here I will only present preliminary communication results carried out by these newly developed Cryostat QCL and GFET detector.

Furthermore, at TX an Arduino DUE based encoder generate a stream of packets at various baud rates. The digital information is encoded in the THz QCL source using intensity modulation ranging from 0% (laser below threshold turned off) to 100% (laser turned on at nominal power, approximately ∼1 mW), employing an OOK modulation scheme with Manchester encoding. The QCL achieves operational temperatures feasible with compact

closed-cycle cryostat (in this case, a K353 Stirling cryocooler by Ricor is utilized) and is stabilized at 38.4 K when driven with a continuous current of 570 mA. The QCL's emitted radiation undergoes collimation through parabolic mirrors onto the GFET detector [6].

At RX side shown in Figure 7.4 the signal is detected by GFET detector, the modulated THz beam reaches the RX stage and undergoes conversion into an electric signal. Subsequently, a variable-gain TIA amplifies the signal, and a digital filter is implemented through a SDR-based DSP stage to filter excess noise before transferring it to a Arduino DUE based digitizer/decoder stage [149]. At decoder the PER is calculated as the ratio of the number of correctly received packets (as decoded by the RX unit) to the total number of packets sent by the TX in each experimental run, amounting to PER 10^{-5}.

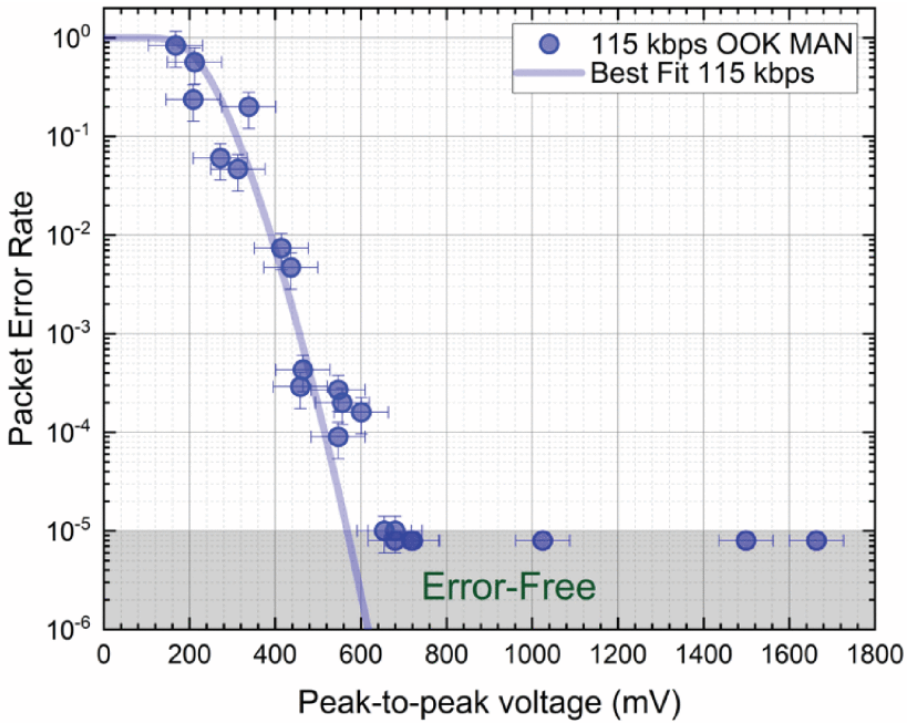

Figure 7.5: Communication performance results: PER vs. peak-to-peak voltage amplitude for 115 kbps OOK with Manchester encoding.

Initial tests on the communication link were conducted in a laboratory setting, capturing the PER at various signal amplitudes is shown in Figure 7.5. These tests demonstrated error-free communication when the peak-to-peak amplitude of signal is around 580 mV and no

communication occurs when the amplitude is $<$ 200 mV at 115 kBps up to a distance of approximately $\sim$3 m.

7.2.2 Summary

Preliminary results of a cryogen-free TWC link is system is demonstrated. The performance of system is evaluated by using PER as performance metric. Error free communication is recorded around when the signal is around 580 mV and no communication occurs when the signal amplitude is $<$ 200 mV at 115 kBps. The error free communication was demonstrated up to distance of approximately $\sim$3 m. The strong absorption by water in the atmosphere and the geometrical losses along the optical path are the main factor limiting the distance. This is the first ever THz communication system without using liquid helium cooling system for both TX and RX.

Chapter 8

Conclusion

This is the second thesis on VLC at LENS, in which several applications of VLC are studied. This thesis was focused on development of versatile VLC systems including FC based VLC RX and SDR based DSP filter stage. This study shows the potential of OWC which could serves as an important technology in NGN for indoor WLC to outdoor VLC. The study in Chapter 4 presents an innovative OWC system utilizing a novel large-area FC OA based on photostable $CuInS_2$ Q-Dot fluorophores. A comprehensive analysis was conducted on its lifetime, time response, bandwidth (BW), field of view (FoV), and efficiency concerning the light spot's position on the slab. The observed -3 dB BW exceeds 250 kHz, and the FoV exceeds 80° degrees FWHM for a collimated source. The FC OA coupled with a customized PD was tested in outdoor conditions with direct strong solar irradiance exceeding 70,000 lx, achieving error-free communication at 1 Mbaud NRZ for distances up to 60 m remarkably, the longest reported link length for an FC optical antenna system. The findings suggest that large-area,Q-Dot based FC antennas could be reliably used in realistic long-range optical communication links, making them promising for high-OG RXs in VLC and long-haul FSO links, particularly due to their solid photo-stability and reduced sensitivity to angular misalignments and pointing instabilities

Furthermore, a second study (Chapter 5) focuses on two organic OAs based on fluo-

rophores DQ1 and LR305 for white light VLC. Originally designed for solar energy conversion, these OAs exhibit high conversion efficiency, quick response times (around 10 ns), and suitability for high data rate applications. The research evaluates their performance as optical front ends in a VLC system, analyzing conversion efficiency for various LED sources. LR305-based OAs prove advantageous in WLC applications, demonstrating high SNR as compared to traditional PD-based RXs, particularly for few-MHz-BW IoT applications. On the other hand, DQ1 based FC VLC RXs are more suitable for blue/UV sources due to their larger Stokes shift. The study proposes the use of DQ1 for creating large-BW WLC links while addressing the challenges of white LED spectrum.

Additionally, the study in Chapter 6 presents a comprehensive analysis of an innovative VLC system featuring a DSP filter stage based on SDR technology. The primary focus is on actively and dynamically filtering of the background noise in both indoor and outdoor environments. The experiment involves integrating the SDR-based DSP filter with a conventional low-cost VLC system based on Arduino DUE. The performance of VLC system with and without filter stage was comparing indoor and outdoors for a 1 Mbaud baud rate. The designed DSP stage allows significantly reducing effect of background ambient light. Outdoors, the SDR-based system increases error-free communication distance by 1.6 times compared to the only Arduino based system, particularly under direct solar illumination of up to 12,000 lux, achieving successful communication up to 10 meters.

The findings of Chapters 4 and 5 indicates that it is feasible to create and effectively utilize large-area FC antennas in practical long-range optical communication setups. This makes them well-suited as high-gain VLC RX for different applications. In Chapter 7 a first prototype of Q-dots FC based smart window for VLC is presented. This pioneering effort not only opens new avenues for VLC and Li-Fi in the IoT revolution but also lays the groundwork for the realization of hybrid smart windows. These windows exhibits hybrid functionalities of energy harvesting and VLC. Moreover, these results may significantly influence the advancement of innovative hybrid IoT devices, smart phones, and laptops etc

with integrating capabilities for solar energy harvesting and communication. Additionally, in Chapter 7 first prototype of cryogen-free QCL for THz communication is also presented paving the way to transportable, terrestrial field-deployable and satellite compatible THz links above 2 THz.

However in this thesis the study of FC based VLC RX is limited to OOK modulation scheme, in future a number of other modulation schemes like oorthogonal frequency division multiplexing modulation scheme can be exploited to study the further improvement in the systems. In addition, to effectively remove the background noise SDR based filter can be implemented which can also further be adopted for complex modulations schemes and scenarios like multi path interference, especially in short-range OWC using only SDR.

Bibliography

[1] Mostafa Zaman Chowdhury, Md. Tanvir Hossan, Amirul Islam, and Yeong Min Jang. A comparative survey of optical wireless technologies: Architectures and applications. *IEEE Access*, 6:9819–9840, 2018.

[2] Marco Seminara. Development and characterization of systems for optical wireless and visible light communication. *Univeristy of Florence, Italy*, 2022.

[3] Cheng-Xiang Wang, Xiaohu You, Xiqi Gao, Xiuming Zhu, Zixin Li, Chuan Zhang, Haiming Wang, Yongming Huang, Yunfei Chen, Harald Haas, John S. Thompson, Erik G. Larsson, Marco Di Renzo, Wen Tong, Peiying Zhu, Xuemin Shen, H. Vincent Poor, and Lajos Hanzo. On the road to 6g: Visions, requirements, key technologies, and testbeds. *IEEE Communications Surveys & Tutorials*, 25(2):905–974, 2023.

[4] A. Balmori. Evidence for a health risk by rf on humans living around mobile phone base stations: From radiofrequency sickness to cancer. *Environmental Research*, 214:113851, 2022.

[5] Hugo Rodrigues Dias Filgueiras, Eduardo Saia Lima, Matheus Sêda Borsato Cunha, Celso Henrique De Souza Lopes, Letícia Carneiro De Souza, Ramon Maia Borges, Luiz Augusto Melo Pereira, Tiago Henrique Brandão, Tomás Powell Villena Andrade, Luciano Camilo Alexandre, Geraldo Neto, Agostinho Linhares, Luciano Leonel Mendes, Murilo Araujo Romero, and Arismar Cerqueira S. Wireless and optical convergent access technologies toward 6g. *IEEE Access*, 11:9232–9259, 2023.

[6] Mehran Rafiee, Subhash Chandra, Hind Ahmed, and S.J. McCormack. Optical materials an overview of various configurations of luminescent solar concentrators for photovoltaic applications. *Optical Materials*, 91, 03 2019.

[7] Shlomi Arnon. *Advanced Optical Wireless Communication Systems*. Cambridge University press, 2012.

[8] Luiz Eduardo Mendes Matheus, Alex Borges Vieira, Luiz F. M. Vieira, Marcos A. M. Vieira, and Omprakash Gnawali. Visible light communication: Concepts, applications and challenges. *IEEE Communications Surveys & Tutorials*, 21(4):3204–3237, 2019.

[9] Lifang Feng, Rose Qingyang Hu, Jianping Wang, Peng Xu, and Yi Qian. Applying vlc in 5g networks: Architectures and key technologies. *IEEE Network*, 30(6):77–83, 2016.

[10] Xiaoming Zhu and J.M. Kahn. Free-space optical communication through atmospheric turbulence channels. *IEEE Transactions on Communications*, 50(8):1293–1300, 2002.

[11] Atheer A. Sabri, Samir M. Hameed, and Wael A. H. Hadi. Last mile access-based fso and vlc systems. *Appl. Opt.*, 62(31):8402–8410, Nov 2023.

[12] John Gancarz, Hany Elgala, and Thomas D.C. Little. Impact of lighting requirements on vlc systems. *IEEE Communications Magazine*, 51(12):34–41, 2013.

[13] Fubin Wang, Fang Yang, Changyong Pan, Jian Song, and Zhu Han. Joint illumination and communication optimization in indoor vlc for iot applications. *IEEE Internet of Things Journal*, 9(21):20788–20800, 2022.

[14] Suseela Vappangi and Venkata Mani Vakamulla. Synchronization in visible light communication for smart cities. *IEEE Sensors Journal*, 18(5):1877–1886, 2018.

[15] Alexis A. Dowhuszko, Mehmet C. Ilter, and Jyri Hämäläinen. Visible light communication system in presence of indirect lighting and illumination constraints. In *ICC*

2020 - 2020 IEEE International Conference on Communications (ICC), pages 1–6, 2020.

[16] Latif Ullah Khan. Visible light communication: Applications, architecture, standardization and research challenges. *Digital Communications and Networks*, 3(2):78–88, 2017.

[17] Zuhang Geng, Faisal Nadeem Khan, Xun Guan, and Yuhan Dong. Advances in visible light communication technologies and applications. *Photonics*, 9(12), 2022.

[18] Harald Haas, Liang Yin, Yunlu Wang, and Cheng Chen. What is lifi? *Journal of Lightwave Technology*, 34(6):1533–1544, 2016.

[19] Yuan Zhuang, Luchi Hua, Longning Qi, Jun Yang, Pan Cao, Yue Cao, Yongpeng Wu, John Thompson, and Harald Haas. A survey of positioning systems using visible led lights. *IEEE Communications Surveys Tutorials*, 20(3):1963–1988, 2018.

[20] Anupam Kumari and Darshak Bhatt. Advanced system analysis and survey on the gps receiver front end. *IEEE Access*, 10:24611–24626, 2022.

[21] Stefano Pergoloni, Zeinab Mohamadi, Anna Maria Vegni, Zabih Ghassemlooy, and Mauro Biagi. Visible light indoor positioning through colored leds. In *2017 IEEE International Conference on Communications Workshops (ICC Workshops)*, pages 150–155. IEEE, 2017.

[22] Minchul Kim and Taeweon Suh. A low-cost surveillance and information system for museum using visible light communication. *IEEE Sensors Journal*, 19(4):1533–1541, 2019.

[23] Máximo Morales Céspedes, Borja Genovés Guzmán, and Víctor P. Gil Jiménez. Lights and shadows: A comprehensive survey on cooperative and precoding schemes to overcome los blockage and interference in indoor vlc. *Sensors*, 21(3), 2021.

[24] Ni Xiaolong, Yao Haifeng, Liu Zhi, Chen Chunyi, Meng Ce, and Zhao Jiaxu. Experimental study of the atmospheric turbulence influence on fso communication system. In *2018 Asia Communications and Photonics Conference (ACP)*, pages 1–3, 2018.

[25] IEEE. Iee colloquium on 'optical sources' (digest no.026). In *IEE Colloquium on Optical Sources*, 1990.

[26] Manav R. Bhatnagar and M. K. Arti. Performance analysis of hybrid satellite-terrestrial fso cooperative system. *IEEE Photonics Technology Letters*, 25(22):2197–2200, 2013.

[27] Rajan Miglani, Jagjit Singh Malhotra, Arun K. Majumdar, Faisel Tubbal, and Raad Raad. Multi-hop relay based free space optical communication link for delivering medical services in remote areas. *IEEE Photonics Journal*, 12(4):1–21, 2020.

[28] Bhogeswara Rao Angara, Palanisamy Shanmugam, and Harishankar Ramachandran. Underwater wireless optical communication system channel modelling with oceanic bubbles and water constituents under different wind conditions. *IEEE Photonics Journal*, 15(2):1–11, 2023.

[29] Bastien Béchadergue, H Guan, Luc Chassagne, Samir Tohmé, and Jean-Laurent Franchineau. Visible light communication system for platooning applications. In *Vision 2016 Vehicle and Infrastructure safety improvement in Adverse conditions and Night Driving*, 10 2016.

[30] Yuki Goto, Isamu Takai, Takaya Yamazato, Hiraku Okada, Toshiaki Fujii, Shoji Kawahito, Shintaro Arai, Tomohiro Yendo, and Koji Kamakura. A new automotive vlc system using optical communication image sensor. *IEEE Photonics Journal*, 8(3):1–17, 2016.

[31] M. Akanegawa, Y. Tanaka, and M. Nakagawa. Basic study on traffic information system using led traffic lights. *IEEE Transactions on Intelligent Transportation Systems*, 2(4):197–203, 2001.

[32] Murat Uysal, Zabih Ghassemlooy, Abdelmoula Bekkali, Abdullah Kadri, and Hamid Menouar. Visible light communication for vehicular networking: Performance study of a v2v system using a measured headlamp beam pattern model. *IEEE Vehicular Technology Magazine*, 10:45–53, 2015.

[33] Phat Huynh and Myungsik Yoo. Vlc-based positioning system for an indoor environment using an image sensor and an accelerometer sensor. *Sensors*, 16(6), 2016.

[34] T. Peyronel, K. J. Quirk, S. C. Wang, and T. G. Tiecke. Luminescent detector for free-space optical communication. *Optica*, 3(7):787–792, Jul 2016.

[35] WH Steel. Luminosity, throughput, or etendue? *Applied Optics*, 13(4):704–705, 1974.

[36] Amna Riaz and Steve Collins. A slab fluorescent concentrator for visible light communications. In *2019 2nd IEEE Middle East and North Africa COMMunications Conference (MENACOMM)*, pages 1–4, 2019.

[37] Pavlos P. Manousiadis, Sujan Rajbhandari, Rahmat Mulyawan, Dimali A. Vithanage, Hyunchae Chun, Grahame Faulkner, Dominic C. O'Brien, Graham A. Turnbull, Stephen Collins, and Ifor D.W. Samuel. Wide field-of-view fluorescent antenna for visible light communications beyond the étendue limit. *Optica*, 3(7):702–706, Jul 2016.

[38] Pavlos Manousiadis, Hyunchae Chun, Sujan Rajbhandari, Dimali Vithanage, Rahmat Mulyawan, G. Faulkner, Harald Haas, Dominic O'Brien, Steve Collins, Graham Turnbull, and Ifor Samuel. Optical antennas for wavelength division multiplexing in visible light communications beyond the Étendue limit. *Advanced Optical Materials*, 8, 12 2019.

[39] Arduino. Arduino Due Documentation. *Arduino Web*, Year of access.

[40] Marco Meucci, Marco Seminara, Tassadaq Nawaz, Stefano Caputo, Lorenzo Mucchi, and Jacopo Catani. Bidirectional vehicle-to-vehicle communication system based on vlc: Outdoor tests and performance analysis. *IEEE Transactions on Intelligent Transportation Systems*, pages 1–11, 2021.

[41] Hyunchae Chun, Pavlos Manousiadis, Sujan Rajbhandari, Dimali A. Vithanage, Grahame Faulkner, Dobroslav Tsonev, Jonathan James Donald McKendry, Stefan Videv, Enyuan Xie, Erdan Gu, Martin D. Dawson, Harald Haas, Graham A. Turnbull, Ifor D. W. Samuel, and Dominic C. O'Brien. Visible light communication using a blue gan μ led and fluorescent polymer color converter. *IEEE Photonics Technology Letters*, 26(20):2035–2038, 2014.

[42] Shi Zhang, Zixian Wei, Zhiyuan Cao, Keming Ma, Chien-Ju Chen, Meng-Chyi Wu, Yuhan Dong, and H. Y. Fu. A high-speed visible light communication system using pairs of micro-size leds. *IEEE Photonics Technology Letters*, 33(18):1026–1029, 2021.

[43] Wasiu O. Popoola. Impact of vlc on light emission quality of white leds. *Journal of Lightwave Technology*, 34(10):2526–2532, 2016.

[44] Shao-Wei Wang, Feiliang Chen, Liye Liang, Songlin He, Yiguang Wang, Xiaoshuang Chen, and Wei Lu. A high-performance blue filter for a white-led-based visible light communication system. *IEEE Wireless Communications*, 22(2):61–67, 2015.

[45] Hoa Le Minh, Dominic O'Brien, Grahame Faulkner, Lubin Zeng, Kyungwoo Lee, Daekwang Jung, and YunJe Oh. High-speed visible light communications using multiple-resonant equalization. *IEEE Photonics Technology Letters*, 20(14):1243–1245, 2008.

[46] Hoa Le Minh, Dominic O'Brien, Grahame Faulkner, Lubin Zeng, Kyungwoo Lee, Daekwang Jung, YunJe Oh, and Eun Tae Won. 100-mb/s nrz visible light com-

munications using a postequalized white led. *IEEE Photonics Technology Letters*, 21(15):1063–1065, 2009.

[47] A. M. Khalid, G. Cossu, R. Corsini, P. Choudhury, and E. Ciaramella. 1-gb/s transmission over a phosphorescent white led by using rate-adaptive discrete multitone modulation. *IEEE Photonics Journal*, 4(5):1465–1473, 2012.

[48] Mohammad Abrar Shakil Sejan and Wan-Young Chung. Secure vlc for wide-area indoor iot connectivity. *IEEE Internet of Things Journal*, 10(1):180–193, 2023.

[49] Vitalio Alfonso Reguera, Lucas Teixeira, Carlos Henrique Barriquello, Djeisson Hoffmann Thomas, and Marco Antônio Dalla Costa. Efficient and low-complexity rate and dimming control of vlc for industrial iot applications. *IEEE Journal of Emerging and Selected Topics in Industrial Electronics*, 3(4):1087–1095, 2022.

[50] Jiun-Yu Sung, Chi-Wai Chow, and Chien-Hung Yeh. Is blue optical filter necessary in high speed phosphor-based white light led visible light communications? *Opt. Express*, 22(17):20646–20651, Aug 2014.

[51] Eric Price and David P. Woodruff. Applications of the shannon-hartley theorem to data streams and sparse recovery. In *2012 IEEE International Symposium on Information Theory Proceedings*, pages 2446–2450, 2012.

[52] Mohammad Ali Khalighi and Murat Uysal. Survey on free space optical communication: A communication theory perspective. *IEEE communications surveys & tutorials*, 16(4):2231–2258, 2014.

[53] Hemani Kaushal and Georges Kaddoum. Optical communication in space: Challenges and mitigation techniques. *IEEE communications surveys & tutorials*, 19(1):57–96, 2016.

[54] Zahra Vali, Asghar Gholami, David G Michelson, Zabih Ghassemlooy, Masood Omoomi, and Hamed Noori. Use of gaussian beam divergence to compensate for misalignment of underwater wireless optical communication links. *IET Optoelectronics*, 11(5):171–175, 2017.

[55] Muhammad Salman Bashir and Mark R. Bell. Optical beam position tracking in free-space optical communication systems. *IEEE Transactions on Aerospace and Electronic Systems*, 54(2):520–536, 2018.

[56] Muhammad Ali Umair, Hira Khalid, Sheikh Muhammad Sajid, and Hector E. Nistazakis. Gaussian-shaped free-space optical beam intensity estimation in detector arrays. *Photonics*, 10(8), 2023.

[57] Toshimasa Umezawa, Atsushi Matsumoto, Kouich Akahane, Atsushi Kanno, and Naokatsu Yamamoto. 40-ghz resonant-cavity 2-d photodetector array using inp/ingaas dh structure for advanced optical wireless communications. In *CLEO 2023*, page SF2O.3. Optica Publishing Group, 2023.

[58] Mohammad Dehghani Soltani, Hossein Kazemi, Elham Sarbazi, Taisir E. H. El-Gorashi, Jaafar M. H. Elmirghani, Richard V. Penty, Ian H. White, Harald Haas, and Majid Safari. High-speed imaging receiver design for 6g optical wireless communications: A rate-fov trade-off. *IEEE Transactions on Communications*, 71(2):1024–1043, 2023.

[59] Mostafa Zaman Chowdhury, Md. Shahjalal, Moh. Khalid Hasan, and Yeong Min Jang. The role of optical wireless communication technologies in 5g/6g and iot solutions: Prospects, directions, and challenges. *Applied Sciences*, 9(20), 2019.

[60] Abdulkadir Celik, Imene Romdhane, Georges Kaddoum, and Ahmed M. Eltawil. A top-down survey on optical wireless communications for the internet of things. *IEEE Communications Surveys & Tutorials*, 25(1):1–45, 2023.

[61] Steve Collins, Dominic C. O'Brien, and Andrew Watt. High gain, wide field of view concentrator for optical communications. *Opt. Lett.*, 39(7):1756–1759, Apr 2014.

[62] J. S. Batchelder, A. H. Zewai, and T. Cole. Luminescent solar concentrators. 1: Theory of operation and techniques for performance evaluation. *Appl. Opt.*, 18(18):3090–3110, Sep 1979.

[63] Wilfried G.J.H.M. van Sark, Keith W.J. Barnham, Lenneke H. Slooff, Amanda J. Chatten, Andreas Büchtemann, Andreas Meyer, Sarah J. McCormack, Rolf Koole, Daniel J. Farrell, Rahul Bose, Evert E. Bende, Antonius R. Burgers, Tristram Budel, Jana Quilitz, Manus Kennedy, Toby Meyer, C. De Mello Donegá, Andries Meijerink, and Daniel Vanmaekelbergh. Luminescent solar concentrators - a review of recent results. *Opt. Express*, 16(26):21773–21792, Dec 2008.

[64] Yilin Li, Yujian Sun, and Yongcao Zhang. Luminescent solar concentrators performing under different light conditions. *Solar Energy*, 188:1248–1255, 2019.

[65] Glenn A. Crosby and James N. Demas. Measurement of photoluminescence quantum yields. review. *The Journal of Physical Chemistry*, 75(8):991–1024, 1971.

[66] Muhammad T. Sajjad, Pavlos P. Manousiadis, Hyunchae Chun, Dimali A. Vithanage, Sujan Rajbhandari, Alexander L. Kanibolotsky, Grahame Faulkner, Dominic O'Brien, Peter J. Skabara, Ifor D. W. Samuel, and Graham A. Turnbull. Novel fast color-converter for visible light communication using a blend of conjugated polymers. *ACS Photonics*, 2(2):194–199, February 2015.

[67] Lauren Shea Rohwer and James E. Martin. Measuring the absolute quantum efficiency of luminescent materials. *Journal of Luminescence*, 115(3):77–90, 2005.

[68] Yufeng Zhou, Daniele Benetti, Zhiyuan Fan, Haiguang Zhao, Dongling Ma, Alexander O. Govorov, Alberto Vomiero, and Federico Rosei. Near infrared, highly efficient luminescent solar concentrators. *Advanced Energy Materials*, 6(11):1501913, 2016.

[69] Rahmat Mulyawan, Ariel Gomez, Hyunchae Chun, Sujan Rajbhandari, Pavlos P Manousiadis, Dimali A Vithanage, Grahame Faulkner, Graham A Turnbull, Ifor D W Samuel, Stephen Collins, and Dominic O'Brien. A comparative study of optical concentrators for visible light communications. In Benjamin B Dingel, Katsutoshi Tsukamoto, and Spiros Mikroulis, editors, *Broadband Access Communication Technologies XI*. SPIE, January 2017.

[70] Rahmat Mulyawan, Ariel Gomez, Hyunchae Chun, Sujan Rajbhandari, Pavlos P. Manousiadis, Dimali A. Vithanage, Grahame Faulkner, Graham A. Turnbull, Ifor D. W. Samuel, Stephen Collins, and Dominic O'Brien. A comparative study of optical concentrators for visible light communications. In Benjamin B. Dingel, Katsutoshi Tsukamoto, and Spiros Mikroulis, editors, *Broadband Access Communication Technologies XI*, volume 10128, page 101280L. International Society for Optics and Photonics, SPIE, 2017.

[71] Steve Collins. Smart phones:an example application for fluorescent concentrators. In *2019 Global LIFI Congress (GLC)*, pages 1–4, 2019.

[72] Yurong Dong, Meng Shi, Xilu Yang, Pan Zeng, Junyi Gong, Sunming Zheng, Mengjie Zhang, Rongqing Liang, Qiongrong Ou, Nan Chi, and Shuyu Zhang. Nanopatterned luminescent concentrators for visible light communications. *Opt. Express*, 25(18):21926–21934, Sep 2017.

[73] Muhammad Ali Umair, Marco Seminara, Marco Meucci, Marco Fattori, Francesco Bruni, Sergio Brovelli, Francesco Meinardi, and Jacopo Catani. Long-range optical wireless communication system based on a large-area, q-dots fluorescent antenna. *Laser & Photonics Reviews*, 17(2):2200575, 2023.

[74] Pavlos P. Manousiadis, Hyunchae Chun, Sujan Rajbhandari, Dimali A. Vithanage, Rahmat Mulyawan, Grahame Faulkner, Harald Haas, Dominic C. O'Brien, Steve

Collins, Graham A. Turnbull, and Ifor D. W. Samuel. Optical antennas for wavelength division multiplexing in visible light communications beyond the Étendue limit. *Advanced Optical Materials*, 8(4):1901139, 2020.

[75] Rahmat Mulyawan, Hyunchae Chun, Ariel Gomez, Sujan Rajbhandari, Grahame Faulkner, Pavlos P. Manousiadis, Dimali A. Vithanage, Graham A. Turnbull, Ifor D. W. Samuel, Stephen Collins, and Dominic O'Brien. Mimo visible light communications using a wide field-of-view fluorescent concentrator. *IEEE Photonics Technology Letters*, 29(3):306–309, 2017.

[76] Matteo Sottile, Giovanni Tomei, Silvia Borsacchi, Francesca Martini, Marco Geppi, Giacomo Ruggeri, and Andrea Pucci. Epoxy resin doped with coumarin 6: Example of accessible luminescent collectors. *European Polymer Journal*, 89:23–33, 2017.

[77] D. A. Vithanage, P. P. Manousiadis, M. T. Sajjad, S. Rajbhandari, H. Chun, C. Orofino, D. Cortizo-Lacalle, A. L. Kanibolotsky, G. Faulkner, N. J. Findlay, D. C. O'Brien, P. J. Skabara, I. D. W. Samuel, and G. A. Turnbull. BODIPY star-shaped molecules as solid state colour converters for visible light communications. *Applied Physics Letters*, 109(1):013302, 07 2016.

[78] Wajahat Ali, Pavlos P. Manousiadis, Dominic C O'Brien, Graham A Turnbull, Ifor D. W. Samuel, and Steve Collins. A gigabit vlc receiver that incorporates a fluorescent antenna and a sipm. *Journal of Lightwave Technology*, 40(16):5369–5375, 2022.

[79] M. Portnoi, P.A. Haigh, T.J Macdonald, and et al. Bandwidth limits of luminescent solar concentrators as detectors in free-space optical communication systems. *Light Sci Appl*, 10(3), 2021.

[80] Amna Riaz, Grahame Faulkner, and Steve Collins. A fluorescent antenna for white light visible light communications. In *2019 Global LIFI Congress (GLC)*, pages 1–4, 2019.

[81] Cuiwei He, Yuto Lim, and Hideyuki Murata. Study of using different colors of fluorescent fibers as optical antennas in white led based-visible light communications. *Opt. Express*, 31(3):4015–4028, Jan 2023.

[82] Shaghayegh Chamani, Ali Rostami, and Peyman Mirtaheri. A superimposed qd-based optical antenna for vlc: White led source. *Nanomaterials*, 12(15), 2022.

[83] Wajahat Ali, Pavlos Manousiadis, Dominic C. O'Brien, Graham Turnbull, Ifor Samuel, and Steve Collins. A gigabit vlc receiver that incorporates a fluorescent antenna and a sipm. *Journal of Lightwave Technology*, pages 1–1, 2021.

[84] Dominic C. O'Brien. Visible light communications: Challenges and potential. In *IEEE Photonic Society 24th Annual Meeting*, pages 365–366, 2011.

[85] Jean Roncali. Luminescent solar collectors: Quo vadis? *Advanced Energy Materials*, 10(36):2001907, 2020.

[86] G. Seybold and G. Wagenblast. New perylene and violanthrone dyestuffs for fluorescent collectors. *Dyes and Pigments*, 11(4):303–317, 1989.

[87] Costanza Papucci, Rima Charaf, Carmen Coppola, Adalgisa Sinicropi, Mariangela di Donato, Maria Taddei, Paolo Foggi, Antonella Battisti, Bastiaan de Jong, Lorenzo Zani, Alessandro Mordini, Andrea Pucci, Massimo Calamante, and Gianna Reginato. Luminescent solar concentrators with outstanding optical properties by employment of d–a–d quinoxaline fluorophores. *J. Mater. Chem. C*, 9:15608–15621, 2021.

[88] Sadra Sadeghi, Houman Bahmani Jalali, Rustamzhon Melikov, Baskaran Ganesh Kumar, Mohammad Mohammadi Aria, Cleva W. Ow-Yang, and Sedat Nizamoglu. Stokes-shift-engineered indium phosphide quantum dots for efficient luminescent solar concentrators. *ACS Applied Materials & Interfaces*, 10(15):12975–12982, 2018. PMID: 29589740.

[89] Francesco Meinardi, Hunter McDaniel, Francesco Carulli, Annalisa Colombo, Kirill A. Velizhanin, Nikolay S. Makarov, Roberto Simonutti, Victor I. Klimov, and Sergio Brovelli. Highly efficient large-area colourless luminescent solar concentrators using heavy-metal-free colloidal quantum dots. *Nature Nanotechnology*, 10:1748–3395, 2015.

[90] G G Stokes. On the change of refrangibility of light. *Abstr. Pap. Commun. R. Soc. Lond*, 1852.

[91] Monica Lorenzon and et.al. Reversed oxygen sensing using colloidal quantum wells towards highly emissive photoresponsive varnishes. *Nature Communications*, 6(6434), 2015.

[92] Francesco Meinardi, Annalisa Colombo, Kirill A. Velizhanin, Roberto Simonutti, Monica Lorenzon, Luca Beverina, Ranjani Viswanatha, Victor I. Klimov, and Sergio Brovelli. Large-area luminescent solar concentrators based on 'stokes-shift-engineered' nanocrystals in a mass-polymerized pmma matrix. *Nature Photonics*, 8:1749–4893, 2014.

[93] P. Moraitis, R.E.I. Schropp, and W.G.J.H.M. van Sark. Nanoparticles for luminescent solar concentrators - a review. *Optical Materials*, 84:636–645, 2018.

[94] Abhinav Anand, Matteo L. Zaffalon, Graziella Gariano, Andrea Camellini, Marina Gandini, Rosaria Brescia, Chiara Capitani, Francesco Bruni, Valerio Pinchetti, Margherita Zavelani-Rossi, Francesco Meinardi, Scott A. Crooker, and Sergio Brovelli. Evidence for the band-edge exciton of cuins2 nanocrystals enables record efficient large-area luminescent solar concentrators. *Advanced Functional Materials*, 30(4):1906629, 2020.

[95] Andrés R. M. Velarde, Emily R. Bartlett, Nikolay S. Makarov, Chloe Castañeda, Aaron Jackson, Karthik Ramasamy, Matthew R. Bergren, and Hunter McDaniel. Op-

timizing the aesthetics of high-performance cuins2/zns quantum dot luminescent solar concentrator windows. *ACS Applied Energy Materials*, 3(9):8159–8163, 2020.

[96] D Phillips, RC Drake, DV O'Connor, and RL Christensen. Time correlated single-photon counting (tcspc) using laser excitation. *Instrumentation Science & Technology*, 1985.

[97] S. Caputo, L. Mucchi, F. Cataliotti, M. Seminara, T. Nawaz, and J. Catani. Measurement-based vlc channel characterization for i2v communications in a real urban scenario. *Vehicular Communications*, 28:100305, 2021.

[98] Francesco Meinardi and et.al. Highly efficient luminescent solar concentrators based on earth-abundant indirect-bandgap silicon quantum dots. *Nature Photonics*, 11(1749-4893):177–185, 2017.

[99] G. Giusfredi. *Physical Optics: Concepts, Optical Elements, and Techniques*. UNITEXT for Physics. Springer International Publishing, 2019.

[100] Mark Portnoi, Paul Anthony Haigh, Thomas J. Macdonald, Filip Ambroz, Ivan P. Parkin, Izzat Darwazeh, and Ioannis Papakonstantinou. Bandwidth limits of luminescent solar concentrators as detectors in free-space optical communication systems. *Light: Science & Applications*, 10(1):3, Jan 2021.

[101] ScienceDirect. Shannon sampling theorem. *Science Direct*, 2003.

[102] Tassadaq Nawaz, Marco Seminara, Stefano Caputo, Lorenzo Mucchi, Francesco S. Cataliotti, and Jacopo Catani. Ieee 802.15.7-compliant ultra-low latency relaying vlc system for safety-critical its. *IEEE Transactions on Vehicular Technology*, 68(12):12040–12051, 2019.

[103] H.P.E. Stern, S.A. Mahmoud, and L.E. Stern. *Communication Systems: Analysis and Design*. Pearson Prentice Hall, 2004.

[104] Vanjula Kataria and Dalip Singh Mehta. Multispectral harvesting rare-earth oxysulphide based highly efficient transparent luminescent solar concentrator. *Journal of Rare Earths*, 40(1):41–48, 2022.

[105] Othmane Essahili, Mouad Ouafi, and Omar Moudam. Recent progress in organic luminescent solar concentrators for agrivoltaics: Opportunities for rare-earth complexes. *Solar Energy*, 245:58–66, 2022.

[106] Lorcan J. Brennan, Finn Purcell-Milton, Barry McKenna, Trystan M. Watson, Yurii K. Gun'ko, and Rachel C. Evans. Large area quantum dot luminescent solar concentrators for use with dye-sensitised solar cells. *J. Mater. Chem. A*, 6:2671–2680, 2018.

[107] Kathryn E. Knowles, Troy B. Kilburn, Dane G. Alzate, Stephen McDowall, and Daniel R. Gamelin. Bright cuins2/cds nanocrystal phosphors for high-gain full-spectrum luminescent solar concentrators. *Chem. Commun.*, 51:9129–9132, 2015.

[108] P. Moraitis, R.E.I. Schropp, and W.G.J.H.M. van Sark. Nanoparticles for luminescent solar concentrators - a review. *Optical Materials*, 84:636–645, 2018.

[109] Andrew Kim, Alireza Hosseinmardi, Pratheep K. Annamalai, Pawan Kumar, and Rajkumar Patel. Review on colloidal quantum dots luminescent solar concentrators. *ChemistrySelect*, 6(20):4948–4967, 2021.

[110] Zachar Krumer, Wilfried G.J.H.M. van Sark, Ruud E.I. Schropp, and Celso de Mello Donegá. Compensation of self-absorption losses in luminescent solar concentrators by increasing luminophore concentration. *Solar Energy Materials and Solar Cells*, 167:133–139, 2017.

[111] Paolo Della Sala, Nunzio Buccheri, Alessandro Sanzone, Mauro Sassi, Placido Neri, Carmen Talotta, Alice Rocco, Valerio Pinchetti, Luca Beverina, Sergio Brovelli, and

Carmine Gaeta. First demonstration of the use of very large stokes shift cycloparaphenylenes as promising organic luminophores for transparent luminescent solar concentrators. *Chem. Commun.*, 55:3160–3163, 2019.

[112] Adam P. Green and Alastair R. Buckley. Solid state concentration quenching of organic fluorophores in pmma. *Phys. Chem. Chem. Phys.*, 17:1435–1440, 2015.

[113] Marco Meucci, Sandra Doria, Ali Muhammad Umair, Daniele Franchi, Marco Fattori, Mariangela Di Donato, Alberto Picchi, Andrea Pucci, Massimo Calamante, and Jacopo Catani. Efficient white-light visible light communication with novel optical antennas based on luminescent solar concentrators. *Journal of Lightwave Technology*, pages 1–10, 2023.

[114] Marco Seminara, Tassadaq Nawaz, Stefano Caputo, Lorenzo Mucchi, and Jacopo Catani. Characterization of field of view in visible light communication systems for intelligent transportation systems. *IEEE Photonics Journal*, 12(4):1–16, 2020.

[115] H.P.E. Stern, S.A. Mahmoud, and L.E. Stern. *Communication Systems: Analysis and Design*. Pearson Prentice Hall, 2004.

[116] Xingxing Huang, Zhixin Wang, Jianyang Shi, Yiguang Wang, and Nan Chi. 1.6 gbit/s phosphorescent white led based vlc transmission using a cascaded pre-equalization circuit and a differential outputs pin receiver. *Opt. Express*, 23(17):22034–22042, Aug 2015.

[117] Muhammad Irfan, Usman Habib, Fazal Muhammad, Farman Ali, Abdullah S Alwadie, Shakir Ullah, Adam Glowacz, and Witold Glowacz. Optical-interference mitigation in visible light communication for intelligent transport systems applications. *Energies*, 13(19), 2020.

[118] Sezer Can Tokgoz, Noha Anous, Serhan Yarkan, Diaa Khalil, and Khalid A. Qaraqe. Performance improvement of white led-based vlc systems using blue and flattening

filters. In *2019 International Conference on Advanced Communication Technologies and Networking (CommNet)*, pages 1–6, 2019.

[119] Shuji Nakamura, Takashi Mukai, and Masayuki Senoh. Candela-class high-brightness InGaN/AlGaN double-heterostructure blue-light-emitting diodes. *Applied Physics Letters*, 64(13):1687–1689, 03 1994.

[120] A. M. Khalid, G. Cossu, R. Corsini, P. Choudhury, and E. Ciaramella. 1-gb/s transmission over a phosphorescent white led by using rate-adaptive discrete multitone modulation. *IEEE Photonics Journal*, 4(5):1465–1473, 2012.

[121] Syifaul Fuada, Angga Pratama Putra, Yulian Aska, and Trio Adiono. A first approach to design mobility function and noise filter in vlc system utilizing low-cost analog circuits. *International Journal of Recent Contributions from Engineering, Science; IT (iJES)*, 5(2):pp. 14–30, Jul. 2017.

[122] Huy Nguyen and Yeong Min Jang. Design of mimo c-ook using matched filter for optical camera communication system. In *2021 International Conference on Artificial Intelligence in Information and Communication (ICAIIC)*, pages 474–476, 2021.

[123] Alin-Mihai Căilean, Mihai Dimian, and Valentin Popa. Noise-adaptive visible light communications receiver for automotive applications: A step toward self-awareness. *Sensors*, 20(13), 2020.

[124] Alin-Mihai Căilean, Barthélemy Cagneau, Luc Chassagne, Mihai Dimian, and Valentin Popa. Novel receiver sensor for visible light communications in automotive applications. *IEEE Sensors Journal*, 15(8):4632–4639, 2015.

[125] JosÃ©RaÃMachado-FernÃ¡ndez. Software Defined Radio: Basic Principles and Applications. *Revista Facultad de IngenierÃa*, 24:79 – 96, 01 2015.

[126] Daniel F. Macedo, Dorgival Guedes, Luiz F. M. Vieira, Marcos A. M. Vieira, and Michele Nogueira. Programmable networks—from software-defined radio to software-defined networking. *IEEE Communications Surveys and Tutorials*, 17(2):1102–1125, 2015.

[127] Hanjiang Luo, Kaishun Wu, Rukhsana Ruby, Yongquan Liang, Zhongwen Guo, and Lionel M. Ni. Software-defined architectures and technologies for underwater wireless sensor networks: A survey. *IEEE Communications Surveys & Tutorials*, 20(4):2855–2888, 2018.

[128] Radek Martinek, Lukas Danys, and Rene Jaros. Visible light communication system based on software defined radio: Performance study of intelligent transportation and indoor applications. *Electronics*, 8(4), 2019.

[129] Waqas Hussain, H. Fatih Ugurdag, and Murat Uysal. Software defined vlc system: Implementation and performance evaluation. In *2015 4th International Workshop on Optical Wireless Communications (IWOW)*, pages 117–121, 2015.

[130] Open source gnu radio the gnu software radio project, 2022.

[131] Ettus reserach universal software defined radio, 2022.

[132] Daughter boards developed by attus reserach, 2022.

[133] Muhammad A UMAIR, Marco MEUCCI, and Jacopo CATANI. Experimental characterization of a new softwaredefined radio-based dsp stage for vlc systems. *Optical Wireless Communication Conference*, 2022.

[134] Danilo Valerio. Open source software-defined radio: A survey on gnu-radio and its applications. *ftw. Technical Report*, 09 2008.

[135] R. Khalili and K. Salamatian. A new analytic approach to evaluation of packet error rate in wireless networks. In *3rd Annual Communication Networks and Services Research Conference (CNSR'05)*, pages 333–338, 2005.

[136] Robert H. Hamstra and Paul Wendland. Noise and frequency response of silicon photodiode operational amplifier combination. *Appl. Opt.*, 11(7):1539–1547, Jul 1972.

[137] THE EUROPEAN PARLIAMENT AND THE COUNCIL OF THE EUROPEAN UNION. Directive 2010/31/eu of the european parliament and of the council on the energy performance of buildings. *Official Journal of the European Union*, 2010.

[138] THE EUROPEAN PARLIAMENT AND THE COUNCIL OF THE EUROPEAN UNION. Directive (eu) 2018/2001 of the european parliament and of the council of 11 december 2018 on the promotion of the use of energy from renewable sources (recast). *Official Journal of the European Union*, 2018.

[139] Brian Norton, Philip C. Eames, Tapas K. Mallick, Ming Jun Huang, Sarah J. McCormack, Jayanta D. Mondol, and Yigzaw G. Yohanis. Enhancing the performance of building integrated photovoltaics. *Solar Energy*, 85(8):1629–1664, 2011. Progress in Solar Energy 1.

[140] Yimu Zhao and Richard R. Lunt. Transparent luminescent solar concentrators for large-area solar windows enabled by massive stokes-shift nanocluster phosphors. *Advanced Energy Materials*, 3(9):1143–1148, 2013.

[141] Bryce S. Richards and Ian A. Howard. Luminescent solar concentrators for building integrated photovoltaics: opportunities and challenges. *Energy Environ. Sci.*, 16:3214–3239, 2023.

[142] Ying Nie, Wei He, Xianghua Liu, Zhongting Hu, Hancheng Yu, and Haixiang Liu. Smart luminescent solar concentrator as a bicpv window. *Building Simulation*, 15(10):1789–1798, 2022.

[143] Guoqing Yu, Hongxing Yang, Daina Luo, Xu Cheng, and Mark Kyeredey Ansah. A review on developments and researches of building integrated photovoltaic (bipv) windows and shading blinds. *Renewable and Sustainable Energy Reviews*, 149:111355, 2021.

[144] Krishna Kadam and Manisha R. Dhage. Visible light communication for iot. In *2016 2nd International Conference on Applied and Theoretical Computing and Communication Technology (iCATccT)*, pages 275–278, 2016.

[145] Zhaoji Fang, Hichem Guerboukha, Rabi Shrestha, Malachi Hornbuckle, Yasith Amarasinghe, and Daniel M. Mittleman. Secure communication channels using atmosphere-limited line-of-sight terahertz links. *IEEE Transactions on Terahertz Science and Technology*, 12(4):363–369, 2022.

[146] Tadao Nagatsuma, Shogo Horiguchi, Yusuke Minamikata, Yasuyuki Yoshimizu, Shintaro Hisatake, Shigeru Kuwano, Naoto Yoshimoto, Jun Terada, and Hiroyuki Takahashi. Terahertz wireless communications based on photonics technologies. *Opt. Express*, 21(20):23736–23747, Oct 2013.

[147] Li Gu, Zhiyong Tan, Qingzhao Wu, Chang Wang, and Juncheng Cao. 20 mbps wireless communication demonstration using terahertz quantum devices. *Chin. Opt. Lett.*, 13(8):081402, Aug 2015.

[148] Zhiyong Tan, Zhen Chen, Juncheng Cao, and Huichun Liu. Wireless terahertz light transmission based on digitally-modulated terahertz quantum-cascadelaser. *Chin. Opt. Lett.*, 11(3):031403, Mar 2013.

[149] Muhammad Ali Umair, Marco Meucci, and Jacopo Catani. Strong noise rejection in vlc links under realistic conditions through a real-time sdr front-end. *Sensors*, 23(3), 2023.